relatively short wavelengths. These restrictions are unfortunate because short-range, low altitude operation limits the area of coverage obtained by the system and short wavelengths experience more atmospheric attenuation and dispersion.

8.4 SYNTHETIC APERTURE RADAR

The deficiencies of brute force operation are overcome in *synthetic aperture radar (SAR)* systems. These systems employ a short physical antenna, but through modified data recording and processing techniques, they synthesize the effect of a very long antenna. The result of this mode of operation is a very narrow effective antenna beamwidth, even at far ranges, without requiring a physically long antenna or a short operating wavelength.

At the detailed level, the operation of SAR systems is quite complex. Suffice it to say here that these systems operate on the principle of using the sensor motion along track to transform a single physically short antenna into an array of such antennas that can be linked together mathematically as part of the data recording and processing procedures (Elachi, 1987b). This concept is shown in Figure 8.8. The "real" antenna is shown in several successive positions along the flight line. These successive positions are treated mathemati-

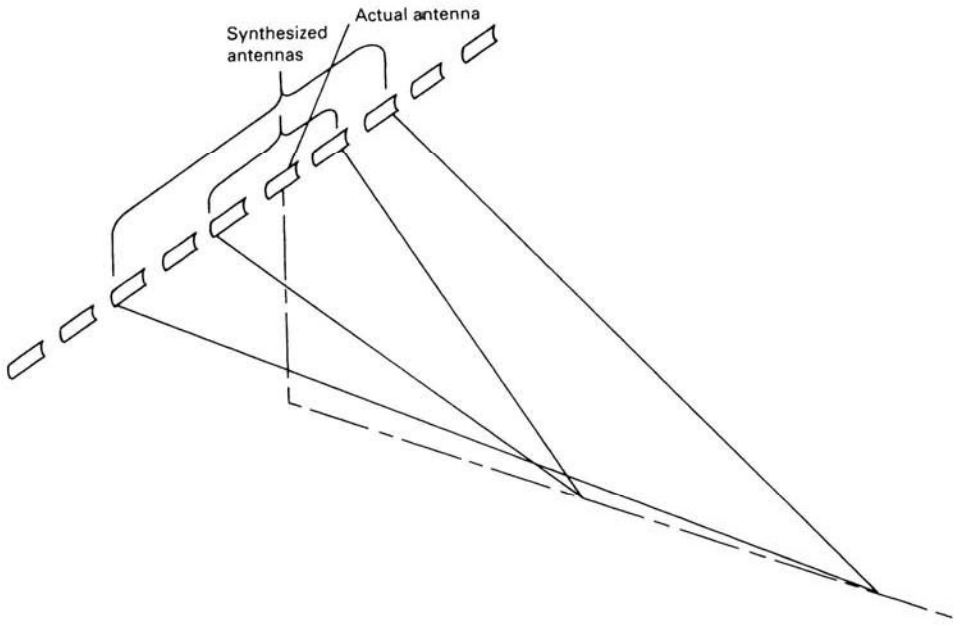

Figure 8.8 Concept of an array of real antenna positions forming a synthetic aperture.

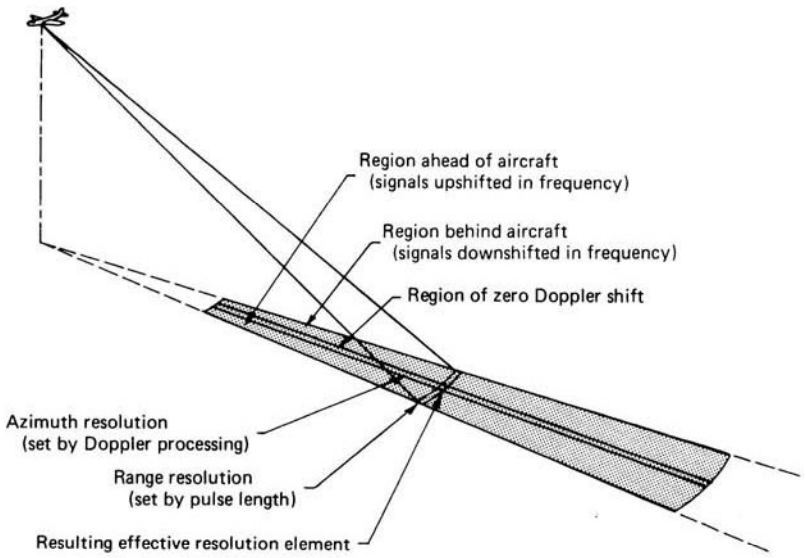

Figure 8.9 Determinants of resolution in synthetic aperture SLR.

cally (or electronically) as if they were simply successive elements of a single, long synthetic antenna. Points on the ground at near range are viewed by proportionately fewer antenna elements than those at far range, meaning effective antenna length increases with range. This results in essentially constant azimuth resolution irrespective of range. Through this process, antennas as long as several kilometers can be synthesized with spaceborne synthetic aperture systems.

Figure 8.9 illustrates yet another approach to explaining how synthetic aperture systems operate, namely discriminating only the near-center return signals from the real antenna beamwidth by detecting Doppler frequency shifts. Recall that a Doppler shift is a change in wave frequency as a function of the relative velocities of a transmitter and a reflector. Within the wide antenna beam, returns from features in the area ahead of the aircraft will have upshifted (higher) frequencies resulting from the Doppler effect. Conversely, returns from the area behind the aircraft will have downshifted (lower) frequencies. Returns from features near the centerline of the beamwidth will experience little or no frequency shift. By processing the return signals according to their Doppler shifts, a very small effective beamwidth can be generated.

Figure 8.10 illustrates the variation with distance of the ground resolution cell size of real aperture systems (*a*) versus synthetic aperture systems (*b*). Note that as the distance from the aircraft increases, the azimuth resolution size increases with real aperture systems and remains constant with synthetic

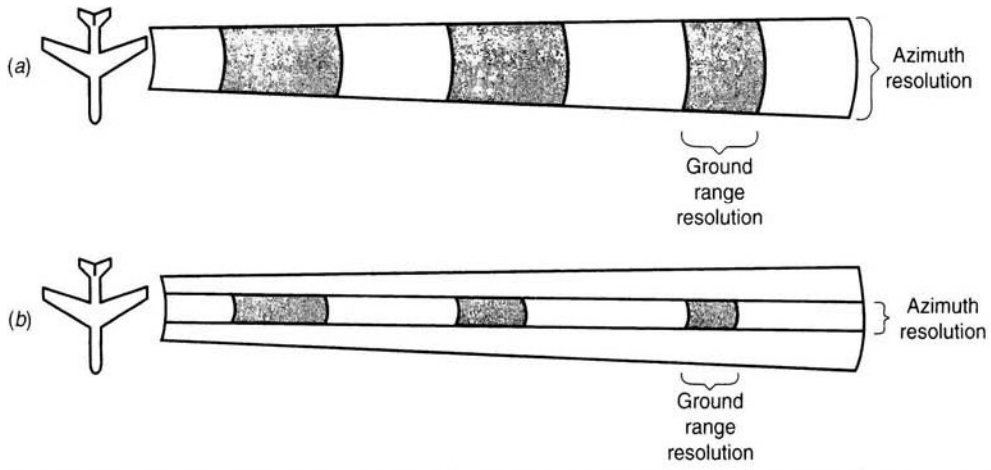

Figure 8.10 Variation with distance of spatial resolution of real aperture (*a*) versus synthetic aperture (*b*) SLR systems.

aperture systems and that the ground range resolution size decreases with both systems.

A final point about SAR systems is that both *unfocused* and *focused* systems exist. Again the details of these systems are beyond our immediate concern. The interesting point about these systems is that the theoretical resolution of *unfocused* systems is a function of wavelength and range, not antenna length. The theoretical resolution of a *focused* system is a function of antenna length, regardless of range or wavelength. More particularly, the resolution of a focused synthetic aperture system is approximately one-half the actual antenna length. That is, the *shorter* the antenna, the finer the resolution. In theory, the resolution for a 1-m antenna would be about 0.5 m, whether the system is operated from an aircraft or a spacecraft! Radar system design is replete with trade-offs among operating range, resolution, wavelength, antenna size, and overall system complexity. (For additional technical information on SAR systems, see Raney, 1998.)

8.5 GEOMETRIC CHARACTERISTICS OF SIDE-LOOKING RADAR IMAGERY

The geometry of SLR imagery is fundamentally different from that of both photography and scanner imagery. This difference basically results because SLR is a *distance* rather than an *angle* measuring system. The influences this has on image geometry are many and varied. Here we limit our discussion to treatment of the following geometric elements of SLR image acquisition and interpretation: *scale distortion*, *relief displacement*, and *parallax*.

Slant-Range Scale Distortion

Side-looking radar systems use one of two types of image recording systems. A *slant-range* image recording system involves a constant sweep rate across each line. Consequently, the spacing between return signals on slant-range imagery is directly proportional to the time interval between echoes from adjacent terrain features. This interval is directly proportional to the *slant*, rather than *horizontal*, distance between the sensor and any given object. In *ground-range* image recording systems, the sweep often incorporates a hyperbolic timing correction in which the spacing between image points is approximately proportional to the horizontal ground distance between terrain features.

Figure 8.11 illustrates the characteristics of slant-range and ground-range image recording. The symbols A, B, and C represent objects of equal size that are equally separated in the near, middle, and far range. The respective ground ranges to the points are $\overline{GR}_A$, $\overline{GR}_B$, and $\overline{GR}_C$. Based directly on the signal return time, the slant-range image shows unequal distances between the features as well as unequal widths for the features. The result is a varying image scale that is at a minimum in the near range and progresses hyperbolically to a maximum at the far range. Therefore, on a slant-range presentation, object width $A_1 < B_1 < C_1$ and distance $\overline{AB} < \overline{BC}$. Applying a hyperbolic correction, a ground-range image of essentially constant scale can be formed with width $A = B = C$ and distance $\overline{AB} = \overline{BC}$. For a given swath width, the change in scale across an image decreases with increasing flying height. Thus, satellite systems have less scale change across an image than do airborne systems.

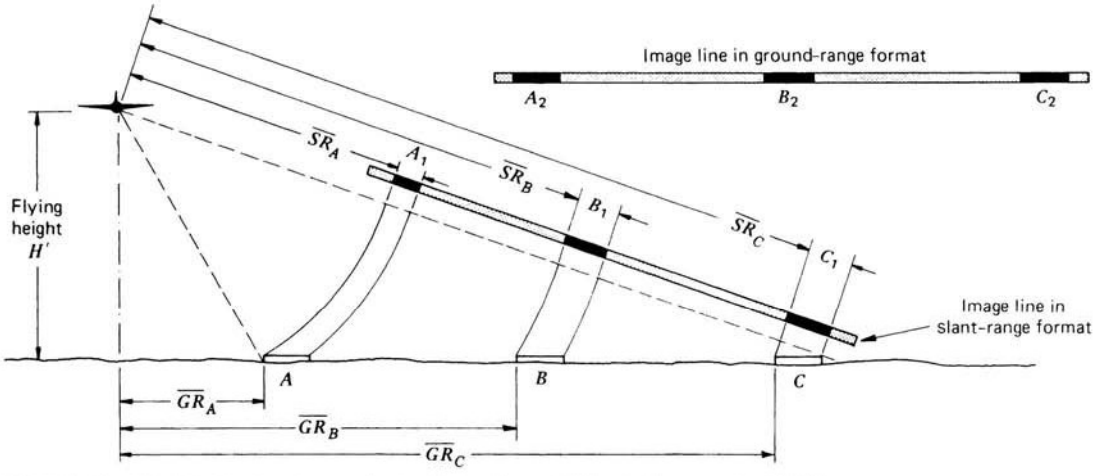

Figure 8.11 Slant-range versus ground-range image format. (Adapted from Lewis, 1976.)

Obviously, the scale distortions inherent in slant-range imagery preclude its direct use for accurate planimetric mapping. However, approximate ground range, $\overline{GR}$, can be derived from slant range, $\overline{SR}$, and flying height, H', under the assumption of flat terrain. From Figure 8.11 it can be seen that

$$\overline{SR}^2 = H'^2 + \overline{GR}^2$$

so

$$\overline{GR} = (\overline{SR}^2 - H'^2)^{1/2} \tag{8.5}$$

Therefore, a ground-range distance can be calculated from an image slant-range distance if the flying height is known. The assumption of flat terrain should be noted, however, and it should be pointed out that flight parameters also affect both range and azimuth scales. The range scale will vary with changes in aircraft altitude, and the azimuth scale will be dependent on precise synchronization between the aircraft ground speed and the data recording system.

Maintaining consistent scale in the collection and recording of SLR data is a complex task. Whereas scale in the range (or across-track) direction is determined by the speed of light, scale in the azimuth (or along-track) direction is determined by the speed of the aircraft or spacecraft. To reconcile and equalize these independent scales, strict control of data collection parameters is needed. In most airborne systems, this is provided by an *inertial navigation and control system*. This device guides the aircraft at the appropriate flying height along the proper course. Angular sensors measure aircraft roll, crab, and pitch and maintain a constant angle of the antenna beam with respect to the line of flight. Inertial systems also provide the output necessary to synchronize the data recording with the aircraft ground speed. Spaceborne systems provide a more stable flight platform.

Relief Displacement

As in line scanner imagery, relief displacement in SLR images is one dimensional and perpendicular to the flight line. However, in contrast to scanner imagery and photography, the *direction* of relief displacement is reversed. This is because radar images display ranges, or distances, from terrain features to the antenna. When a vertical feature is encountered by a radar pulse, the top of the feature is often reached before the base. Accordingly, return signals from the top of a vertical feature will often reach the antenna before returns from the base of the feature. This will cause a vertical feature to "lay over" the closer features, making it appear to lean toward the nadir. This radar *layover effect*, most severe at near range (steeper incident angles), is compared to photographic relief displacement in Figure 8.12.

Terrain slopes facing the antenna at near range are often displayed with a dramatic layover effect. This occurs whenever the terrain slope is steeper

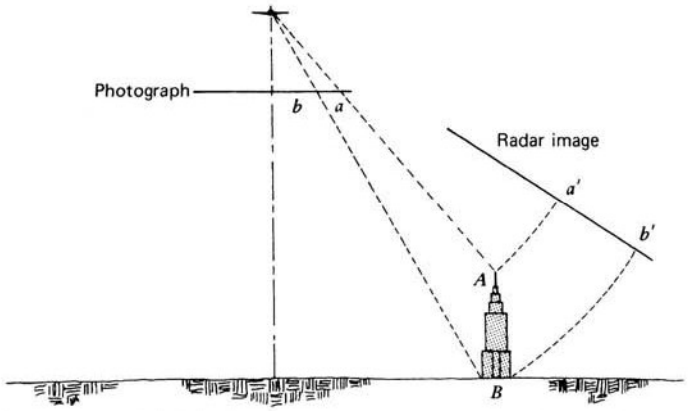

Figure 8.12 Relief displacement on SLR images versus photographs.

than a line perpendicular to the direction of the radar pulse, expressed by its look angle. This condition is met by the left sides of features A and B in Figure 8.13. As such, the tops of these slopes will be imaged before their bases, causing layover. It can be seen in the image representations that the amount of layover displacement is greatest at short range, where the look angle is smaller.

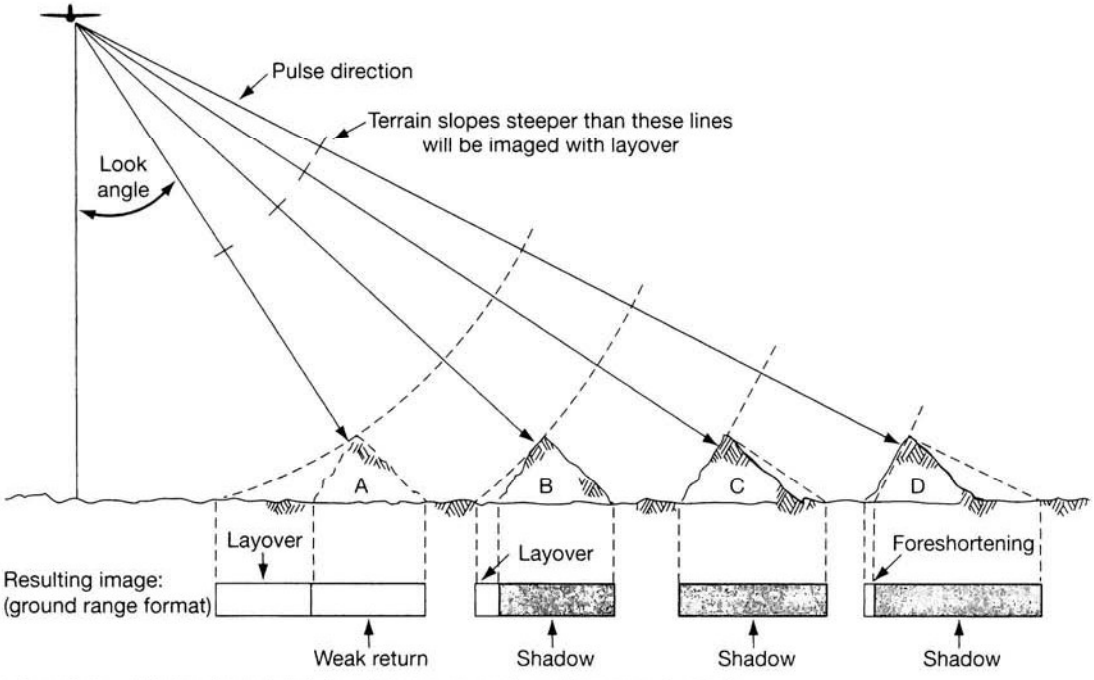

Figure 8.13 Effects of terrain relief on SLR images. (Adapted from Lewis, 1976.)

When the slope facing the antenna is less steep than the line perpendicular to the look direction, as in feature D in Figure 8.13, no layover occurs. That is, the radar pulse reaches the base of the feature before the top. The slopes of the surfaces will not be presented in true size, however. As shown in feature D, the size of the sloped surface is compressed on the image. This *foreshortening effect* becomes more severe as the slope's steepness approaches perpendicularity to the look direction. In feature C, the front slope is precisely perpendicular to the look direction, and it can be seen that the image of the front slope has been foreshortened to zero length.

Figure 8.14, a satellite radar image of the west coast of Vancouver Island, British Columbia, illustrates layover very well. In this image, the effect of layover is very prominent because of the relatively steep look direction of the radar system and the mountainous terrain contained in this image (the satellite track was to the left of the image).

The look angle and terrain slope also affect the phenomenon of *radar shadow*. Slopes facing away from the radar antenna will return weak signals

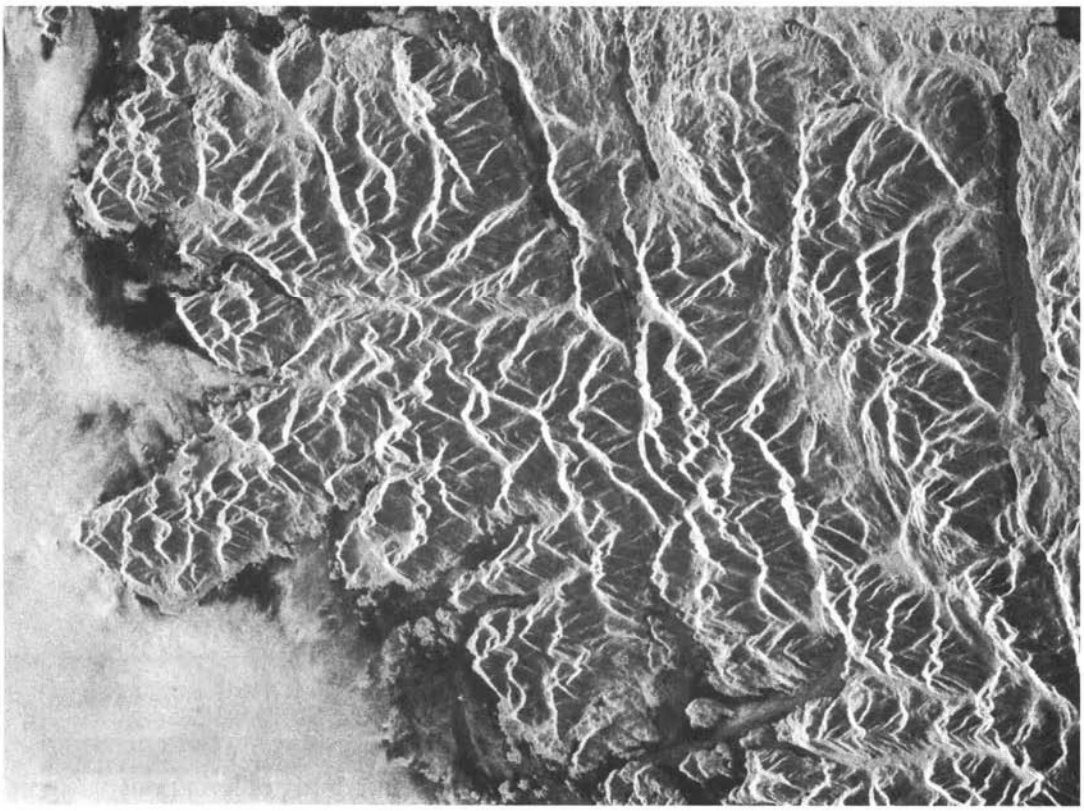

Figure 8.14 ERS-1 radar image, C band, Vancouver Island, British Columbia, midsummer. Scale 1 : 625,000. (Copyright © ESA. Courtesy Canada Centre for Remote Sensing.)

or no signal at all. In Figure 8.13, the right side of feature *A* faces away from the aircraft, but it is less steep than the look direction and will therefore be illuminated by the radar pulse. This illumination, however, will be very slight and the resulting return signals will be weak, causing a fairly dark image area. In feature *B*, its right side is parallel to the look direction and will therefore not be illuminated. As a result, the antenna will receive no return echoes from that side, and the corresponding image area will be totally black. When a slope faces away from the aircraft and is steeper than the look direction, as in features *C* and *D*, the area of nonillumination will extend beyond the sloped area, masking down-range features in a radar shadow. As shown in Figure 8.13, the shadow length increases with range because of the increase in look angle. Thus, a feature that casts an extensive shadow at far range *(D)* could be completely illuminated at close range *(A)*. Note in Figure 8.14 that radar shadows increase toward the right side of the image (farther distance from the satellite).

Parallax

When an object is imaged from two different flight lines, differential relief displacements cause image parallax on SLR images. This allows images to be viewed stereoscopically. Stereo radar images can be obtained by acquiring data from flight lines that view the terrain feature from opposite sides (Figure 8.15*a*). However, because the radar sidelighting will be reversed on

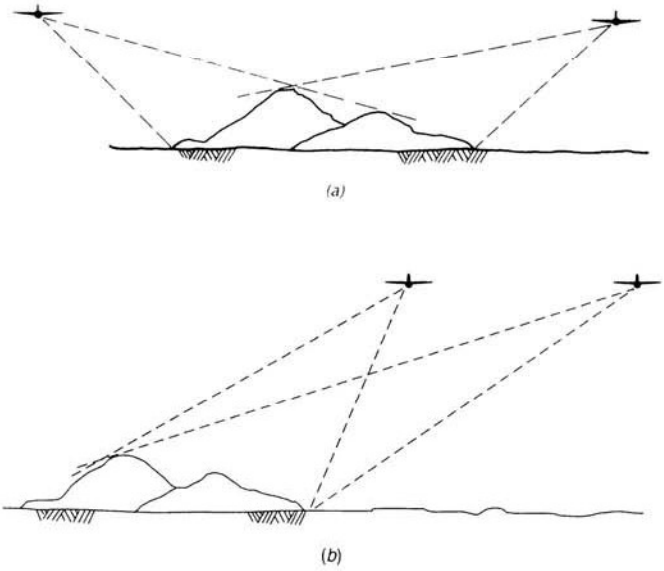

Figure 8.15 Flight orientations to produce parallax on SLR images: (*a*) opposite-side configuration; (*b*) same-side configuration.

the two images in the stereopair, stereoscopic viewing is somewhat difficult using this technique. Accordingly, stereo radar imagery is often acquired from two flight lines at the same altitude on the same side of the terrain feature. In this case, the direction of illumination and the sidelighting effects will be similar on both images (Figure 8.15*b*). It is also possible to acquire stereo radar imagery in the same-side configuration by using different flying heights on the same flight line and, therefore, varying the antenna look angle.

Figure 8.16 shows a stereopair of space radar images of volcanic terrain in Chile that were acquired from two laterally offset flight lines at the same altitude on the same side of the volcano. This resulted in the two different look angles (45° and 54°) that were used for data collection. Although the stereo convergence angle is relatively small (9°), the stereo perception of the imagery is excellent because of the ruggedness of the terrain. The

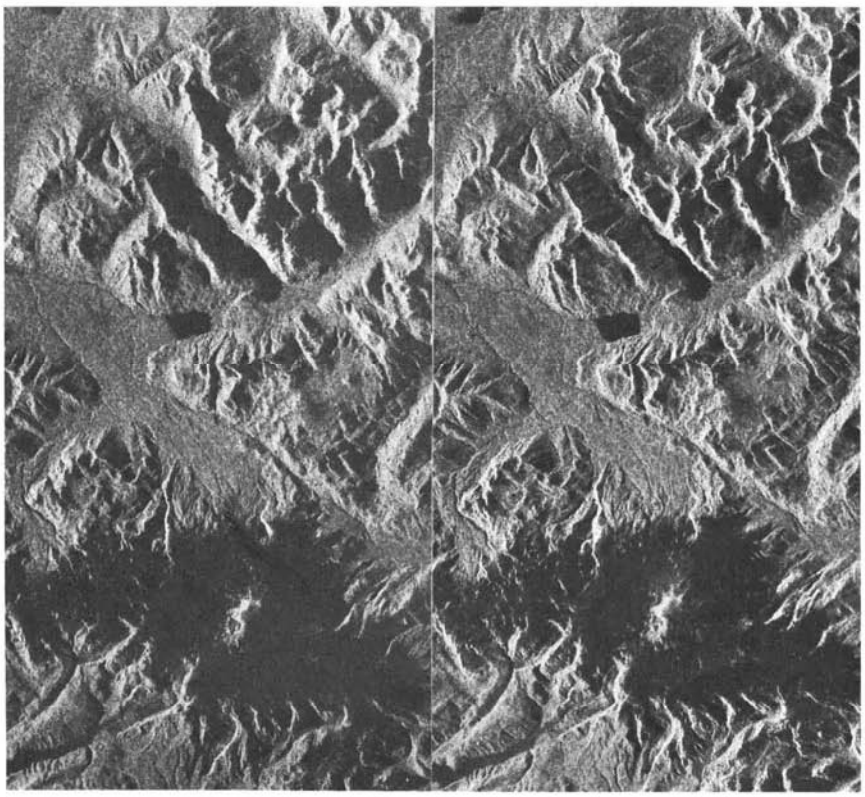

Figure 8.16 Shuttle imaging radar stereopair (SIR-B), Michinmahuida Volcano, Chiloe Province, Chile. Scale 1 : 350,000. The data for this stereopair were collected at two incident angles from the same altitude, with same-side illumination. (Courtesy NASA/JPL/Caltech.)

volcano near the bottom of the figure is Michinmahuida volcano; it rises 2400 m above the surrounding terrain. The snow-covered slopes of this volcano appear dark toned, because of absorption of the radar signal by the snow.

In addition to providing a stereoscopic view, image parallax may be measured and used to compute approximate feature heights. As with aerial photography, parallax is determined by measuring mutual image displacements on the two images forming a stereomodel. Such measurements are part of the science of *radargrammetry*, a field beyond the scope of our interest in this text. (For further information on radargrammetry, see Leberl, 1990, 1998.)

8.6 TRANSMISSION CHARACTERISTICS OF RADAR SIGNALS

The two primary factors influencing the transmission characteristics of the signals from any given radar system are the wavelength and the polarization of the energy pulse used. Table 8.1 lists the common wavelength bands used in pulse transmission. The letter codes for the various bands (e.g., K, X, L) were originally selected arbitrarily to ensure military security during the early stages of radar development. They have continued in use as a matter of convenience, and various authorities designate the various bands in slightly different wavelength ranges.

Naturally, the wavelength of a radar signal determines the extent to which it is attenuated and/or dispersed by the atmosphere. Serious atmospheric effects on radar signals are confined to the shorter operating wavelengths (less than about 4 cm). Even at these wavelengths, under most operating conditions the atmosphere only slightly attenuates the signal. As one would anticipate, attenuation generally increases as operating wavelength decreases, and

TABLE 8.1 Radar Band Designations

Band Designation	Wavelength λ (cm)	Frequency $\nu = c\lambda^{-1}$ [MHz (10^6 cycles sec^{-1})]
K_a	0.75–1.1	40,000–26,500
K	1.1–1.67	26,500–18,000
K_u	1.67–2.4	18,000–12,500
X	2.4–3.75	12,500–8,000
C	3.75–7.5	8000–4000
S	7.5–15	4000–2000
L	15–30	2000–1000
P	30–100	1000–300

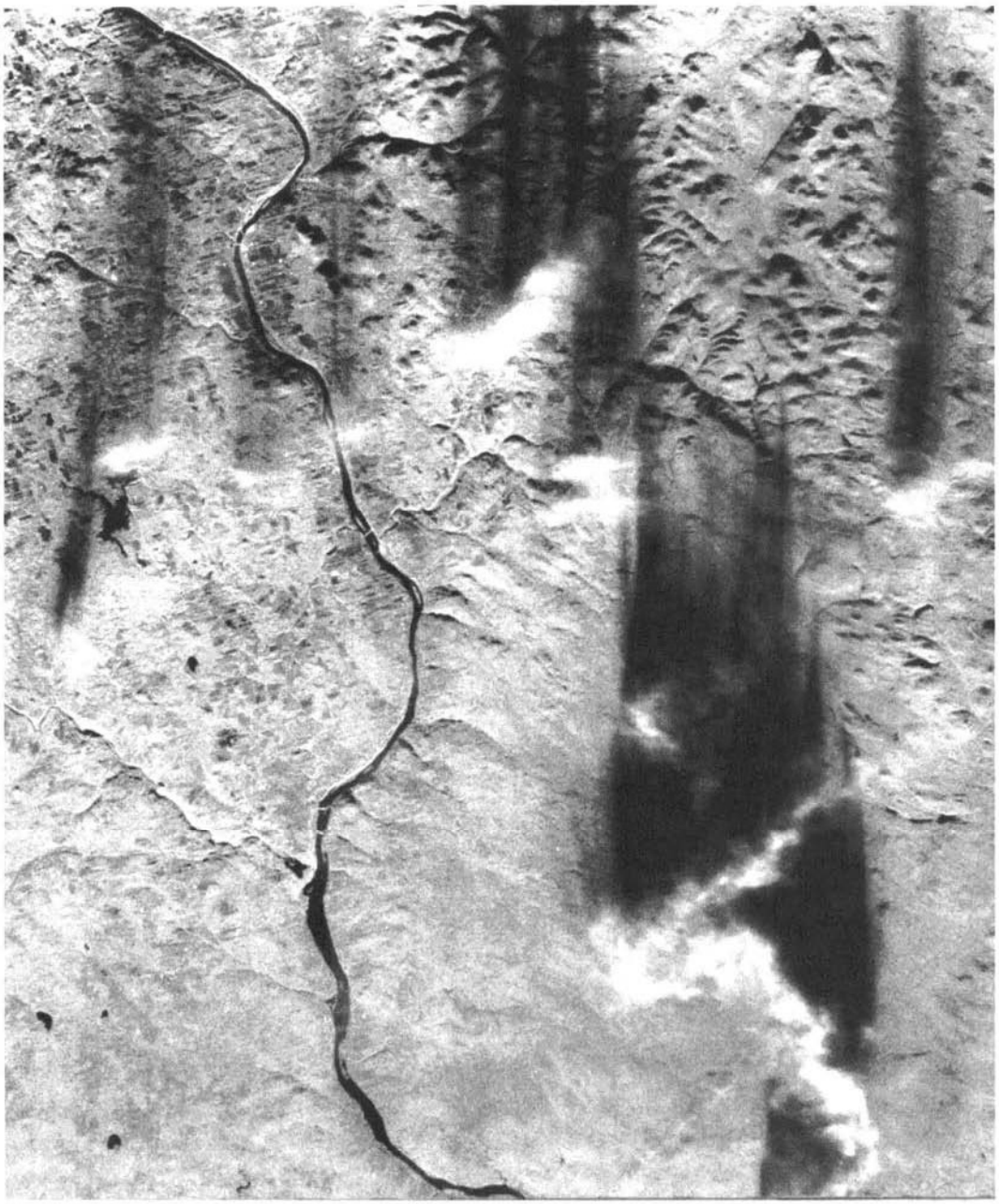

Figure 8.17 X-band airborne side-looking radar data acquired near Woodstock, New Brunswick, Canada, illustrating an unusual shadow effect created by severe rainfall activity and radar signal attenuation. (Courtesy Agriculture and Agri-Food Canada, Fredericton.)

the influence of clouds and rain is variable. Whereas radar signals are relatively unaffected by clouds, echoes from heavy precipitation can be considerable. Precipitation echoes are proportional, for a single drop, to the quantity D^6/λ^4, where D is the drop diameter. With the use of short wavelengths, radar reflection from water droplets is substantial enough to be used in PPI systems to distinguish regions of precipitation. For example, rain and clouds can affect radar signal returns when the radar wavelength is 2 cm or less. At the same time, the effect of rain is minimal with wavelengths of operation greater than 4 cm. With K- and X-band radar, rain may attenuate or scatter radar signals significantly.

Figure 8.17 illustrates an unusual shadow effect created by severe rainfall activity and demonstrates the wavelength dependence of radar systems. In this X-band airborne radar image, the bright "cloudlike" features are due to backscatter from rainfall. The dark regions "behind" these features (especially well seen at lower right) can be created by one of two mechanisms. One explanation is that they are "hidden" because the rain completely attenuates the incident energy, preventing illumination of the ground surface. Alternatively, a portion of the energy penetrates the rain during radar signal transmission but is completely attenuated after backscatter. This is termed *two-way attenuation*. In either case, much less energy is returned to the receiving antenna. When the signal is not completely attenuated, some backscatter is received (upper left).

Another effect of rainfall on radar images is that rain occurring at the time of data acquisition can change the physical and dielectric properties of the surface soil and vegetation, thus affecting backscatter. Figure 8.18 shows an area in Alberta, Canada, with dense forest and clearcut areas. The forested areas present a rougher surface to the radar waves and appear lighter toned than the smoother clearcut areas. Figure 8.18*a* was imaged under dry conditions, and the tonal differences between the forested and clearcut areas are very clear. Figure 8.18*b* was imaged during a period of heavy rain, and the tonal differences between the forested and clearcut areas are subdued.

Irrespective of wavelength, radar signals can be transmitted and/or received in different modes of *polarization*. That is, with polarimetric radar systems, the signal can be filtered in such a way that its electrical wave vibrations are restricted to a single plane perpendicular to the direction of wave propagation. (Unpolarized energy vibrates in all directions perpendicular to that of propagation.) A radar signal can be transmitted in either a horizontal (H) or a vertical (V) plane. Likewise, it can be received in either a horizontal or a vertical plane. Thus, we have the possibility of dealing with four different combinations of signal transmission and reception: H send, H receive (HH); H send, V receive (HV); V send, H receive (VH); and V send, V receive (VV). *Like-polarized* imagery results from the HH or

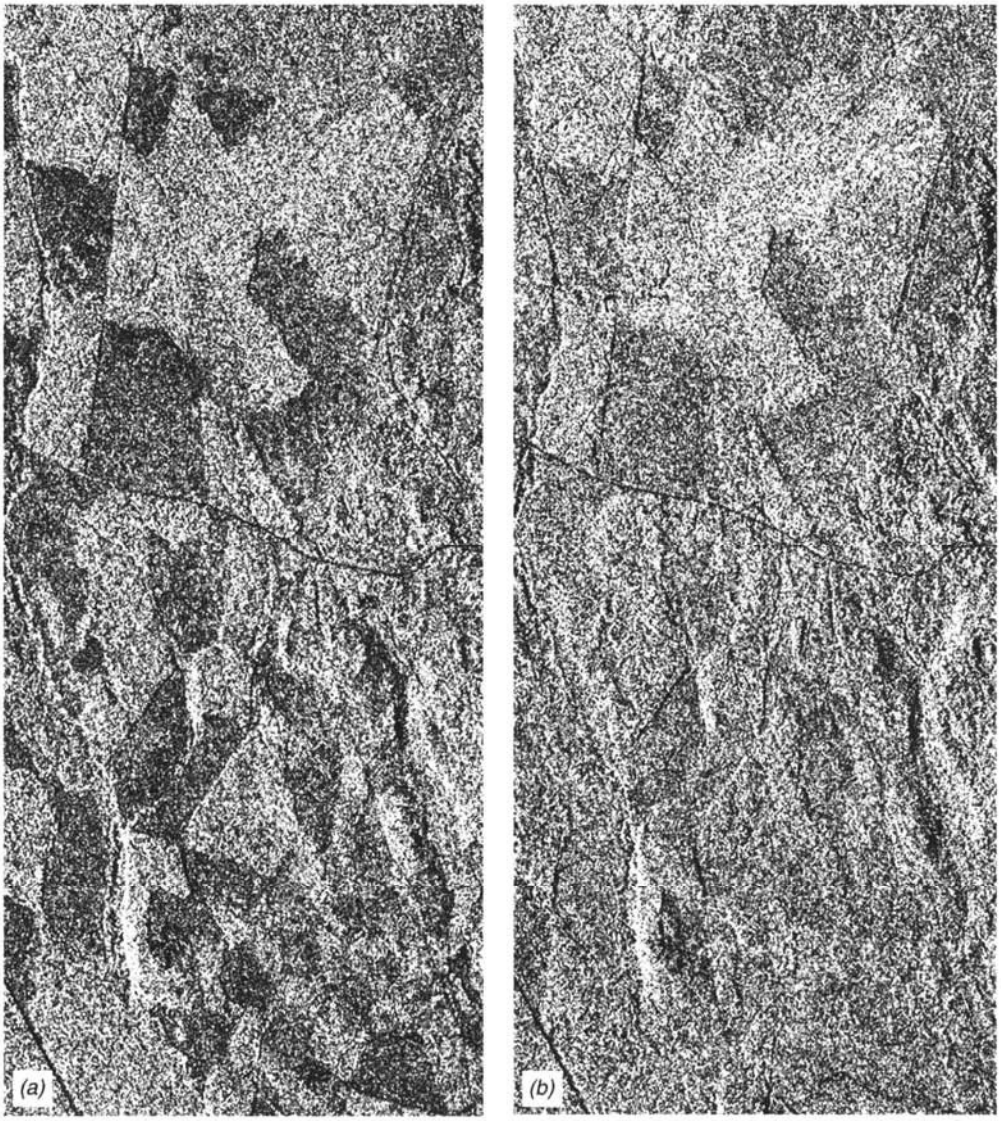

Figure 8.18 Spaceborne radar images of a forested area near Whitecourt, Alberta, Canada, illustrating the effects of heavy rain on radar returns. C band, HH polarization. Figure 8.18*a* was imaged in October under dry conditions, and the distinction between the light-toned forested areas and the darker toned clearcut areas is very clear. Figure 8.18*b* was imaged in August during a period of heavy rain, and the tonal differences between the forested and clearcut areas are much less. (Radarsat images copyright © Canadian Space Agency 1996. Courtesy Canada Centre for Remote Sensing.)

VV combinations. *Cross-polarized* imagery is obtained from HV or VH combinations. Systems that simultaneously collect data in HH, HV, VH, and VV combinations are said to have *quadrature polarization*. *Circular polarization*, where the plane of wave vibrations rotates as the waves propagate, can also be utilized. Since various objects modify the polarization of the energy they reflect to varying degrees, the mode of signal polarization influences how the objects look on the resulting imagery. We illustrate this in Section 8.8. (For further information on radar polarization, see Boerner, 1998.)

For long wavelengths (P band) at high altitude (greater than 500 km), the ionosphere can have significant effects on the transmission of radar signals. These effects occur in at least two ways. First, passage through the ionosphere can result in a propagation delay, which leads to errors in the measurement of the slant range. Second, there is a phenomenon known as *Faraday rotation*, whereby the plane of polarization is rotated somewhat, in direct proportion to the amount of ionospheric activity from the planet's magnetic field. These factors can cause significant problems for polarimetric, long wavelength, orbital SAR systems. (For further information on these effects, see Curlander and McDonough, 1991.)

8.7 OTHER RADAR IMAGE CHARACTERISTICS

Other characteristics that affect the appearance of radar images are *radar image speckle* and *radar image range brightness variation*. These factors are described below.

Radar Image Speckle

Radar images, such as those illustrated here, contain some degree of *speckle*. Microwave signals returning from a given location on the earth's surface can be in phase or out of phase by varying degrees when received by the sensor. This produces a seemingly random pattern of brighter and darker pixels in radar images, giving them a distinctly grainy appearance (or speckle).

Speckle can be reduced through the application of image processing techniques, such as averaging neighboring pixel values, or by special filtering and averaging techniques but cannot be completely eliminated. One technique useful for reducing speckle is *multiple-look processing*. In this procedure, several independent images of the same area, produced by using different portions of the synthetic aperture, are averaged together to

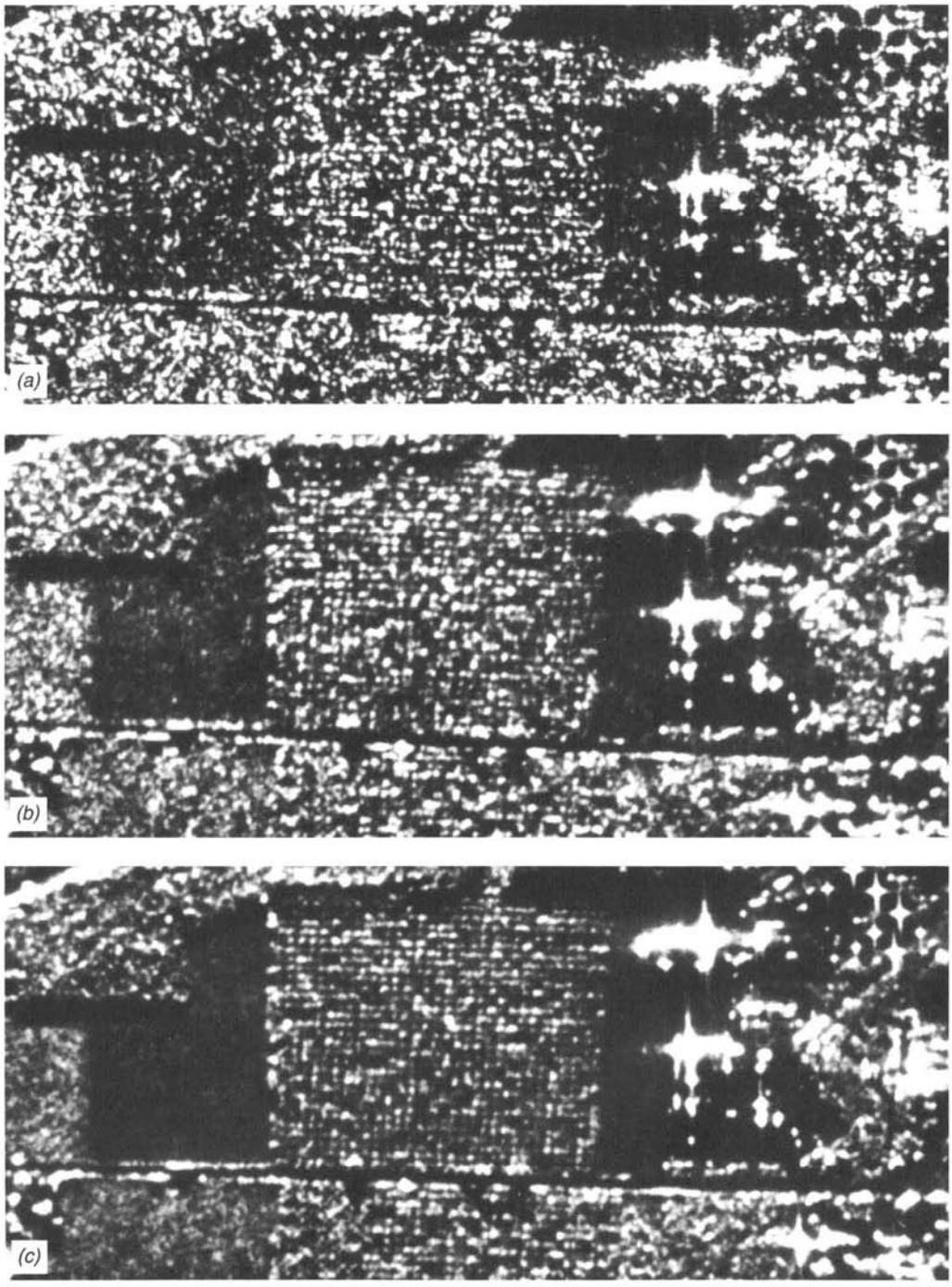

Figure 8.19 An example of multilook processing and its effect on image speckle: (*a*) 1 look; (*b*) 4 looks; (*c*) 16 looks. X-band airborne SAR radar image. Note that speckle decreases as the number of looks increases. These images were specially processed such that the image resolution is the same for all three parts of the figure; 16 times as much data were required to produce the image in (*c*) as the image in (*a*). (From American Society for Photogrammetry and Remote Sensing, 1998. Images copyright © John Wiley & Sons.)

produce a smoother image. The number of statistically independent images being averaged is called the *number of looks*, and the amount of speckle is inversely proportional to the square root of this value. Given that the input data characteristics are held constant, the size of the resolution cell of the output image is directly proportional to the number of looks. For example, a four-look image would have a resolution cell four times larger than a one-look image and a speckle standard deviation one-half that of a one-look image. Hence, both the number of looks and the resolution of a system contribute to the overall quality of a radar image. For further information on number of looks versus other image characteristics, such as speckle and resolution, see Raney (1998) and Lewis, Henderson, and Holcomb (1998).

Figure 8.19 illustrates the appearance of radar images of the same scene with different numbers of looks. The amount of speckle is much less with 4 looks (*b*) than with 1 look (*a*), and even less with 16 looks (*c*). These images were specially processed such that the image resolution is the same for all three parts of the figure; 16 times as much data were required to produce the image in (*c*) as the image in (*a*).

Radar Image Range Brightness Variation

Synthetic aperture radar images often contain a systematic gradient in image brightness across the image in the range direction. This is principally caused by two geometric factors. First, the size of the ground resolution cell decreases from near range to far range, reducing the strength of the return signal. Second, and more significantly, backscatter is inversely related to the local incident angle (i.e., as the local incident angle increases, backscatter decreases), which is in turn related to the distance in the range direction. As a result, radar images will tend to become darker with increasing range. This effect is typically more severe for airborne radar systems than for spaceborne systems because the range of look angles is larger for the airborne systems with a lower flying height (for the same swath width). To some degree, mathematical models can be used to compensate for this effect, resulting in images without visible range brightness illumination effects. Some SAR systems (e.g., SIR-C) correct for the first of these geometric factors (decreasing ground resolution cell size), but not the second (increasing local incident angle), the effects of which are more complex.

Figure 8.20 is an airborne SAR image with a difference in look angle from near to far range of about 14°. Figure 8.20*a* has no compensation for range-related brightness variation, while a simple empirical model has been used to compensate for this effect in Figure 8.20*b*.

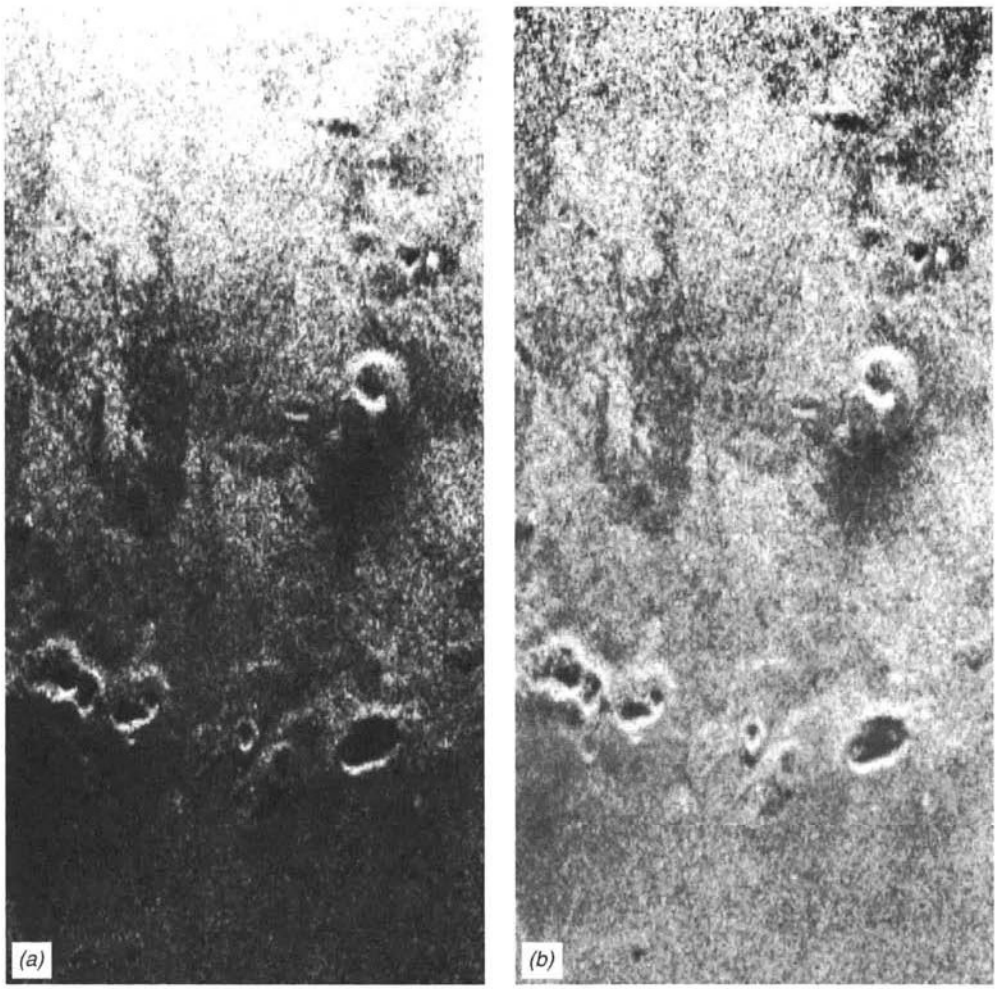

Figure 8.20 Airborne SAR radar images, Hualalai volcano, Hawaii: (*a*) without compensation for range brightness falloff; (*b*) with compensation for range brightness falloff. The difference in look angle from near range (top of the image) to far range (bottom of the image) is about 14°. (Courtesy NASA/JPL/Caltech.)

8.8 RADAR IMAGE INTERPRETATION

Side-looking radar image interpretation has been successful in many fields of application. These include, for example, mapping major rock units and surficial materials, mapping geologic structure (folds, faults, and joints), mapping vegetation types (natural vegetation and crops), determining sea ice types, and mapping surface drainage features (streams and lakes).

Because of its sidelighted character, SLR imagery superficially resembles aerial photography taken under low sun angle conditions. However, a host of

earth surface feature characteristics work together with the wavelength, incident angle, and polarization of radar signals to determine the intensity of radar returns from various objects. These factors are many, varied, and complex. Although several theoretical models have been developed to describe how various objects reflect radar energy, most practical knowledge on the subject has been derived from empirical observation. It has been found that the primary factors influencing objects' return signal intensity are their geometric and electrical characteristics; these are described below. The effects of radar signal polarization are illustrated, and radar wave interactions with soil, vegetation, water and ice, and urban areas are also described.

Geometric Characteristics

Again, of the most readily apparent features of radar imagery is its "sidelighted" character. This arises through variations in the relative sensor/terrain geometry for differing terrain orientations, as was illustrated in Figure 8.13. Variations in local incident angle result in relatively high returns from slopes facing the sensor and relatively low returns, or no returns, from slopes facing away from the sensor.

In Figure 8.21, the return-strength-versus-time graph has been positioned over the terrain such that the signals can be correlated with the feature that produced them. Above the graph is the corresponding image line, in which the signal strength has been converted schematically to brightness values. The response from this radar pulse initially shows a high return from the slope facing the sensor. This is followed by a duration of no return signal from areas blocked from illumination by the radar wave. This radar shadow

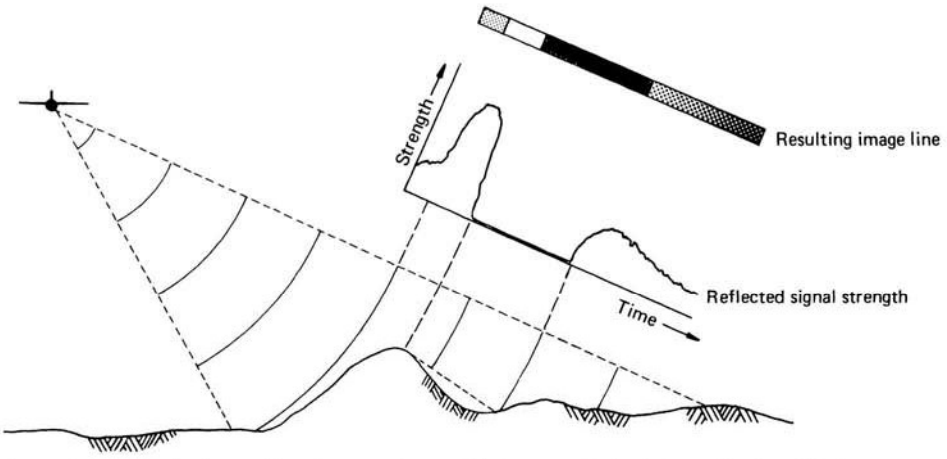

Figure 8.21 Effect of sensor/terrain geometry on SLR imagery. (Adapted from Lewis, 1976.)

is completely black and sharply defined, unlike shadows in photography that are weakly illuminated by energy scattered by the atmosphere. Note that radar shadows can be seen in several radar images in this chapter. Following the shadow, a relatively weak response is recorded from the terrain that is not oriented toward the sensor.

Radar backscatter and shadow areas are affected by different surface properties over a range of local incident angles. As a generalization, for local incident angles of 0° to 30°, radar backscatter is dominated by topographic slope. For angles of 30° to 70°, surface roughness dominates. For angles greater than 70°, radar shadows dominate the image.

Figure 8.22 illustrates radar reflection from surfaces of varying roughness and geometry. The *Rayleigh criterion* states that surfaces can be considered "rough," and act as diffuse reflectors (Figure 8.22*a*), if the root-mean-square (rms) height of the surface variations exceeds one-eighth of the wavelength of sensing ($\lambda/8$) divided by the cosine of the local incident angle (Sabins, 1997). Such surfaces scatter incident energy in all directions and return a significant portion of the incident energy to the radar antenna. Surfaces are considered "smooth" by the Rayleigh criterion, and act as specular reflectors (Figure 8.22*b*), when their rms height variation is less than approximately $\lambda/8$ divided by the cosine of the local incident angle. Such surfaces reflect most of the energy away from the sensor, resulting in a very low return signal.

The Rayleigh criterion does not consider that there can be a category of surface relief that is intermediate between definitely rough and definitely smooth surfaces. A *modified Rayleigh criterion* is used to typify such situations. This criterion considers rough surfaces to be those where the rms

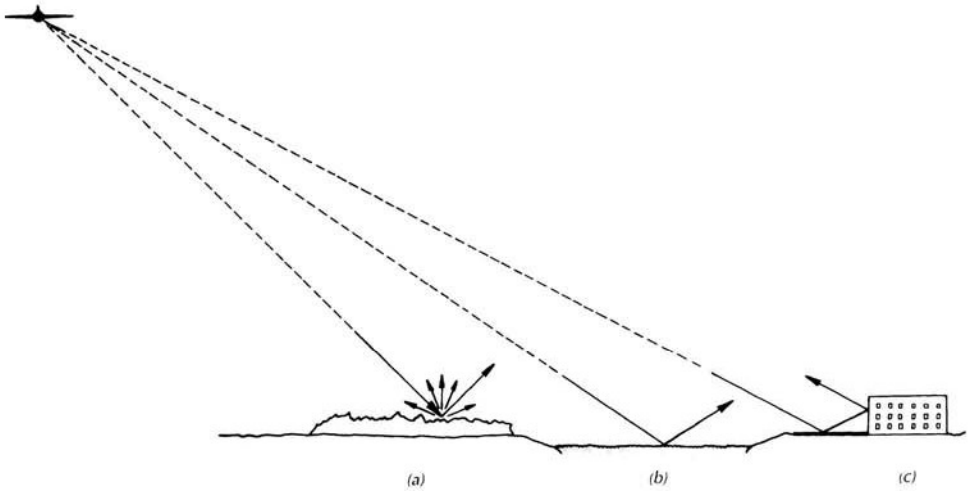

Figure 8.22 Radar reflection from various surfaces: (*a*) diffuse reflector; (*b*) specular reflector; (*c*) corner reflector.

TABLE 8.2 Definition of Synthetic Aperture Radar Roughness Categories for Three Local Incident Angles[a]

Roughness Category	Root-Mean-Square Surface Height Variation (cm)		
	K_a Band (λ = 0.86 cm)	X Band (λ = 3.2 cm)	L Band (λ = 23.5 cm)
(*a*) Local incidence angle of 20°			
Smooth	<0.04	<0.14	<1.00
Intermediate	0.04–0.21	0.14–0.77	1.00–5.68
Rough	>0.21	>0.77	>5.68
(*b*) Local incidence angle of 45°			
Smooth	<0.05	<0.18	<1.33
Intermediate	0.05–0.28	0.18–1.03	1.33–7.55
Rough	>0.28	>1.03	>7.55
(*c*) Local incidence angle of 70°			
Smooth	<0.10	<0.37	<2.75
Intermediate	0.10–0.57	0.37–2.13	2.75–15.6
Rough	>0.57	>2.13	>15.6

Source: Adapted from Sabins, 1997.

[a]The table is based on a modified Rayleigh criterion.

height is greater than $\lambda/4.4$ divided by the cosine of the local incident angle and smooth when the rms height variation is less than $\lambda/25$ divided by the cosine of the local incident angle (Sabins, 1997). Intermediate values are considered to have intermediate roughnesses. Table 8.2 lists the surface height variations that can be considered smooth, intermediate, and rough for several radar bands for local incident angles of 20°, 45°, and 70°. (Values for other wavelength bands and/or incident angles can be calculated from the information given above.)

Figure 8.23 graphically illustrates how the amount of diffuse versus specular reflection for a given surface roughness varies with wavelength, and Table 8.3 describes how rough various surfaces appear to radar pulses of various wavelengths using the modified Rayleigh criterion described above. It should be noted that some features, such as corn fields, might appear rough when seen in both the visible and the microwave portion of the spectrum. Other surfaces, such as roadways, may be diffuse reflectors in the visible region but specular reflectors of microwave energy. In general, radar images manifest many more specular surfaces than do photographs.

The shape and orientation of objects must be considered as well as their surface roughness when evaluating radar returns. A particularly bright response results from a *corner reflector*, as illustrated in Figure 8.22*c*. In this case, adjacent smooth surfaces cause a double reflection that yields a very

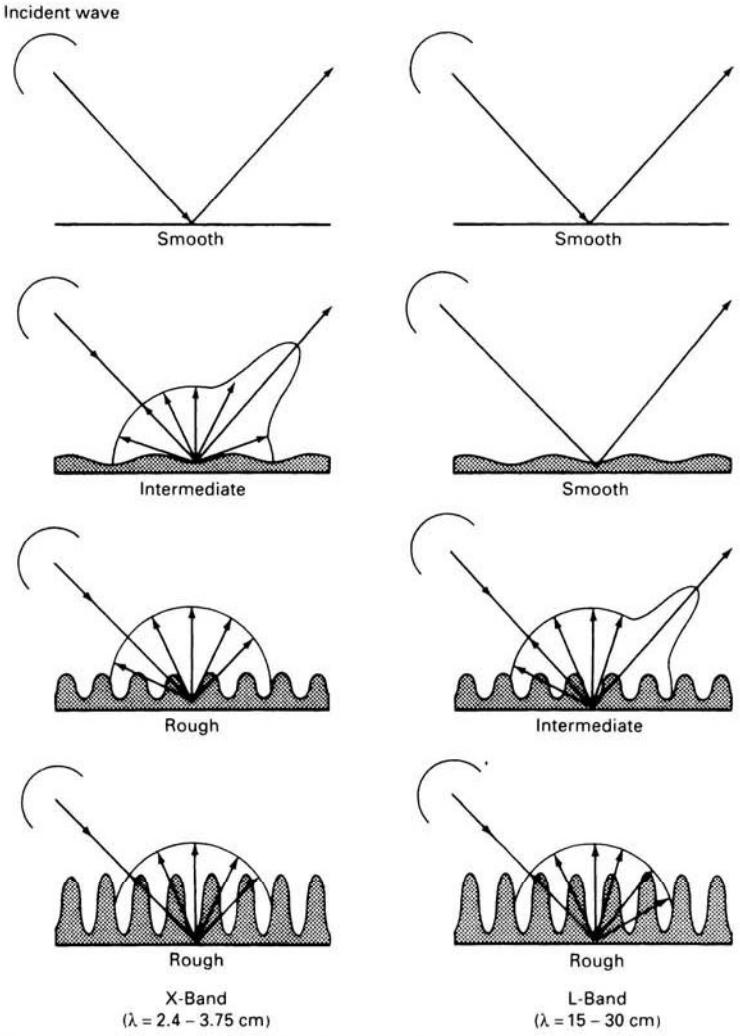

Figure 8.23 X-band and L-band radar reflection from surfaces of varying roughness. (Modified from diagram by Environmental Research Institute of Michigan.)

high return. Because corner reflectors generally cover only small areas of the scene, they typically appear as bright spots on the image.

Electrical Characteristics

The electrical characteristics of terrain features work closely with their geometric characteristics to determine the intensity of radar returns. One

TABLE 8.3 Synthetic Aperture Radar Roughness at a Local Incident Angle of 45°

Root-Mean-Square Surface Height Variation (cm)	K_a Band (λ = 0.86 cm)	X Band (λ = 3.2 cm)	L Band (λ = 23.5 cm)
0.05	Smooth	Smooth	Smooth
0.10	Intermediate	Smooth	Smooth
0.5	Rough	Intermediate	Smooth
1.5	Rough	Rough	Intermediate
10.0	Rough	Rough	Rough

Source: Adapted from Sabins, 1997.

measure of an object's electrical character is the *complex dielectric constant*. This parameter is an indication of the reflectivity and conductivity of various materials.

In the microwave region of the spectrum, most natural materials have a dielectric constant in the range 3 to 8 when dry. On the other hand, water has a dielectric constant of approximately 80. Thus, the presence of moisture in either soil or vegetation can significantly increase radar reflectivity. In fact, changes in radar signal strength from one material to another are often linked to changes in moisture content much more closely than they are to changes in the materials themselves. Because plants have large surface areas and often have a high moisture content, they are particularly good reflectors of radar energy. Plant canopies with their varying complex dielectric constants and their microrelief often dominate the texture of radar image tones.

It should be noted that the dielectric constant of vegetation changes with atmospheric conditions. Clouds limit incident radiation on the earth's surface, changing the water content of the surface vegetation. In particular, clouds decrease or stop vegetation transpiration, which in turn changes the water potential, dielectric constant, and radar backscatter of vegetation.

Metal objects also give high returns, and metal bridges, silos, railroad tracks, and poles usually appear as bright features on radar images. Figure 8.24*a* is a side-looking airborne radar image showing a small urban area (population 6000) adjacent to the Mississippi River. In the urban area, note the high return from the larger buildings of the central business district, which act as corner reflectors, as well as from the metallic bridges crossing the river. The river water acts as a specular reflector and has a very dark image tone. The urban area is located on a river terrace with flat topography. Note the rectangular field patterns resulting from image tone differences caused by differing amounts of diffuse reflection from different crops on this terrace. Figure 8.24*b* shows agricultural land in an area of thick loess (wind blown silt) with moderate relief. Strip farming (to control soil erosion) can be

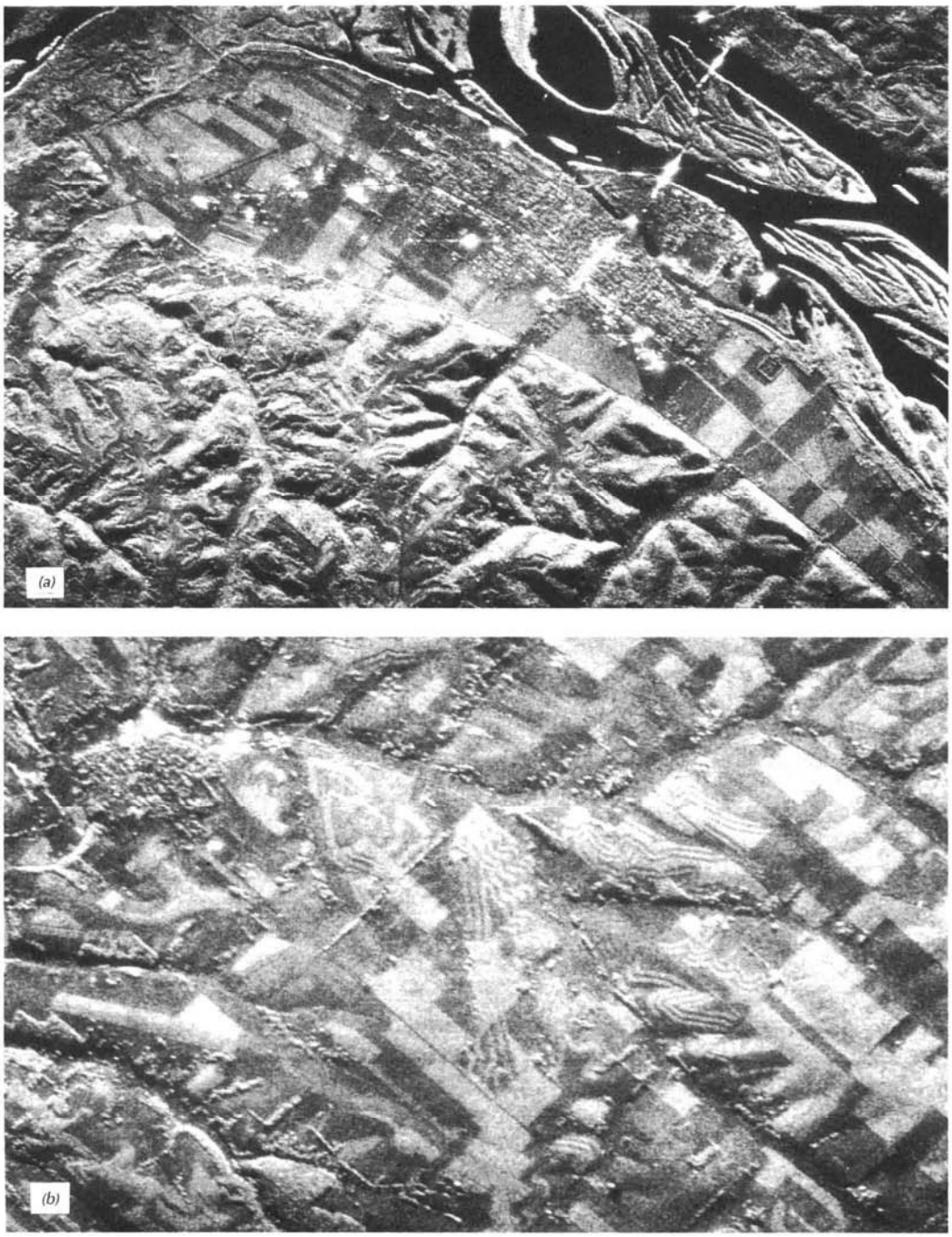

Figure 8.24 SLAR images, southwestern Wisconsin, late summer, X band, synthetic aperture. (*a*) Prairie du Chien and vicinity. 1 : 80,000. (*b*) Rural area near Prairie du Chien. 1 : 50,000. (Courtesy Strategic Air Command and Goodyear Aerospace.)

seen on this image as alternations of light-toned and dark-toned crops resembling contour lines.

Effect of Polarization

Figures 8.25 and 8.26 illustrate the effect of radar signal polarization on the resulting images. Figure 8.25 is a side-looking airborne radar image of an area of folded sedimentary rocks obtained using both HH and HV polarizations. A large synclinal mountain is seen in the upper left and center portions of the scene. Note that the slopes facing the top of the page have a lighter tone than those facing the bottom. This is because the flight line was to the top of this image and slopes facing that direction produce a greater return signal. Despite the fact that the topography of this bedrock hill is so strikingly exhibited on this radar image, the radar signal is principally returned from vegetation surfaces. The banding that can be seen around the synclinal mountain is due to an alternation of bedrock types, principally sandstone and shale. Some of the banding results from differences in shading because of topography, and some results from differences in vegetation type and vigor over the different rock formations. Note also the dark tone of the lake at right center and the various rivers in this scene caused by specular reflection of the radar signal. The cross-polarized signal (HV), in this case, results in an image with less image contrast, showing fewer distinctions among vegetation types, than the like-polarized (HH) image. Because the complex manner in which radar signals interact with and return from features is dependent on slope orientation, surface roughness, vegetation cover, and soil and vegetation water content, it is not always possible to predict whether HH or HV images will have a higher information content for a particular application. As shown in the next illustration, there can be conditions where the cross-polarized image has a greater information content than the like-polarized image.

Figure 8.26 is a side-looking airborne radar image showing an area with a variety of soil and rock conditions obtained using both HH and HV polarizations. At the top of the image are dissected bedrock hills with sufficient relief to exhibit considerable shadowing. Below the bedrock hills is a light-toned area of alluvial materials washed down from the bedrock hills. Some braiding of the distributary stream channels can be seen, especially on the HV image. Basaltic lava flows can be seen at C and D. The "Sunshine Basalt" flow (C) issued from Sunshine Crater (20 mm above and to the right of the letter C on this image). The younger "Pisgah Basalt" flow (D) issued from Pisgah Crater, located just outside the lower right-hand corner of this image. The Sunshine Basalt flow has a much darker tone on the HV image than the Pisgah Basalt flow, whereas both have nearly the same tone on the HH image. The small alluvial fan at *A* has a much lighter tone than the adjacent Sunshine Basalt flow on the HV image but nearly the same tone on the HH image. This lighter tone

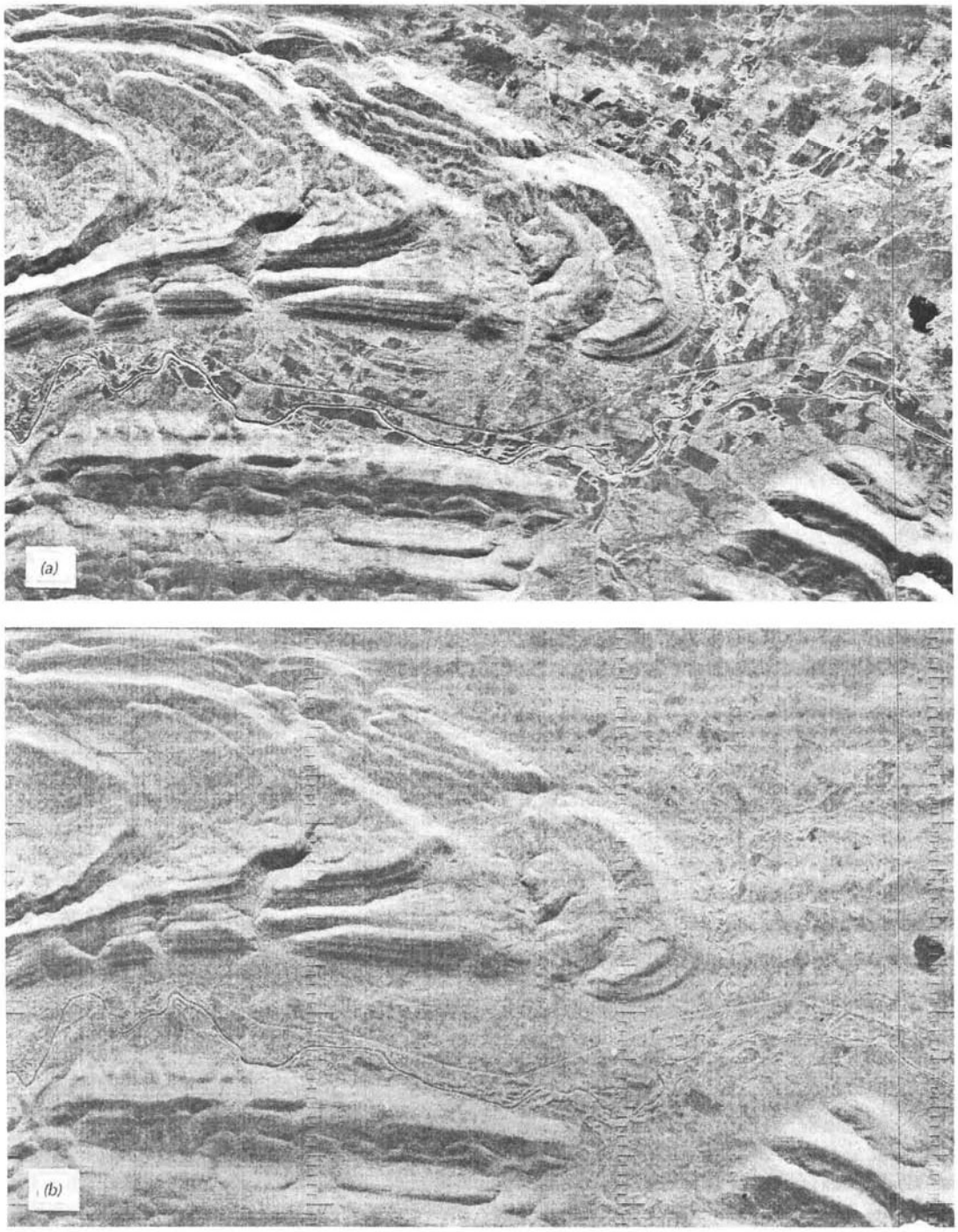

Figure 8.25 SLAR images, Ouachita Mountains, OK, K band, real aperture (scale 1:160,000): (*a*) HH polarization; (*b*) HV polarization. (Courtesy Westinghouse Electric Corp.)

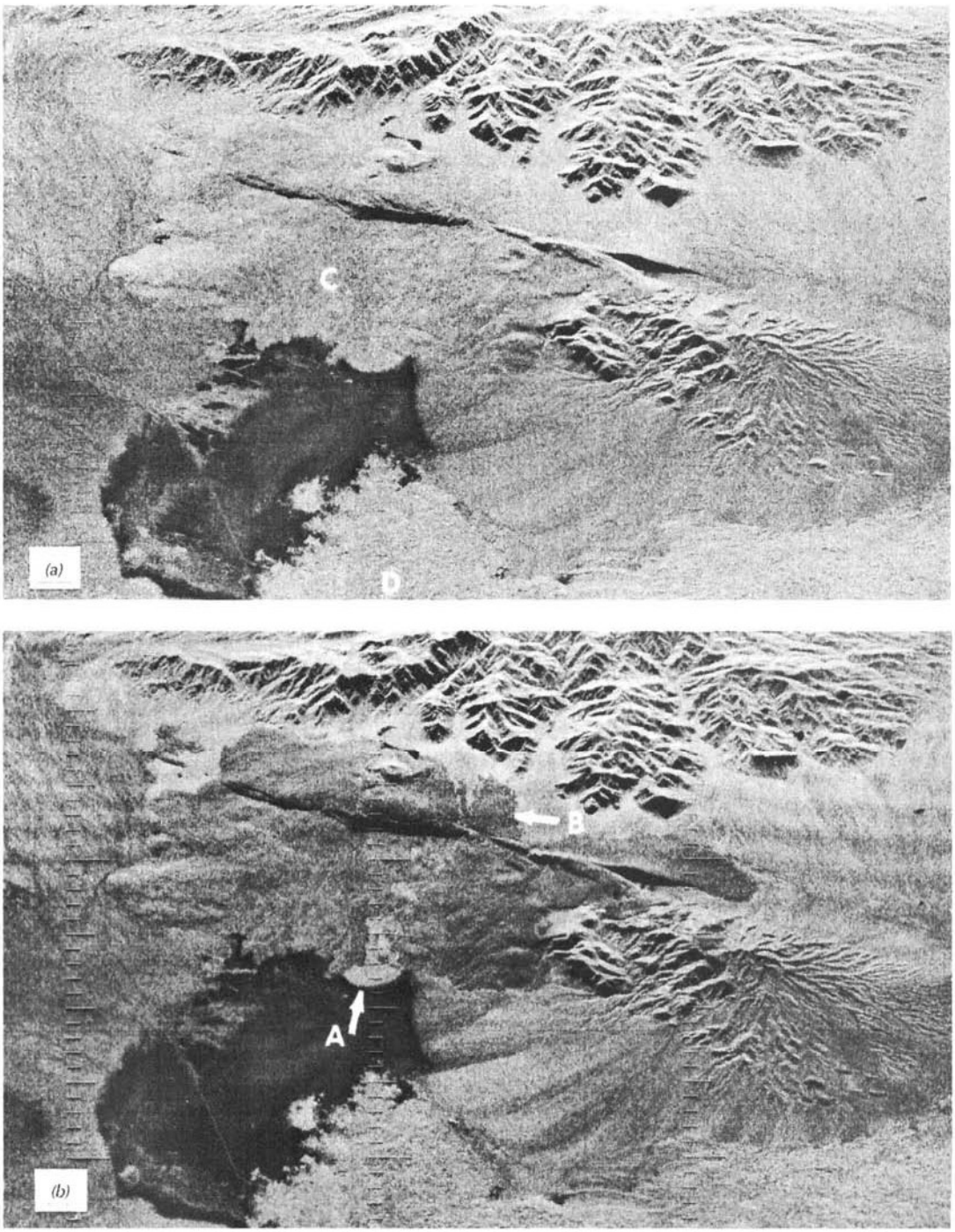

Figure 8.26 SLAR images, Sunshine Crater Area, CA, K band, real aperture (scale 1 : 75,000): (*a*) HH polarization; (*b*) HV polarization. (Courtesy Westinghouse Electric Corp.)

is principally due to the greater density of vegetation on the alluvial fan than on the adjacent Sunshine Basalt flow. The contrast in tones at *B* on the HV image represents the boundary between the lighter toned alluvial materials and the darker toned Sunshine Basalt flows. Note that this boundary is not visible on the HH image. The large dark-toned area at lower left is a playa (dry lakebed) with a mud-cracked clay surface that acts as a specular reflector. The light-toned line running across the playa is a gravel road. Note that the playa is dark toned on both images and the gravel road is light toned.

Soil Response

Because the dielectric constant for water is at least 10 times that for dry soil, the presence of water in the top few centimeters of bare (unvegetated) soil can be detected in radar imagery. Soil moisture and surface wetness conditions become particularly apparent at longer wavelengths. Soil moisture normally limits the penetration of radar waves to depths of a few centimeters. However, signal penetrations of several meters have been observed under extremely dry soil conditions with L-band radar.

Figure 8.27 shows a comparison of Landsat TM (*a*) and spaceborne synthetic aperture radar (*b*) imagery of the Sahara Desert near Safsaf Oasis in southern Egypt. This area, located approximately 190 km west of the lakes shown in Figures 4.26 and 4.27, is largely covered by a thin layer of windblown sand, which obscures many of the underlying bedrock and drainage features. Field studies in the area have shown that L-band (23 cm) radar signals can penetrate up to 2 m through this sand, providing imagery of subsurface geologic features. The dark, braided patterns in (*b*) represent former drainage channels from an ancient river valley, now filled with sand more than 2 m deep. While some of these channels are believed to date back tens of millions of years, other most likely formed during intervals within the past half-million years when the region experienced a wetter climate. Archaeologists working in this area have found stone tools used by early humans more than 100,000 years ago. Other features visible in the radar imagery primarily relate to bedrock structures, which include sedimentary rocks, gneisses, and other rock types. Very few of these features are visible in the Landsat imagery, due to the obscuring sand cover.

Vegetation Response

Radar waves interact with a vegetation canopy as a group of volume scatterers composed of a large number of discrete plant components (leaves, stems, stalks, limbs, etc.). In turn, the vegetation canopy is underlain by soil that may cause surface scattering of the energy that penetrates the vegetation canopy. When the radar wavelengths approximate the mean size of plant components, volume scattering is strong, and if the plant canopy is dense,

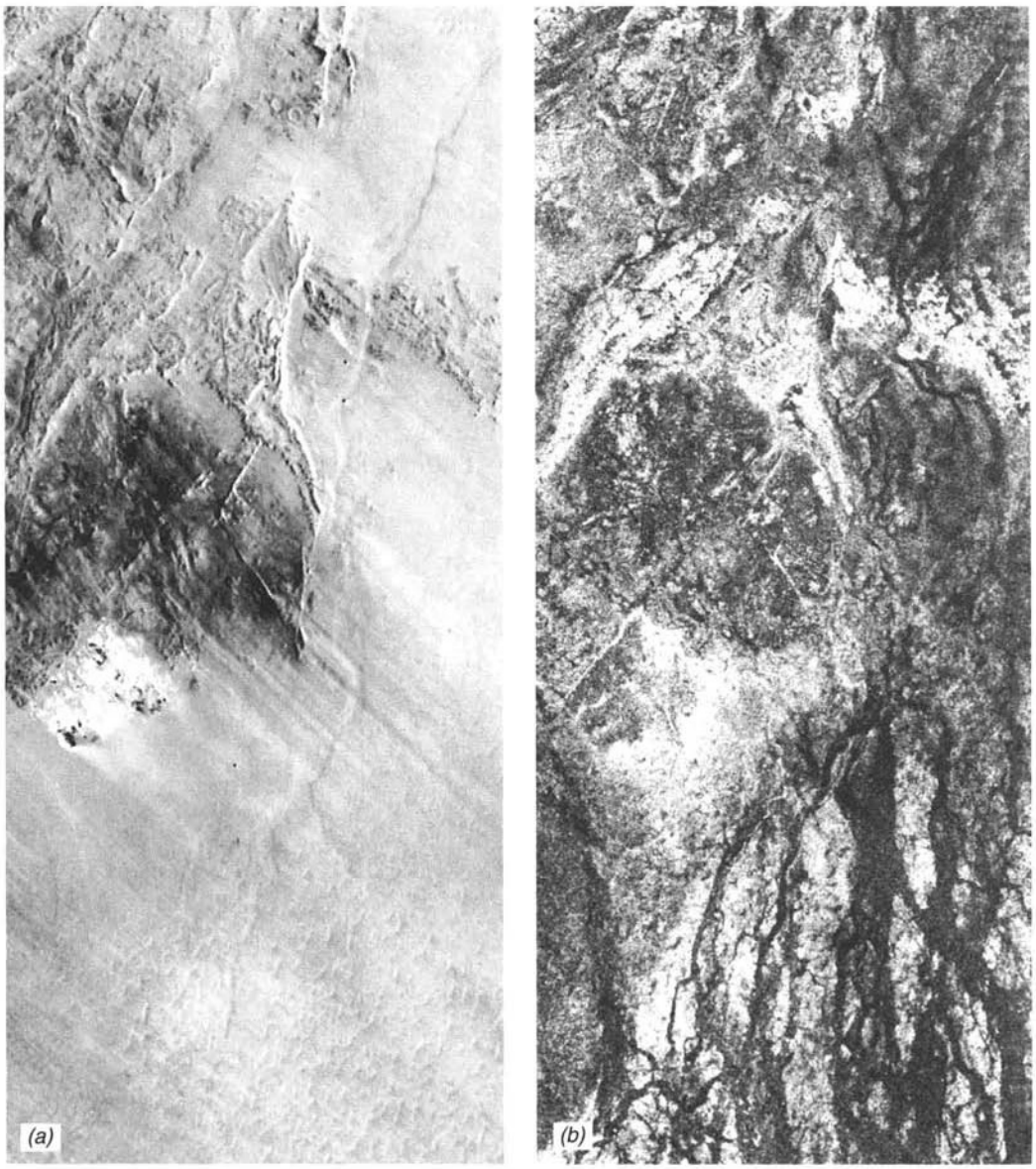

Figure 8.27 Sahara Desert near Safsaf Oasis, southern Egypt: (*a*) Landsat TM image; (*b*) SIR-C image, L band, HH polarization, 45° incident angle. North is to the upper left. Scale 1:170,000. (Courtesy NASA/JPL/Caltech.)

there will be strong backscatter from the vegetation. In general, shorter wavelengths (2 to 6 cm) are best for sensing crop canopies (corn, soybeans, wheat, etc.) and tree leaves. At these wavelengths, volume scattering predominates and surface scattering from the underlying soil is minimal. Longer wavelengths (10 to 30 cm) are best for sensing tree trunks and limbs.

In addition to plant size and radar wavelength, many other factors affect radar backscatter from vegetation. Recall that vegetation with a high moisture content returns more energy than dry vegetation. Also, more energy is returned from crops having their rows aligned in the azimuth direction than from those aligned in the range direction of radar sensing.

Figure 8.28 shows a spaceborne SLR image of a relatively flat area that includes a portion of the Canada/United States border, which appears as an inclined straight line near the bottom of the image. Different agricultural practices emphasize this line, with rangeland predominating in Alberta and wheat fields (at various stages of growth) in Montana. Also clearly evident is the Milk River and its tributaries flowing southeast out of Canada and into the United States.

Figure 8.29 shows a spaceborne SLR image of an agricultural area located in southwest Manitoba. The light-toned circular features are center-pivot irrigation areas with crops that have a much higher moisture content than the nonirrigated crops in the scene. The greater moisture content of the irrigated crops increases the dielectric constant, which in turn increases the reflectivity of the crop surface. That is, leaves with a high moisture content reflect radar waves more strongly than dry leaves of the same plant species. The light-toned

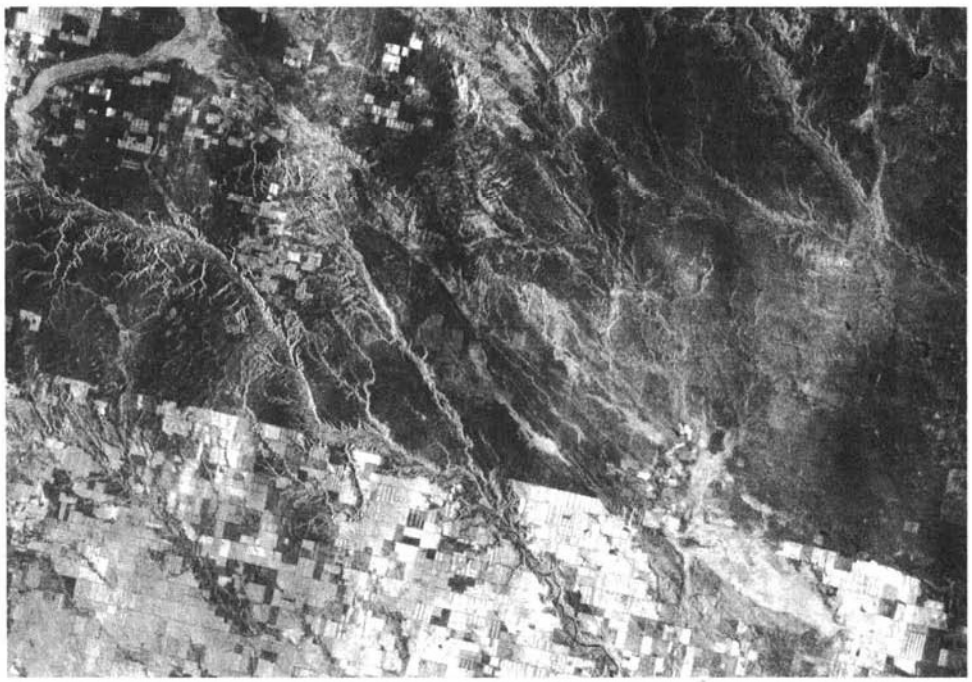

Figure 8.28 ERS-1 radar image, C band, Alberta (Canada)/Montana (United States) border, midsummer. Scale 1 : 700,000. (Copyright © ESA. Courtesy Canada Centre for Remote Sensing.)

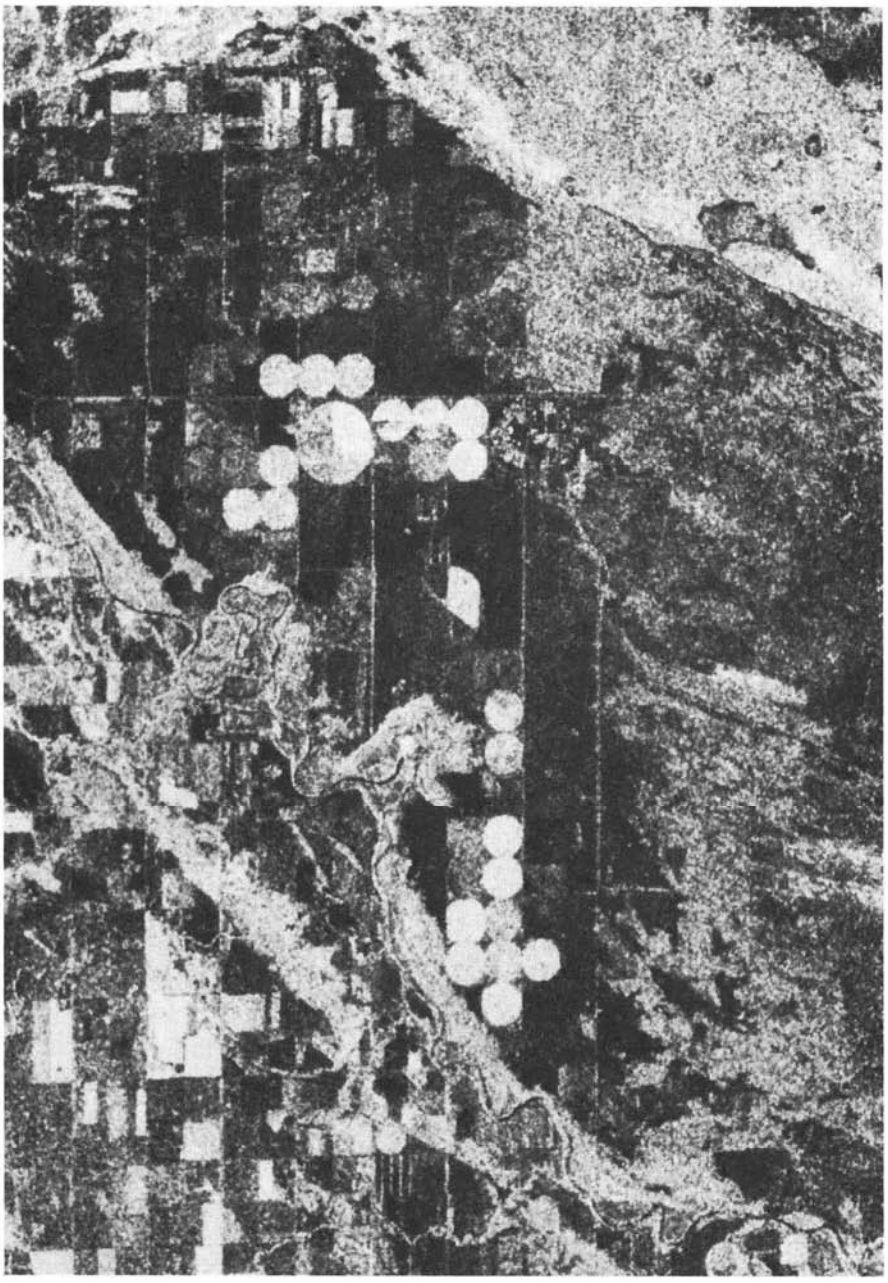

Figure 8.29 ERS-1 radar image, C band, southwest Manitoba, midsummer. Scale 1:180,000. (Copyright © ESA. Courtesy Canada Centre for Remote Sensing.)

area at upper right of Figure 8.29 is a marsh (wetland with grasses, sedges, cattails, and rushes). The brightness of this feature is due both to the increased roughness of the vegetation present and to its increased moisture content. Often, vegetated areas that are flooded can cause a corner reflector effect. Each stalk of vegetation forms a right angle with the calm water. Combined, these can produce a bright radar return, which is a useful indicator of water standing beneath a vegetation canopy (see also Figure 8.32).

Figure 8.30 illustrates the effect of wavelength on the appearance of airborne SAR images. Here, the scene is imaged with three different wave-

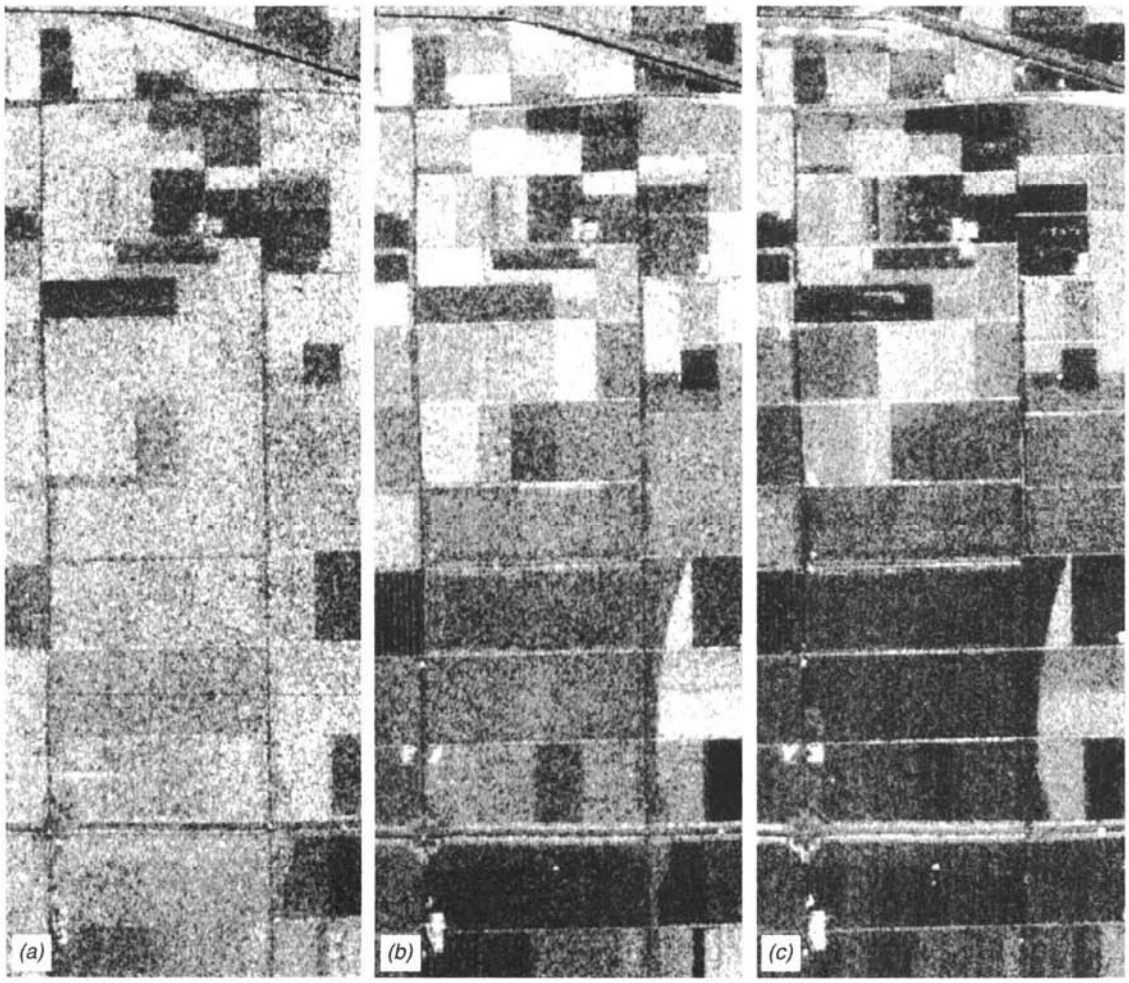

Figure 8.30 Airborne SAR images of an agricultural area in the Netherlands: (*a*) C band (3.75–7.5 cm); (*b*) L band (15–30 cm); (*c*) P band (30–100 cm). HH polarization. (From American Society for Photogrammetry and Remote Sensing, 1998. Images copyright © John Wiley & Sons.)

lengths. Most crop types reflect differently in all three wavelength bands, with generally lighter tones in the C band and darker tones in the P band. Many crop types in this image could be identified by comparing the relative amounts of backscatter in the three different bands.

Figure 8.31 shows a C-band (*a*) and an L-band (*b*) image of an area in northern Wisconsin that is mostly forested, containing many lakes. The look direction is toward the bottom of the images, and the effect of reduced backscatter with increasing range (as described in Section 8.7) can be seen (the near-range ground areas are generally lighter toned than the far-range ground areas). Because of specular reflection from their smooth surfaces, the lakes appear dark throughout both images. A tornado scar can be seen as a dark-toned linear feature running through the center of Figure 8.31*b*, from upper left to lower right. The tornado occurred 10 years before the date of this image. It destroyed many buildings and felled most of the trees in its

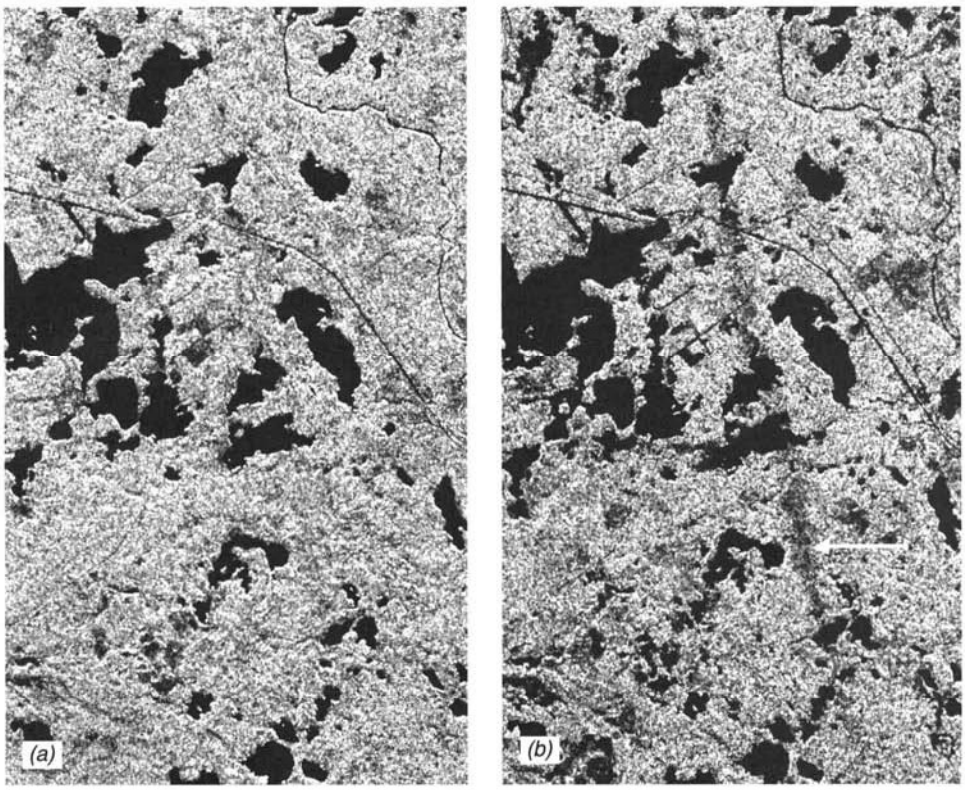

Figure 8.31 SIR-C images of a forested area in northern Wisconsin: (*a*) C-band image; (*b*) L-band image. Scale 1 : 150,000. Note the dark-toned lakes throughout the image and the tornado scar that is visible only in the L-band image. (Courtesy NASA/JPL/Caltech and UW-Madison Environmental Remote Sensing Center.)

path. After the tornado damage, timber salvage operations removed most of the fallen trees, and young trees were established. At the time of acquisition of these spaceborne radar images, the young growing trees in the area of the tornado scar appear rough enough in the C-band (6-cm) image that they blend in with the larger trees in the surrounding forested area. In the L-band (24-cm) image, they appear smoother than the surrounding forested area and the tornado scar can be seen as a dark-toned linear feature.

Incident angle also has a significant effect on radar backscatter from vegetation. Figure 8.32 shows spaceborne SAR images of a forested area in northern Florida and further illustrates the effect of radar imaging at multiple incident angles on the interpretability of radar images. The terrain is flat, with a mean elevation of 45 m. Sandy soils overlay weathering limestone; lakes are sinkhole lakes. Various land cover types can be identified in Figure 8.32*b* by their tone, texture, and shape. Water bodies (W) have a dark tone and smooth texture. Clear-cut areas (C) have a dark tone with a faint mottled texture and rectangular to angular shapes. The powerline right-of-way (P) and roads (R) appear as dark-toned, narrow, linear swaths. Pine forest (F), which covers the majority of this image, has a medium tone with a mottled texture. Cypress-tupelo swamps (S), which consist mainly of deciduous species, have a light tone and a mottled texture. However, the relative tones of the forested areas vary considerably with incident angle. For example, the cypress-tupelo swamp areas are dark toned at an incident angle of 58° and cannot be visually distinguished from the pine forest. These same swamps are somewhat lighter toned than the pine forest at an incident angle of 45° and much lighter toned than the pine forest at an incident angle of 28°. The very high radar return from these swamps on the 28° image is believed to be caused by specular reflection from the standing water in these areas acting in combination with reflection from the tree trunks, resulting in a complex corner reflector effect (Hoffer, Mueller, and Lozano-Garcia, 1985). This effect is more pronounced at an incident angle of 28° than at larger incident angles because the penetration of radar waves through the forest canopy is greater at the smaller angle.

Water and Ice Response

Smooth water surfaces act as specular reflectors of radar waves and yield no returns to the antenna, but rough water surfaces return radar signals of varying strengths. Experiments conducted with the Seasat radar system (L-band system with look angles of 20° to 26°, as described later in Section 8.11) showed that waves with a wavelength greater than 100 m could be detected when wave heights were greater than about 1 m and surface wind speeds exceeded about 2 m/sec (Fu and Holt, 1982). It was also found that waves moving in the range direction (moving toward or away from the radar system) could be detected more readily than waves moving in the azimuth direction.

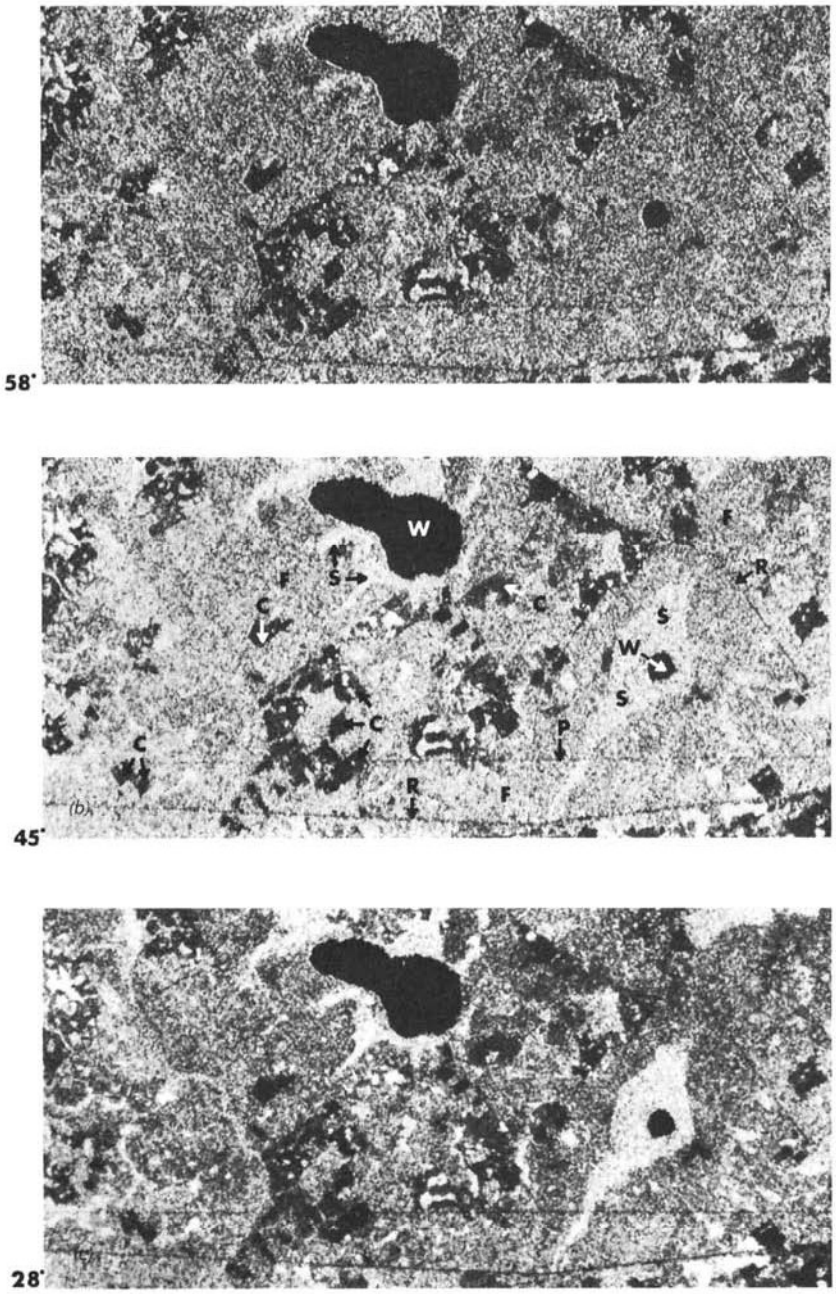

Figure 8.32 SIR-B images, northern Florida, L band (scale 1:190,000): (*a*) 58° incident angle, October 9; (*b*) 45° incident angle, October 10; (*c*) 28° incident angle, October 11. C = clear-cut area; F = pine forest; P = powerline right-of-way; R = road; S = cypress-tupelo swamp; W = open water. (Courtesy Department of Forestry and Natural Resources, Purdue University, and NASA/JPL/Caltech.)

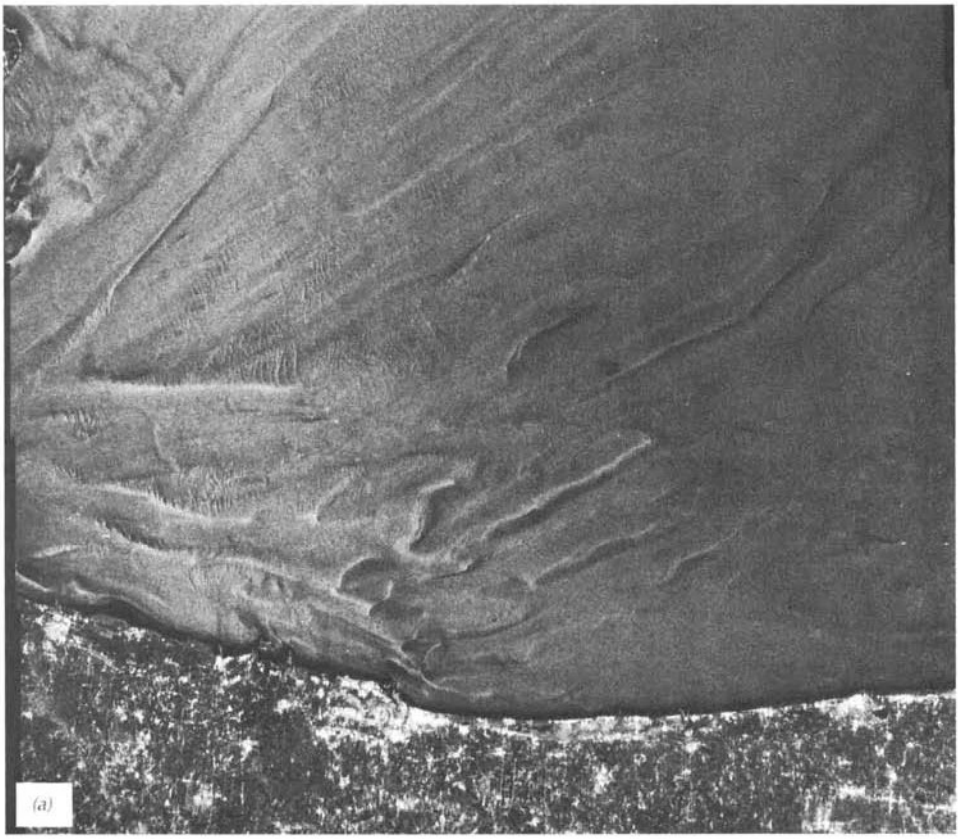

Figure 8.33 English Channel near the Strait of Dover: (*a*) Seasat SAR image, L band, midsummer; (*b*) map showing ocean bottom contours in meters. (Courtesy NASA/JPL/Caltech.)

Radar images from space have revealed interesting patterns that have been shown to correlate with ocean bottom configurations. Figure 8.33*a* is a spaceborne SAR image of the English Channel near the Strait of Dover. Here, the channel is characterized by tidal variations of up to 7 m and reversing tidal currents with velocities at times over 1.5 m/sec. Also, there are extensive sand bars on both sides of the strait and along the coasts of France and England. The sand bars in the channel are long, narrow ridges from 10 to 30 m in depth, with some shallower than 5 m. Together with the high volume of ship traffic, these sand bars make navigation in the channel hazardous. By comparing this image with Figure 8.33*b*, it can be seen that the surface patterns on the radar image follow closely the sand bar patterns present in the area. Tidal currents at the time of image acquisition were 0.5 to 1.0 m/sec, generally in a northeast-to-southwest direction. The more prominent patterns are visible over bars 20 m or less in depth.

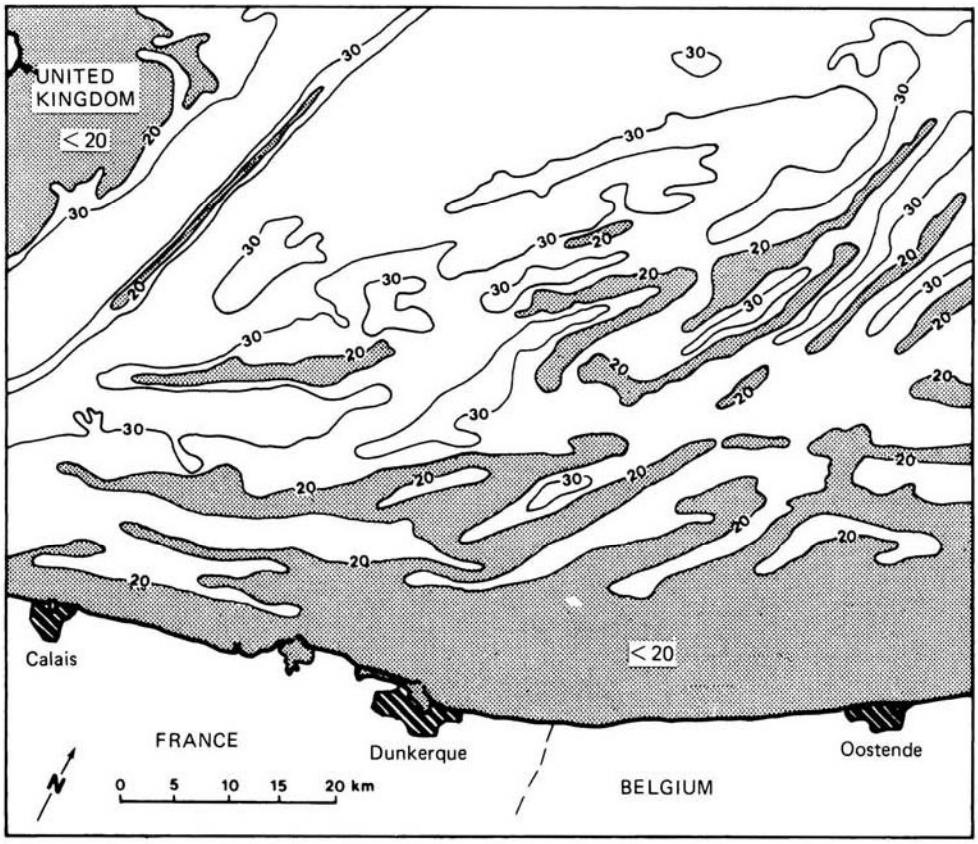

(b)

Figure 8.33 *(Continued)*

Radar backscatter from ice is dependent on the dielectric properties and spatial distribution of the ice. In addition, such factors as ice age, surface roughness, internal geometry, temperature, and snow cover also affect radar backscatter. X- and C-band radar systems have proven useful in determining ice types and, by inference, ice thickness. L-band radar is useful for showing the total extent of ice, but it is often not capable of discriminating ice type and thickness. (See Figure 8.49 for radar images of several forms of ice.)

Urban Area Response

As illustrated in Figure 8.34, urban areas typically appear light toned in SLR images because of their many corner reflectors.

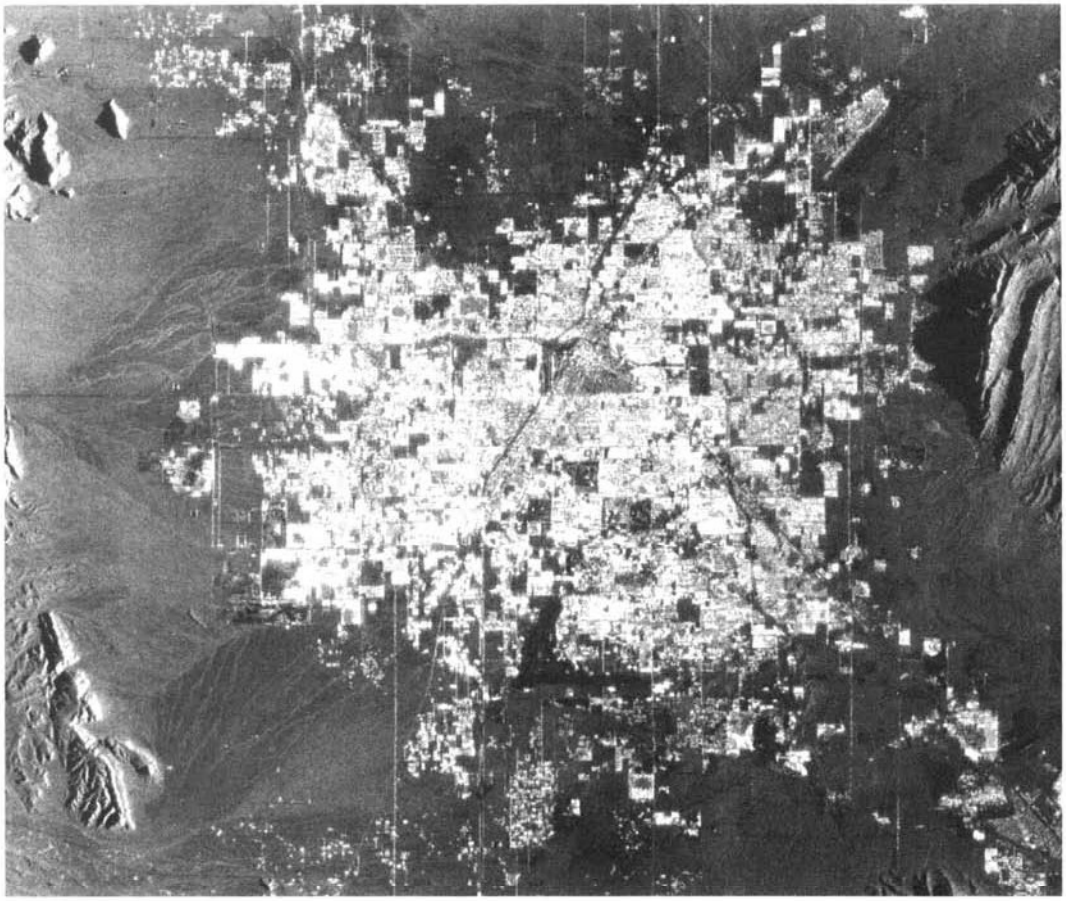

Figure 8.34 Airborne SAR image, Las Vegas, NV, X band, HH polarization. North is to the top, the look direction is from the right. Scale 1 : 250,000. (From American Society for Photogrammetry and Remote Sensing, 1998. Images copyright © John Wiley & Sons.)

Figure 8.35, an airborne SAR image of Sun City, Arizona, illustrates the effect of urban building orientation on radar reflection. The "corner reflection" from buildings located on the part of the circular street system where the wide faces of the houses (front and rear) face the direction from which the radar waves have originated provides the strongest radar returns. At right angles to this direction, there is again a relatively strong radar return where the sides of the houses face the direction from which the radar waves have originated. This effect is sometimes called the *cardinal effect*, a term that has survived from the early days of radar remote sensing. At that time, it was noted that reflections from urban areas, often laid out according to the cardinal directions of a compass, caused significantly larger returns when the linear features were illuminated at an angle orthogonal to their orientation,

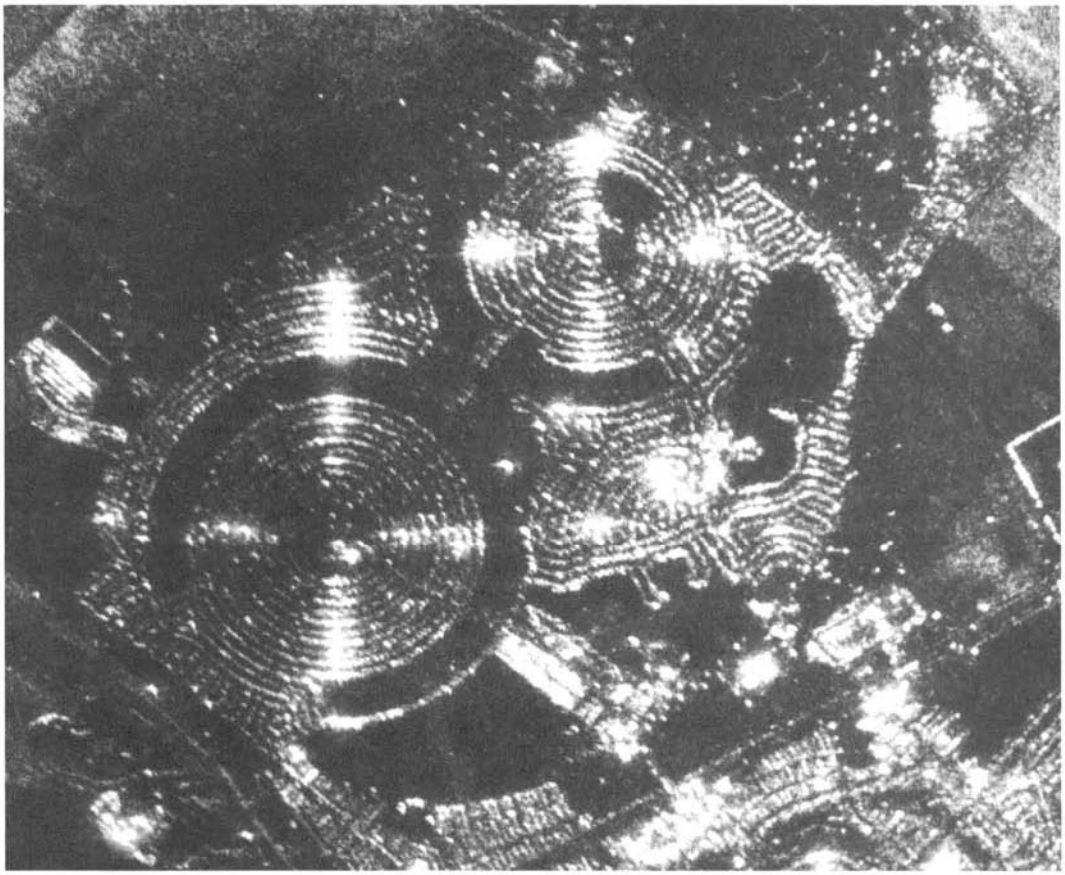

Figure 8.35 Airborne SAR image, Sun City, AZ, X band. The look direction is from the top of the image. Scale 1 : 28,000. (From American Society for Photogrammetry and Remote Sensing, 1998. Images copyright © John Wiley & Sons.)

hence the name cardinal effect (Raney, 1998). Other earth surface features also respond with a similar effect. For example, the orientation of row crops affects their response, as described in Section 8.8, and the orientation of ocean waves also strongly affects their response.

Summary

In summary, as a generalization, larger SLR return signals are received from slopes facing the aircraft, rough objects, objects with a high moisture content, metal objects, and urban and other built-up areas (resulting from corner reflections). Surfaces acting as diffuse reflectors return a weak to moderate signal

and may often have considerable image texture. Low returns are received from surfaces acting as specular reflectors, such as smooth water, pavements, and playas (dry lakebeds). No return is received from radar "shadow" areas.

8.9 INTERFEROMETRIC RADAR

As discussed in Section 8.5, the presence of differential relief displacement in overlapping radar images acquired from different flight lines produces image parallax. This is analogous to the parallax present in aerial photographs or electro-optical scanner data. Just as photogrammetry can be used to measure surface topography and feature heights in optical images, radargrammetry can be used to make similar measurements in radar images.

In recent years, much attention has been paid to an alternative method for topographic mapping with radar. *Imaging radar interferometry* is based on analysis of the phase of the radar signals as received by two antennas located at different positions in space. As shown in Figure 8.36, the radar signals returning from a single point P on the earth's surface will travel slant-range distances r_1 and r_2 to antennas A_1 and A_2, respectively. The difference between

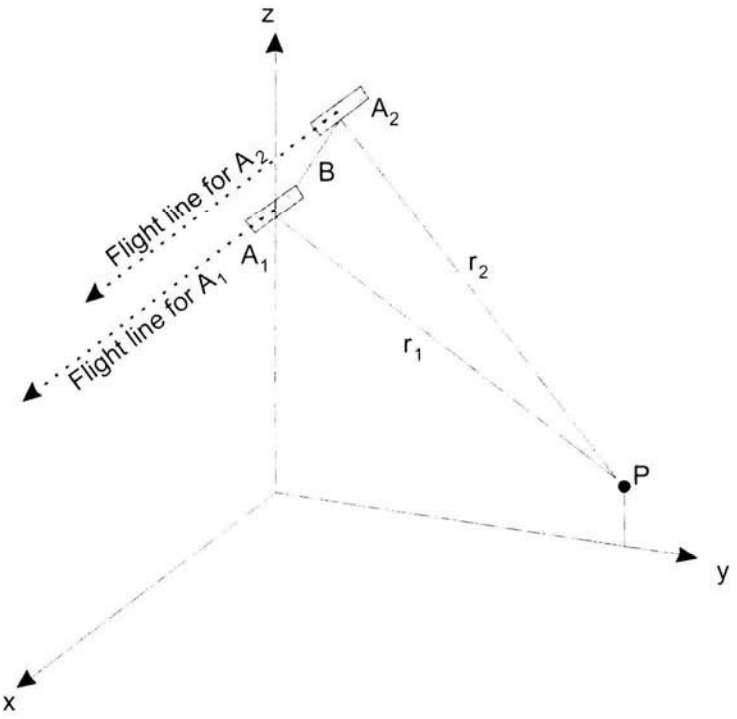

Figure 8.36 Interferometric radar geometry.

lengths r_1 and r_2 will result in the signals being out of phase by some phase difference ϕ, ranging from 0 to 2π radians. If the geometry of the *interferometric baseline* (B) is known with a high degree of accuracy, this phase difference can be used to compute the elevation of point P.

Figure 8.37 illustrates the interferometric determination of earth's surface elevations. Figure 8.37*a* is a SAR image of a large volcano. Figure 8.37*b* shows an *interferogram*, which displays the phase difference values for each pixel of an interferometric radar data set. The resulting interference pattern consists of a series of stripes, or *fringes*, that represent differences in surface height and sensor position. When the effect of sensor position is removed, a *flattened interferogram* is produced in which each fringe corresponds to a particular elevation range (Figure 8.37*c*).

There are several different approaches to collecting interferometric radar data. In the simplest case, referred to as *single-pass interferometry*, two antennas are located on a single aircraft or satellite platform. One antenna acts as both a transmitter and receiver, while the second antenna acts only as a

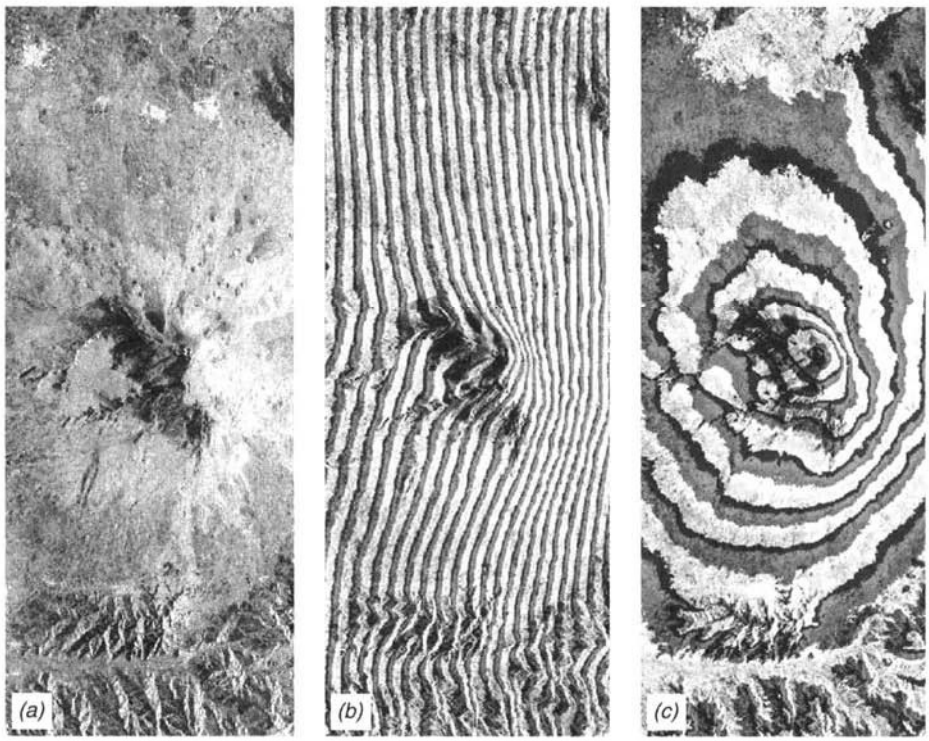

Figure 8.37 Radar image and radar interferograms: (*a*) SIR-C radar image, Mt. Etna, Italy; (*b*) raw interferogram; (*c*) flattened interferogram showing elevation ranges. Parts (*b*) and (*c*) are black and white reproductions of color interferograms. (Courtesy NASA/JPL/Caltech and USGS EROS Data Center.)

receiver. In this case, as shown in Figure 8.36, the interferometric baseline is the physical distance between the two antennas. Alternatively, in *repeat-pass interferometry*, an aircraft or satellite with only a single radar antenna makes two or more passes over the area of interest, with the antenna acting as both a transmitter and receiver on each pass. The interferometric baseline is then the distance between the two flight lines or orbital tracks. It is generally desirable to have the sensor pass as close as possible to its initial position, to keep this baseline small. For airborne repeat-pass interferometry, the flight lines should generally be separated by no more than tens of meters, while for spaceborne systems this distance can be as much as hundreds or thousands of meters.

In repeat-pass interferometry, the position and orientation of objects on the surface may change substantially between passes, particularly if the passes are separated by an interval of days or weeks. This results in a situation known as *temporal decorrelation* in which precise phase matching between the two signals is degraded. For example, in a forested area the individual leaf elements at the top of the canopy may change position due to wind action over the course of a single day. For a short wavelength system such as an X-band SAR, which is highly sensitive to individual leaves and other small features, this decorrelation may limit the use of repeat-pass interferometry substantially. In more arid landscapes, where vegetation is sparse, temporal decorrelation will be less of a problem. Likewise, longer wavelength interferometric radar systems will tend to be less affected by temporal decorrelation than will systems using shorter wavelengths. The use of single-pass interferometry avoids the problem of surface change between passes, so that decorrelation is not a problem.

In some cases, repeat-pass interferometry can actually be used to study surface changes that have occurred between the two passes. In addition to the "before" and "after" images, this approach—known as *differential interferometry*—also requires prior knowledge about the underlying topography. This can be in the form of an existing digital elevation model (DEM), but errors in the DEM will lead to incorrect estimates of surface change. A better approach is to acquire one interferometric image pair from the period before the surface change occurs, for use in combination with a third image acquired after the change. In either case, the phase difference between the before and after images can be corrected to account for topography, with the residual phase differences then representing changes in the position of features on the surface. If the interferometric correlation between the two images is high, these changes can be accurately measured to within a small fraction of the radar system's wavelength—often to less than 1 cm. With a single pair of images, surface changes are measured only as line-of-sight displacements, meaning that only the degree to which a point moved toward or away from the radar look direction can be measured. If two sets of interferometric image pairs

are available from different look directions, such as from the ascending and descending segments of a satellite's orbit, the two-dimensional movement of the surface can be derived.

This approach works best for changes that affect large areas in a spatially correlated manner, such as the entire surface of a glacier moving downhill, as opposed to changes that occur in a spatially disjointed manner, such as the growth of trees in a forest. Plate 36 illustrates the use of interferometric radar to monitor continuing ground uplift caused by magma accumulation at depth. Scientists from the USGS Cascades Volcano Observatory, in connection with other agencies, have confirmed the slow uplift of a broad area centered about 5 km west of South Sister volcano in the central Oregon Cascade Range. The radar interferogram shown in Plate 36 was produced using radar data from the European Space Agency's ERS satellites. In this interferogram, each full color band from blue to red represents about 2.8 cm of ground movement in the direction of the radar satellite. (No information is available for the uncolored areas, where forest vegetation, or other factors, hinders the acquisition of useful radar data.) The four concentric bands show that the ground surface moved toward the satellite by as much as 10 cm between August 1996 and October 2000. Surface uplift caused by magma accumulation at depth can be a precursor to volcanic activity at the earth's surface.

Another example of differential interferometry is illustrated in Plate 37. This differential interferogram, derived from ERS-1 and ERS-2 images, shows surface displacement between April 1992 and December 1997 in the area around Las Vegas, Nevada. For most of the past century, pumping of groundwater from an underground aquifer for domestic and commercial consumption has caused land subsidence at a rate of several centimeters per year in Las Vegas, with significant damage to the city's infrastructure. In recent years, artificial recharge of groundwater has been used in an attempt to reduce subsidence. Analysis of the interferometric radar imagery in combination with geologic maps shows that the spatial extent of subsidence is controlled by geologic structures (faults, indicated by white lines in Plate 37) and sediment composition (clay thickness). The maximum detected subsidence during the 1992 to 1997 period was 19 cm. Other potential applications of differential radar interferometry include monitoring the movement of glaciers and ice sheets, measuring displacement across faults after earthquakes, and detecting land subsidence due to oil extraction, mining, and other activities.

8.10 RADAR REMOTE SENSING FROM SPACE

Several satellites have provided operational radar remote sensing from space, including the Almaz-1 system of the former Soviet Union, the ERS-1, ERS-2, and Envisat systems of the European Space Agency, Japan's JERS-1 system, and Canada's Radarsat system.

Among the precursors to these systems were the experimental spaceborne systems Seasat-1 and three Shuttle Imaging Radar systems (SIR-A, SIR-B, and SIR-C). More recently, the Shuttle Radar Topography Mission (SRTM) employed the SIR-C antenna for a brief but highly productive operational program to map global topography using radar interferometry.

In general, images acquired at small incident angles (less than 30°) emphasize variations in surface slope, although geometric distortions due to layover and foreshortening in mountainous regions can be severe. Images with large incident angles have reduced geometric distortion and emphasize variations in surface roughness, although radar shadows increase.

A limitation in the use of airborne radar imagery is the large change in incident angle across the image swath. In these circumstances, it is often difficult to distinguish differences in backscatter caused by variations in incident angle from those actually related to the structure and composition of the surface materials present in an image. Spaceborne radar images overcome this problem because they have only small changes in incident angle. This makes their interpretation less difficult.

Because radar is an active sensor that can gather data both day and night, radar images may be acquired during both a south-to-north (ascending) orbital direction and a north-to-south (descending) orbital direction. A "right-looking" sensor will face east during an ascending orbit and west during a descending orbit. (The opposite is true for a left-looking sensor.)

Some spaceborne systems (e.g., Radarsat and Envisat) use a *ScanSAR* imaging mode in which the radar beam is electronically steered back and forth in the range direction to cover a wider area. In effect, the beam illuminates two or more separate swaths in alternation, with the far-range side of the first swath being contiguous with the near-range side of the second swath, and so on. The multiple swaths are then processed to form a single, wide image. The disadvantage of ScanSAR mode is that the spatial resolution is reduced.

An additional imaging mode, referred to as *Spotlight*, involves steering the radar beam in azimuth rather than in range, in order to dwell on a given site for a longer period of time. As the satellite approaches the target area, the beam is directed slightly forward of the angle at which it is normally transmitted; then, while the satellite moves past, the beam swings back to continue covering the target area. Through an extension of the synthetic aperture principle, this Spotlight mode allows a finer resolution to be achieved by acquiring more "looks" over the target area from a longer segment of the orbit path. This increase in resolution comes at the expense of continuous coverage because while the antenna is focusing on the target area it is missing the opportunity to image other portions of the ground swath. The SIR-C radar mission provided the first tests of both ScanSAR and Spotlight modes from space.

8.11 SEASAT-1

Seasat-1 was the first of a proposed series of satellites oriented toward oceanographic research. The Seasat-1 satellite was launched on June 27, 1978, into an 800-km near-polar orbit. The satellite was designed to provide alternating day and night coverage each 36 hr. Approximately 95 percent of the earth's oceans were to be covered by the system. Unfortunately, prime power system failure 99 days after launch limited the image data produced by the satellite.

An important "first" realized with Seasat-1 was a spaceborne L-band (23.5-cm) SLR system with HH polarization. It was designed to generate imagery across a 100-km swath with a look angle of 20° to 26° and four-look 25 m resolution in both range and azimuth. Table 8.4 summarizes these characteristics (as well as those of the SIR systems).

Although the primary rationale for placing the imaging radar system on board Seasat was its potential for monitoring the global surface wave field and polar sea ice conditions, the resultant images of the oceans revealed a much wider spectrum of oceanic and atmospheric phenomena, including internal waves, current boundaries, eddies, fronts, bathymetric features, storms, rainfalls, and windrows. Seasat was also operated over the world's land areas, and many excellent images illustrating applications to geology, water resources, land cover mapping, agricultural assessment, and other land-related uses were obtained.

Figures 8.3 and 8.33 (described previously) are examples of Seasat-1 imagery.

TABLE 8.4 Characteristics of Major Experimental Synthetic Aperture Radar Systems

Characteristic	Seasat-1	SIR-A	SIR-B	SIR-C
Launch date	June 1978	November 1981	October 1984	April 1994 October 1994
Length of mission	99 days	3 days	8 days	10 days
Nominal altitude, km	800	260	225	225
Wavelength band	L band	L band	L band	X band (X-SAR) C and L bands (SIR-C)
Polarization	HH	HH	HH	HH, HV, VV, VH (X band HH only)
Look angle	20–26° (fixed)	47–53° (fixed)	15–60° (variable)	15–60° (variable)
Swath width, km	100	40	10–60	15–90
Azimuth resolution, m	25	40	25	25
Range resolution, m	25	40	15–45	15–45

8.12 SHUTTLE IMAGING RADAR

A number of early spaceborne radar experiments were conducted using SIR systems—SIR-A in 1981 and SIR-B in 1984. Two SIR-C missions were conducted in 1994. Table 8.4 summarizes the characteristics of these three systems.

SIR-A

The SIR-A experiments were conducted from the Space Shuttle during November 1981. This was the second flight of the Space Shuttle, and the first scientific payload ever flown. The SIR-A system possessed many of the same characteristics as the radar system onboard Seasat. The principal difference between these two was that the SIR-A antenna (9.4 m long) illuminated the earth's surface at a larger look angle (47° to 53°) than Seasat. As with Seasat, an L-band (23.5-cm) system with HH polarization was used. The swath width imaged was 40 km and resolution was 40 m in both range and azimuth. SIR-A obtained imagery over 10 million km^2 of the earth's surface and acquired radar images of many tropical, arid, and mountainous regions for the first time.

Figure 8.38 shows a Landsat MSS band 7 (near-IR) image (*a*) and a SIR-A image (*b*) of an area in the Widyan region of Saudi Arabia and Iraq. This is an area of rugged terrain composed of extensively dissected carbonate rocks (several types of limestone and dolomite). Numerous dry river channels in the area form the regional drainage network. The dry river beds are covered with smooth, dry layers of wind-deposited silt and sand that produce very low radar returns. The outcropping carbonate rocks adjacent to the river beds have rough angular surfaces that produce strong radar returns. The contrast between the light-toned carbonate rocks and the dark-toned dry river beds provides ready discrimination of the dendritic drainage pattern on the radar image. The Landsat image of this area shows little contrast between the river beds and the adjacent carbonate bedrock.

Figure 8.39 is a SIR-A image showing villages, roads, and cultivated fields in eastern China. Each of the hundreds of white spots on this image is a village. The agricultural crops common in this area are winter wheat, kaoliang, corn, and millet. The dark linear and winding features with white lines on each side are rivers and drainageways located between levees.

SIR-B

The SIR-B experiments were conducted from the Space Shuttle during October 1984. Again, an L-band system with HH polarization was used. The prin-

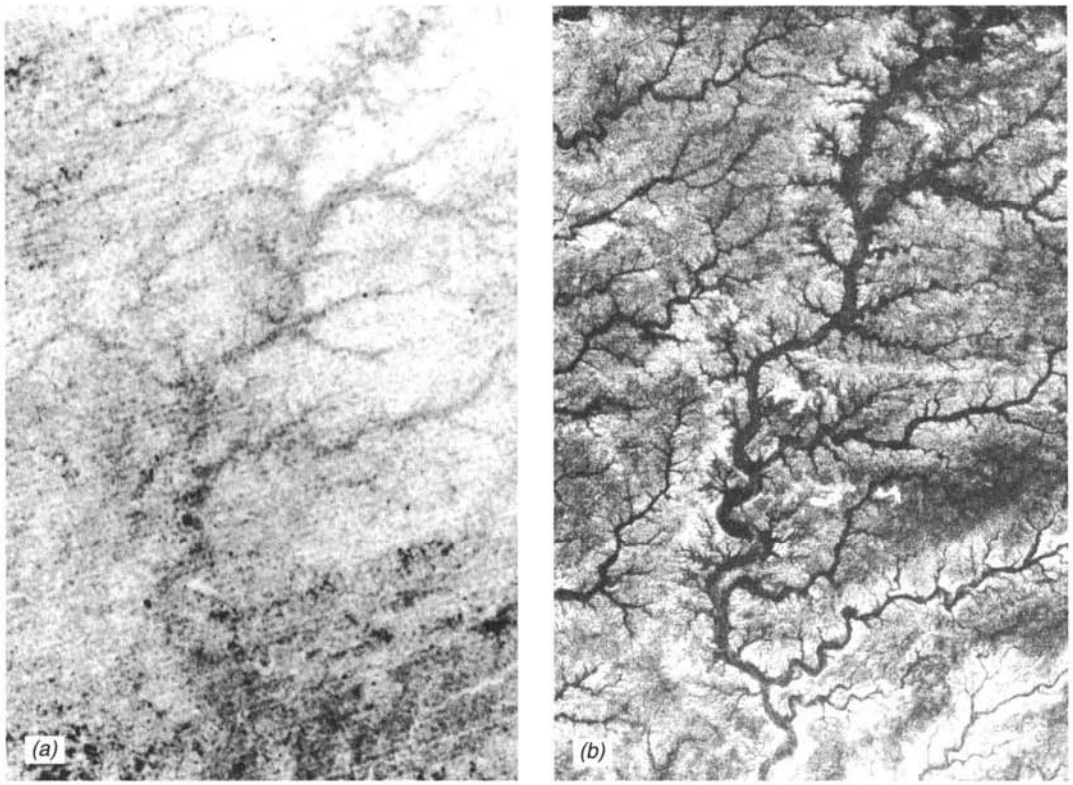

Figure 8.38 Widyan region of Saudi Arabia and Iraq: (*a*) Landsat MSS band 7 image (0.8–1.1 μm), July 1973; (*b*) SIR-A image, L band, November 1981 (scale 1 : 485,000). (Courtesy NASA/JPL/Caltech.)

cipal difference between the SIR-A and SIR-B radar systems is that SIR-B was equipped with an antenna that could be tilted mechanically to beam its radar signals toward the earth at varying look angles (ranging from 15° to 60°). This provided the opportunity for scientific studies aimed at assessing the effect of various incident angles on radar returns. In addition, it provided the opportunity for the acquisition of stereo radar images. The azimuth resolution of SIR-B was 25 m. The range resolution varied from 15 m at a look angle of 60° to 45 m at a look angle of 15°.

Figure 8.40 shows SIR-B images of Mt. Shasta, a 4300-m-high volcano in northern California. These images illustrate the effect of incident angle on elevation displacement. In Figure 8.40*a*, having an incident angle of 60°, the peak of the volcano is imaged near its center. In Figure 8.40*b*, having an incident angle of 30°, the peak is imaged near the top of the figure (the look direction was from top to bottom in this figure). Several light-toned tongues of lava can be seen on the flanks of this strato volcano. The surface of the young lava flow seen at upper left in this radar image consists of unvegetated angular

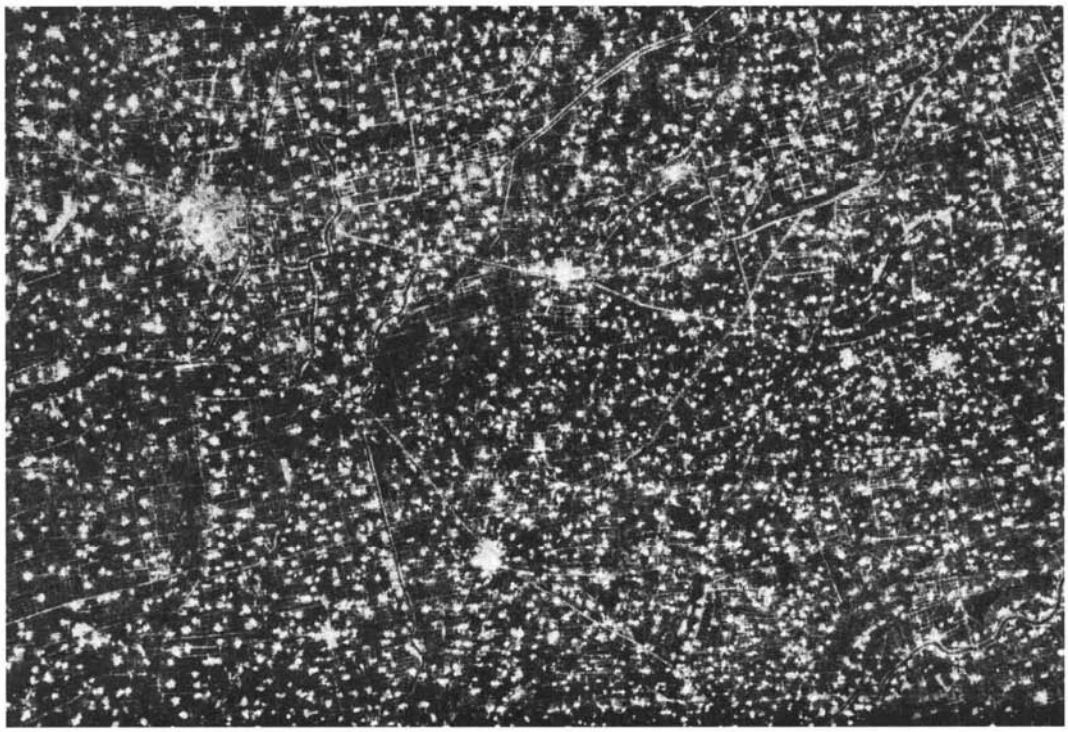

Figure 8.39 SIR-A image of eastern China, L band. Scale 1 : 530,000. (Courtesy NASA/JPL/Caltech.)

chunks of basalt $\frac{1}{3}$ to 1 m in size that present a very rough surface to the L-band radar waves. The other, somewhat darker toned lava flows on the flanks of Mt. Shasta are older, have weathered more, and are more vegetated.

The image parallax associated with data from two different incident angles can be used not only to generate stereopairs of radar data but also to prepare topographic maps and digital elevation models of the imaged terrain. For example, Figure 8.41 shows 12 perspective views of Mt. Shasta that were generated from a digital elevation model extracted from the radar data shown in Figures 8.40*a* and *b*. Image parallax was achieved by same-side illumination using the same altitude but different look angles (Section 8.5). Through computer modeling, perspective views from various vantage points around the mountain were calculated for this display.

SIR-C

SIR-C missions were conducted in April and October 1994. SIR-C was designed to explore multiple-wavelength radar sensing from space. Onboard

SIR-C were L-band (23.5-cm) and C-band (5.8-cm) systems from NASA and an X-band (3.1-cm) system (known as X-SAR) from a consortium of the German Space Agency (DARA) and the Italian Space Agency (ASI). The multiple wavelength bands available allowed scientists to view the earth in up to three wavelength bands, either individually or in combination. SIR-C look angles were variable in one-degree increments from 15° to 60°, and four polarizations were available (HH, HV, VV, and VH).

The scientific emphasis in selecting sites for SIR-C image acquisition was on studying five basic themes—oceans, ecosystems, hydrology, geology, and rain and clouds. Ocean characteristics studied included large surface and internal waves, wind motion at the ocean surface, and ocean current motion, as well as sea ice characteristics and distribution. Ecosystem characteristics studied included land use, vegetation type and extent, and the effects of fires, flooding, and clear cutting. Hydrologic studies focused on water and wetland conditions, soil moisture patterns, and snow and glacier cover. Geologic applications included mapping geologic structures (including those buried under dry sand), studying soil erosion, transportation and deposition, and monitoring active volcanoes. Also under study was the attenuation of radar signals at X-band and C-band wavelengths by rain and clouds.

Figure 8.42 is an example of SIR-C imagery. In this black-and-white reproduction of a three-band, multipolarization image, the sinuous dark area crossing the image from lower right to upper left is the Missouri River. The narrow light-toned area on both sides of the river channel is its natural levee. The darker toned band several times wider than the river is its low-lying floodplain. The heavily dissected uplands on both sides of the floodplain can be seen at lower left and upper right, covering more than one-half of the image.

NASA's Jet Propulsion Laboratory (JPL) has released many color-composite SIR-C images from around the world (see Appendix B for website address). Three different wavelength–polarization combinations are used to produce these images, with one combination displayed as blue, one as green, and one as red. If the different wavelength–polarization images show reflection from different features with different intensities, then these features are displayed with different colors. This can be seen in Plate 38, which shows a volcano-dominated landscape in central Africa; parts of Rwanda, Uganda, and the Democratic Republic of the Congo (formerly Zaire) are each present in this image. In this image, C-band data with HH polarization are displayed as blue, C-band data with HV polarization are displayed as green, and L-band data with HV polarization are displayed as red. The volcano at top center is Karisimba, 4500 m high. The green band on the lower slopes of Karisimba volcano, to the right of its peak, is an area of bamboo forest, one of the world's few remaining natural habitats for mountain gorillas. Just right of the center of the image is Nyiragongo volcano, an active volcano 3465 m high. The lower portion of the image is dominated by Nyamuragira volcano,

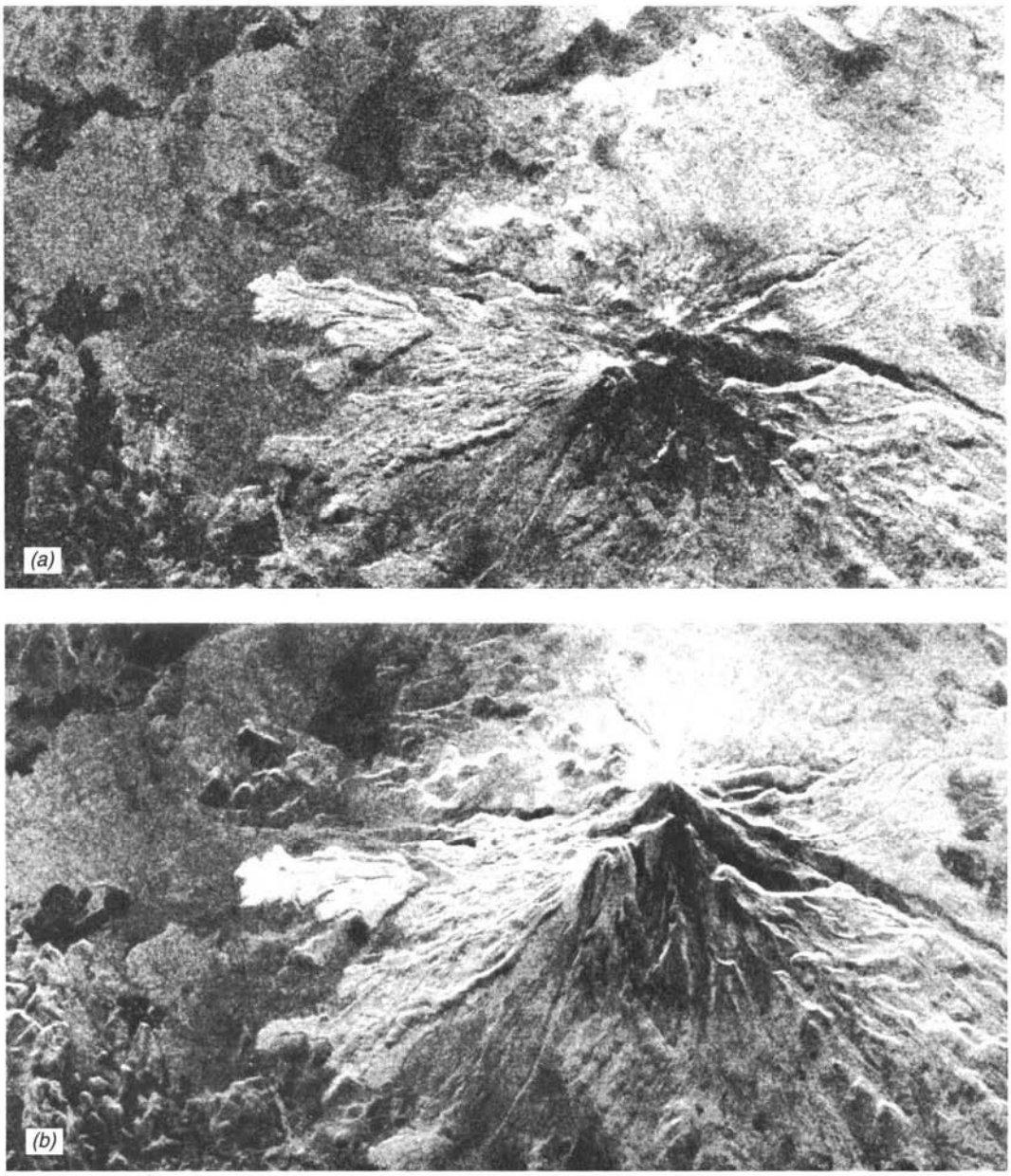

Figure 8.40 SIR-B images, Mt. Shasta, CA, L band, mid-fall (scale 1 : 240,000): (*a*) 60° incident angle; (*b*) 30° incident angle. Note the severe layover of the mountain top in (*b*). (Courtesy NASA/JPL/Caltech.)

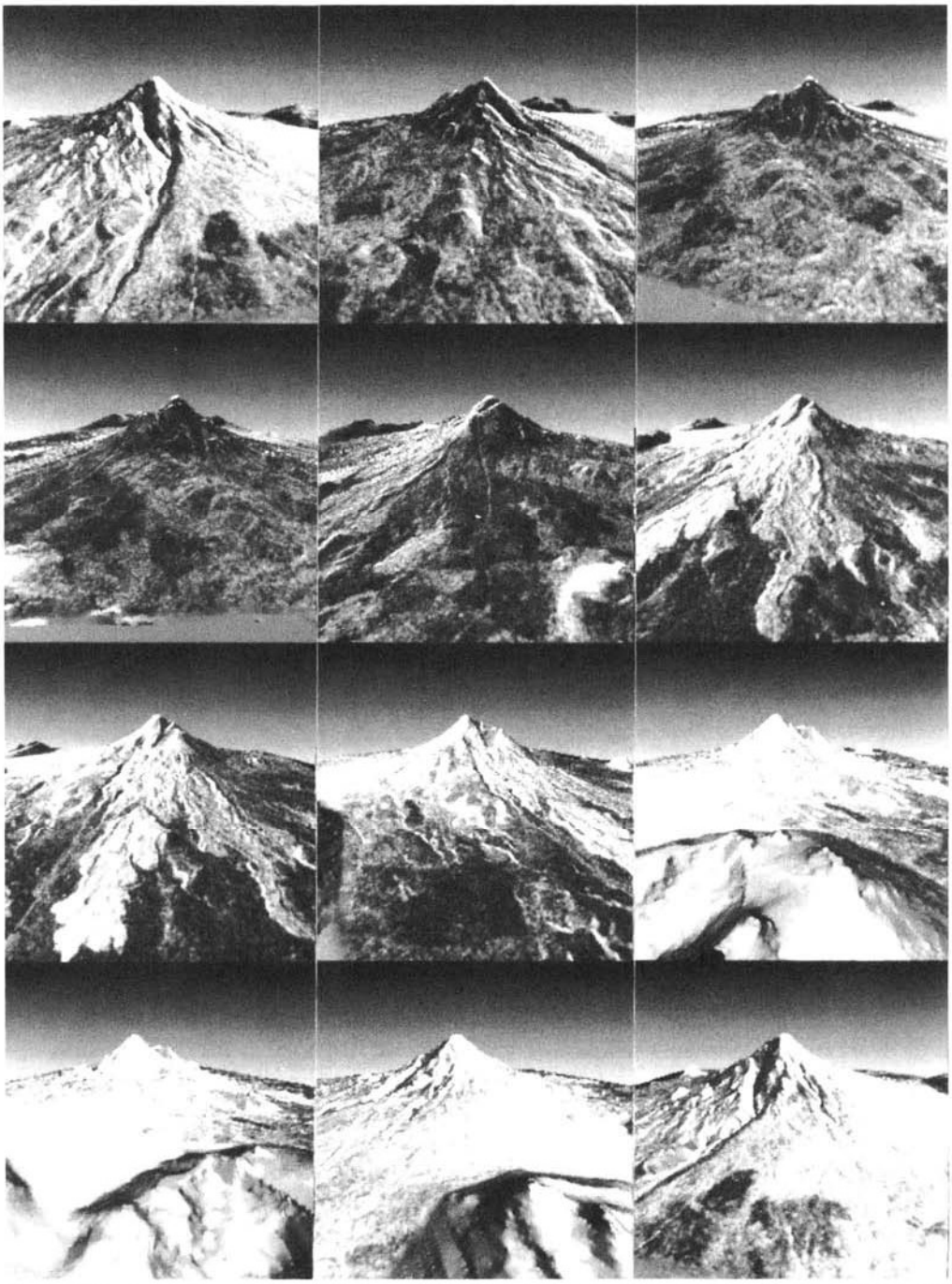

Figure 8.41 Perspective views of Mt. Shasta, CA, generated from the SIR-B data shown in Figure 8.40*a* and *b*. (Courtesy NASA/JPL/Caltech.)

Figure 8.42 SIR-C image, Missouri River near Glasgow, MO. Black and white reproduction of a three-band color composite image (L band HH, L band HV, and L band HH + HV). North is to the bottom of the image. Scale 1 : 220,000. (Courtesy NASA/JPL/Caltech.)

3053 m high, and the many lava flows (purple in this image) that issue from its flanks.

Plate 39 shows SIR-C imagery of a portion of Yellowstone National Park in Wyoming. Yellowstone was the world's first national park and is known for its geological features, including geysers and hot springs. The park and the surrounding region also provide habitat for populations of grizzly bears, elk, and bison. In 1988, massive forest fires burned across some 3200 km^2 within the park. The intensity of the burn varied widely, leaving a complex mosaic of heavily burned, lightly burned, and unburned areas that will continue to dominate the park's landscape for decades. The effects of these fires can be clearly seen in the L_{VH}-band SIR-C image (*a*), acquired on October 2, 1994.

Unburned lodgepole pine forest returned a strong response in the L_{VH}-band and thus appear relatively bright in this image. Areas of increasing burn intensity have proportionately less above-ground forest biomass present; these areas produced less L_{VH} backscatter and appear darker. Yellowstone Lake, near the bottom of the image, appears black due to specular reflection and negligible L_{VH} backscatter.

Plate 39*b* shows a map of above-ground forest biomass, derived from the SIR-C data shown in (*a*) and from field measurements by the Yellowstone National Biological Survey. Colors in the map indicate the amount of biomass, ranging from brown (less than 4 tons per hectare) to dark green (nonburned forest with a biomass of greater than 35 tons per hectare). Rivers and lakes are shown in blue. The ability of long-wavelength and cross-polarized radar systems to estimate forest biomass may provide a valuable tool for natural resource managers and scientists, whether in the wake of natural disasters such as fires and windstorms, or in the course of routine forest inventory operations.

Due to the experimental nature of the SIR-C system, not all of the imagery from the two missions was processed. The raw data are archived at the USGS EROS Data Center and are currently being processed on demand. Unlike the subsequent Shuttle Radar Topography Mission (Section 8.17), which collected data over the majority of the earth's land surface, SIR-C data were only collected over isolated areas of research interest. Low resolution browse images for all SIR-C data acquisitions can be viewed on the EROS Data Center website. Precision processing of the full resolution data can be ordered at low cost.

8.13 ALMAZ-1

The Soviet Union (just prior to its dissolution) became the first country to operate an earth-orbiting radar system on a commercial basis with the launch of *Almaz-1* on March 31, 1991. Previously, the Soviet Union had operated *Cosmos-1870*, an experimental spaceborne radar system for a period of 2 years, and had collected a large volume of radar images over both land areas and the world's oceans. Although these images were not made generally available during the period of the system's operation, Cosmos-1870 served as a prototype to validate the design and operational capabilities of the Almaz-1 satellite.

Almaz-1 returned to earth on October 17, 1992, after operating for about 18 months. Other Almaz missions were planned prior to the dissolution of the Soviet Union.

Almaz-1 was launched with a nominal altitude of 300 km and an orbit that ranged from approximately 73° N latitude to 73° S latitude. About halfway through its lifetime, the orbital altitude of Almaz-1 was changed from 300 to 360 km in an attempt to prolong its lifetime in orbit. Depending

on the region of interest, Almaz-1 provided repeated image coverage at intervals of 1 to 3 days.

The primary sensor on board Almaz-1 was a SAR system operating in the S-band spectral region (10 cm wavelength) with HH polarization. The look angle for the system could be varied by rolling the satellite. The look angle range of 20° to 70° was divided into a standard range of 32° to 50° and two experimental ranges of 20° to 32° and 50° to 70°. The effective spatial resolution varied from 10 to 30 m, depending on the range and azimuth of the area imaged. The data swaths were approximately 350 km wide. Onboard tape recorders were used to record all data until they were transmitted in digital form to a ground receiving station.

8.14 ERS-1, ERS-2, AND ENVISAT

The European Space Agency (ESA) launched its first remote sensing satellite, *ERS-1*, on July 17, 1991, and its successor *ERS-2* on April 21, 1995. Both had a projected life span of at least 3 years; ERS-1 was retired from service on March 10, 2000, and ERS-2 is still in operation. The characteristics of both systems were essentially the same. They were positioned in sun-synchronous orbits at an inclination of 98.5° and a nominal altitude of 785 km. During the 1995 to 2000 period, a particular focus of the two satellites was tandem operation for repeat-pass radar interferometry.

On March 1, 2002, ESA launched *Envisat*. This large satellite platform carries a number of instruments, including the ocean monitoring system MERIS (Section 6.17), and an advanced imaging radar system. Following the launch, Envisat was maneuvered into an orbit matching that of ERS-2, just 30 min ahead of ERS-2 and covering the same ground track to within 1 km. North American data from ERS-1, ERS-2, and Envisat have been provided by receiving stations located in Prince Albert, Saskatchewan, Gatineau, Quebec, and Fairbanks, Alaska.

Sensors Onboard ERS-1 and ERS-2

ERS-1 and ERS-2 carry three principal sensors: (1) a C-band active microwave instrumentation (AMI) module, (2) a Ku-band radar altimeter (a nadir looking instrument for altitude, wind speed, and significant wave height measurements), and (3) an along-track scanning radiometer (a passive instrument consisting of an infrared radiometer and a microwave sounder). We limit this discussion to the AMI, which has a SAR system that operates in either an Image Mode or a Wave Mode and a microwave scatterometer that is used in a Wind Mode. In the Image Mode, the AMI produces SAR data over a 100-km, right-looking swath with a four-look resolution of approximately 30 m, VV po-

larization, and a 23° look angle (beam center). The high power and data rates for the system preclude onboard storage so the system is operated only while in line-of-sight communication with an ERS ground station.

The AMI Wave Mode is used to measure the radar reflectivity of the ocean surface as it is influenced by waves, yielding information on wavelength and direction of ocean wave systems. In the Wind Mode (a nonimaging mode) sea surface wind speeds and directions are measured.

Examples of ERS Images

The ERS radar systems operate in a shorter wavelength (C) band than many of the operational spaceborne radar systems and also employ a VV polarization, chosen to enhance the reflectivity of the oceanic returns. They also employ a relatively steep incident angle (23°). Thus, ERS images can be expected to look somewhat different than images of the same area obtained with most other operational spaceborne radar systems.

Figure 8.43 is an ERS-1 radar image of the Strait of Gibraltar showing internal waves (wavelength around 2 km) moving from the Atlantic Ocean to the Mediterranean Sea. Internal waves are usually created by the presence of two different layers of water combined with a current effect. In the case of the Strait of Gibraltar, the two layers are caused by different salinities, whereas the current is caused by the tide.

Figure 8.44 is an ERS-1 radar image showing an oil slick (lower right) in the Mediterranean Sea off the coast of France. Oil films have a dampening effect on waves, and the oil-coated smoother water has greater specular reflection than the surrounding water, thus appearing darker on this radar image. Figures 8.14, 8.28, and 8.29 (described previously) are also examples of ERS images.

Sensors Onboard Envisat

As mentioned previously, Envisat carries several sensors, including MERIS (Section 6.17) and the *Advanced Synthetic Aperture Radar (ASAR)* system. The ASAR system operates in the C band, with wavelengths similar to the SAR system onboard ERS-1 and ERS-2. ASAR can be programmed to function in a variety of modes, two of which (Image Mode and Wave Mode) were also implemented on ERS-1 and -2. In Image Mode, ASAR generates four-look high resolution (30-m) images and operates in one of seven predetermined swath configurations, with swath widths ranging from 58 to 109 km and look angles ranging from 14° to 45°. Either HH or VV polarization can be used in Image Mode. Wave Mode is designed to measure radar backscatter from ocean wave action intermittently over large areas. It uses the same swaths and polarizations as Image Mode but only collects data over small samples of the ocean at

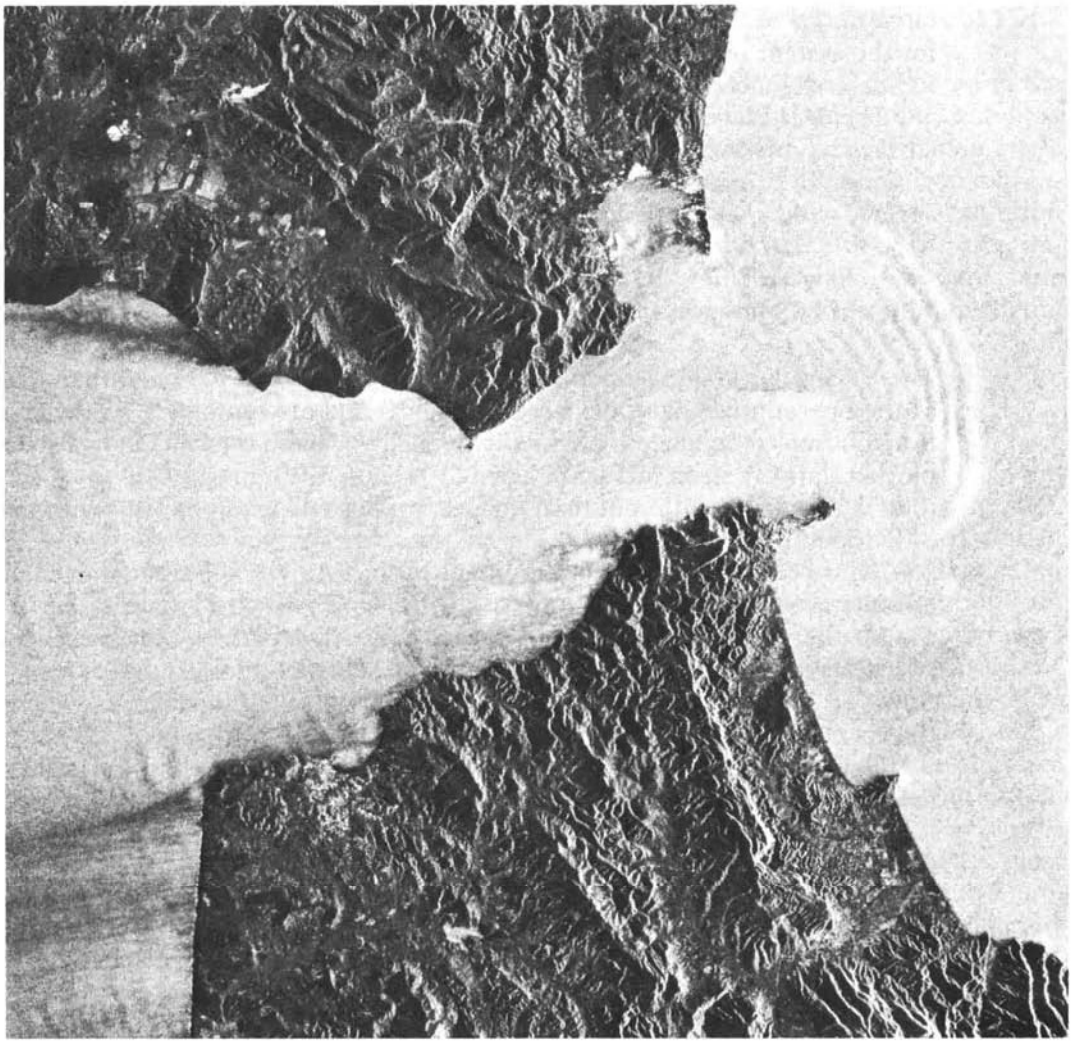

Figure 8.43 ERS-1 radar image of the Strait of Gibraltar showing internal waves moving from the Atlantic Ocean (at left) to the Mediterranean Sea (at right). Scale 1 : 650,000. (Courtesy ESA/ERS-1.)

regular intervals along the swath, rather than collecting a continuous strip of data. This intermittent operation provides a low data rate, such that the data can be stored on board the satellite, rather than being downlinked immediately to the ground station.

Other ASAR modes are based on the ScanSAR technique discussed in Section 8.10. Wide Swath Mode provides images at 150 m resolution, while Global Monitoring Mode uses a coarser resolution of 1 km. Both of these modes cover a 405-km swath with either HH or VV polarization. The final ASAR mode, Al-

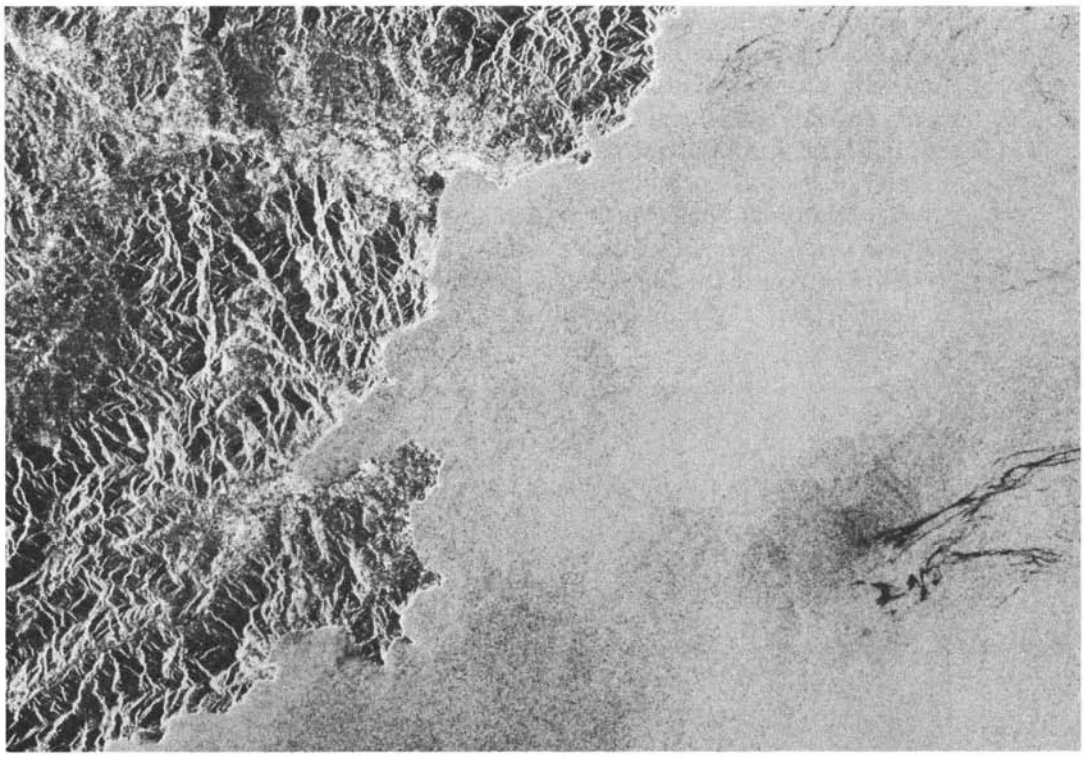

Figure 8.44 ERS-1 radar image showing an oil slick (darker area at lower right) in the Mediterranean Sea off the coast of France. Scale 1 : 475,000. (Courtesy ESA/ERS-1.)

ternating Polarization Mode, represents a modified ScanSAR technique that alternates between polarizations over a single swath, rather than alternating between near- and far-range swaths. This mode provides 30-m-resolution dual-polarization imagery, with one of three polarization combinations (HH and VV, VV and VH, or HH and HV).

8.15 JERS-1 AND ALOS

Developed by the National Space Development Agency of Japan, the *JERS-1* satellite was launched on February 11, 1992, and operated until October 12, 1998. It included both a four-band optical sensor (OPS; described earlier in Section 6.15) and an L-band (23-cm) SAR operating with HH polarization. The radar system had a three-look ground resolution of 18 m and covered a swath width of 75 km at a look angle of 35°. The JERS-1 was in a sun-synchronous orbit at an inclination of 98° and an altitude of 568 km. The repeat period for the orbit was 44 days.

Figure 8.45 is a JERS-1 radar image of Mt. Fuji, Japan. The snow-covered peak of Mt. Fuji is dark toned, as was the snow-covered peak of Michinmahuida Volcano that was shown in Figure 8.16, a SIR-B stereopair. Several lakes appear black, and recently clearcut areas appear dark toned, as contrasted with the lighter toned forested areas. Developed areas appear light toned.

The National Space Development Agency of Japan plans to launch an *Advanced Land Observing Satellite (ALOS)* in the summer of 2004. Among the systems onboard this satellite is a *Phased Array L-band Synthetic Aperture Radar (PALSAR)* system. Operating at the L-band, PALSAR will have a cross-

Figure 8.45 JERS-1 radar image showing Mt. Fuji and vicinity, Japan. Scale 1:450,000. (NASDA, 1992. Courtesy Remote Sensing Technology Center of Japan.)

track pointing capability over a range of look angles from 18° to 51°. In its fine resolution mode, PALSAR will use an HH or VV single polarization in its standard configuration, with a two-look spatial resolution of 10 m. However, a dual polarization mode will also be available (either HH and HV, or VV and VH) at a spatial resolution of 20 m. In its ScanSAR mode, PALSAR will have a swath width of up to 350 km, with a resolution of about 100 m in both azimuth and range directions, and a polarization of either HH or VV.

8.16 RADARSAT

Radarsat-1, launched on November 28, 1995, is the first Canadian remote sensing satellite. It was developed by the Canadian Space Agency in cooperation with the United States, provincial governments, and the private sector. Canada is responsible for the design, control, and operations of the overall system, while NASA provided the launch services. Radarsat-1 had an initial expected lifetime of 5 years, and as of the time of this writing (2002), it is still fully operational. It will be followed by *Radarsat-2*, scheduled for launch in 2004. Radarsat data for North America are received at the Prince Albert, Saskatchewan, Gatineau, Quebec, and Fairbanks, Alaska, ground stations. The data are distributed commercially worldwide by *Radarsat International* (*RSI*), an arrangement that will continue for Radarsat-2.

The orbit for Radarsat is sun synchronous and at an altitude of 798 km and inclination of 98.6°. The orbit period is 100.7 min and the repeat cycle is 24 days. Radarsat is a right-looking sensor, facing east during the ascending orbit and west during the descending orbit. Because the antenna can be operated at various look angles and swath widths, the system provides 1-day repeat coverage over the high Arctic and approximately 3-day repeat coverage at midlatitudes.

The Radarsat SAR is a C-band (5.6-cm) system with HH polarization. The system can be operated in a variety of beam selection modes providing various swath widths, resolutions, and look angles. In the ScanSAR mode, either two, three, or four single beams are used during data collection. Table 8.5 and Figure 8.46 summarize the modes in which the system operates.

The primary applications for which Radarsat has been designed include ice reconnaissance, coastal surveillance, land cover mapping, and agricultural and forestry monitoring. The near-real-time monitoring of sea ice is important for reducing the navigational risks of Arctic ships. Other uses include disaster monitoring (e.g., oil spill detection, landslide identification, flood monitoring), snow distribution mapping, wave forecasting, ship surveillance in offshore economic zones, and measurement of soil moisture. The different operating modes of the system allow both broad monitoring programs to be conducted as well as more detailed investigations using the fine resolution mode.

TABLE 8.5 Radarsat-1 Beam Selection Modes

Beam Mode	Number of Beam Positions	Swath Width (km)	Look Angle (deg)	Resolution[a] (m)	Number of Looks
Standard	7	100	20–49	25	4
Wide	3	150–165	20–39	30	4
Fine	5+	45	37–48	8	1
Extended high	6	75	50–60	25	4
Extended low	1	170	10–23	35	4
ScanSAR narrow	2	305	20–46	50	2–4
ScanSAR wide	1	510	20–49	100	4–8

[a]Resolution values are approximate. Azimuth and range resolution values differ, and range resolution varies with range (which in turn varies with look angle).

Figure 8.47 shows an area of forest clearcuts in Alberta, Canada, imaged by Radarsat-1 at two different incident angles. Clearcut areas in northern Canada generally have a rough surface (with varying topography, standing tree trunks, new trees, and slash piles), and it has been found that they are difficult to distinguish from forested areas when incident angles are low. The clearcut areas are clearly visible (as dark-toned patches) in (*b*), where the incident angle varies from 45° to 49°, and much less visible in (*a*), where the incident angle varies from 20° to 27°.

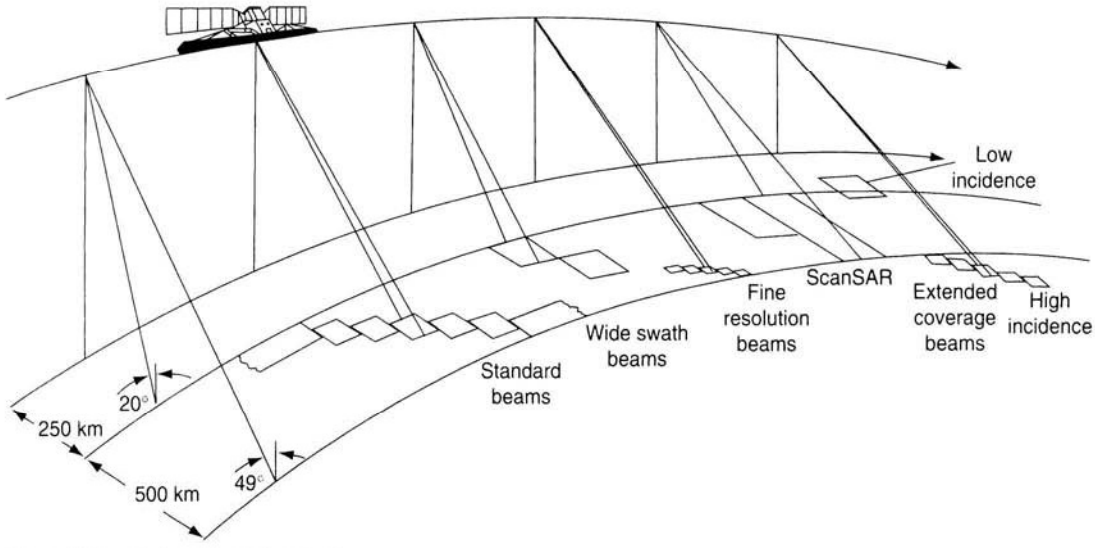

Figure 8.46 Radarsat imaging modes.

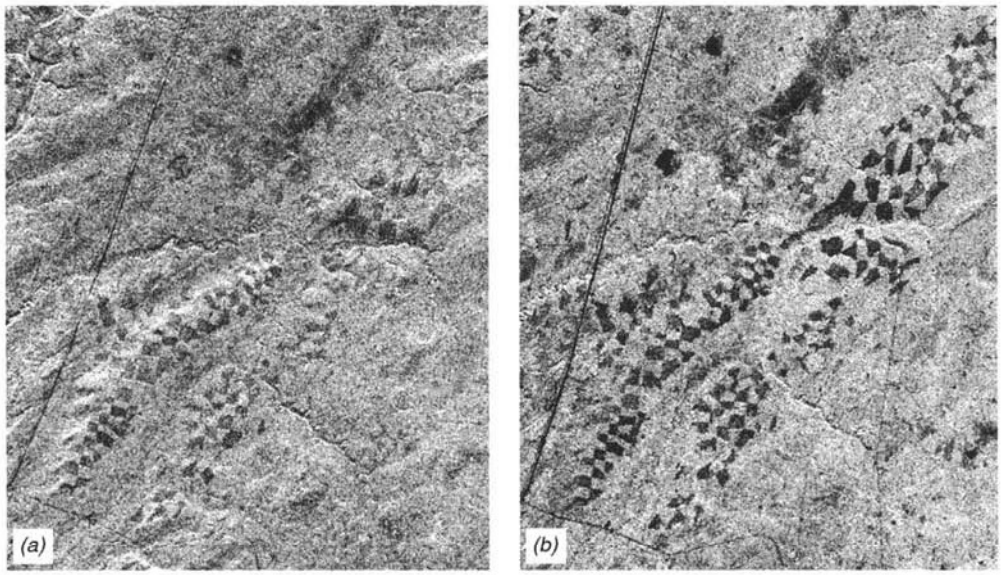

Figure 8.47 Radarsat-1 images illustrating the effect of incident angle on the appearance of clearcuts in a forested area near Whitecourt, Alberta, Canada: (*a*) Incident angle 20 to 27°; (*b*) Incident angle 45 to 49°. Winter image, cold, dry snow ground cover. (Radarsat data copyright © Canadian Space Agency 1996. Received by the Canada Centre for Remote Sensing. Processed and distributed by RADARSAT International. Courtesy Canada Centre for Remote Sensing.)

Figure 8.48 shows flooding of the Red River, Manitoba, Canada, in May 1996. The broad, dark area from lower right to the top of the image is smooth, standing water. The lighter toned areas to the left and upper right are higher, nonflooded, ground. Where standing water is present under trees or bushes, corner reflection takes place and the area appears very light toned. This is especially evident near the Red River. (See also Figure 8.32 for an example of this effect.) The town of Morris can be identified as a light toned rectangle in the flooded area. The town is protected by a levee and, as a result, has not flooded. Other, smaller areas that have not flooded (but are surrounded by water) can also be seen in this image.

Figure 8.49 illustrates the use of Radarsat data for ice type identification in the Gulf of St. Lawrence, Canada. Because radar returns vary with the salinity, surface roughness, and surface wetness of ice, image interpretations can be made to assess ice conditions. Also, images obtained over a period of days and weeks can be used to monitor ice movement. Thin first-year ice floes (A) are distinguishable by their shape and tone relative to the surrounding features. Lower ice salinity and a relatively smooth surface result in low to moderate radar returns (relatively dark-toned areas on the image). "Brash ice" (B) found between first-year ice floes consists of floating ice made up of ice fragments from other

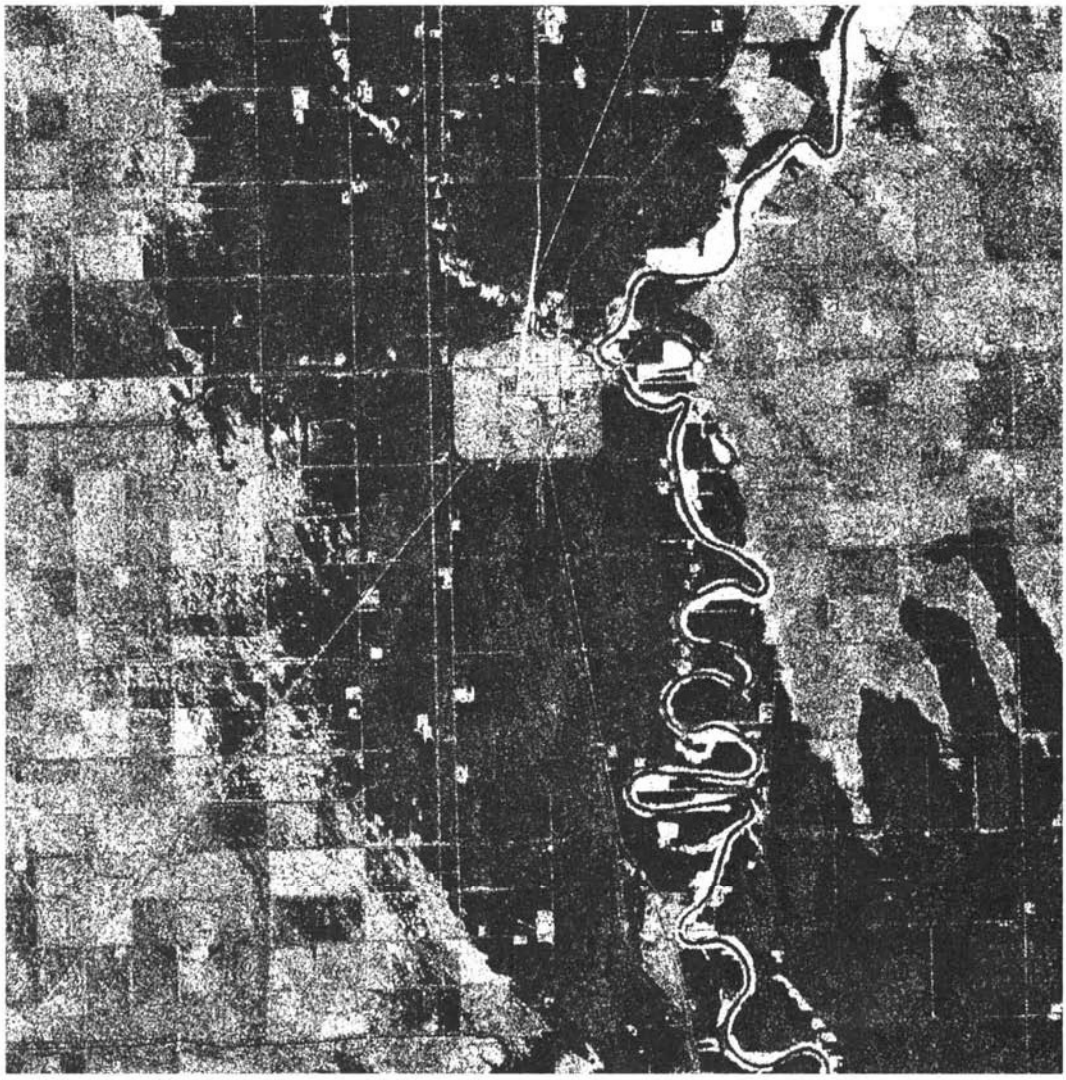

Figure 8.48 Radarsat-1 image showing flooding of the Red River, Manitoba, Canada, May 1996. Standard beam mode, incident angle 30 to 37°. Scale 1:135,000. (Radarsat data copyright © Canadian Space Agency 1996. Received by the Canada Centre for Remote Sensing. Processed and distributed by RADARSAT International. Enhanced and interpreted by the Canada Centre for Remote Sensing.)

forms. This ice type returns moderate to strong amounts of energy and appears light toned. Shown at (C) is a pressure ridge between thin first-year ice floes. These ridges act as corner reflectors and appear light toned, if large enough. A crack, or "lead," within a first-year ice floe is shown at (D). This feature exhibits strong radar returns because of the presence of brash ice within the crack.

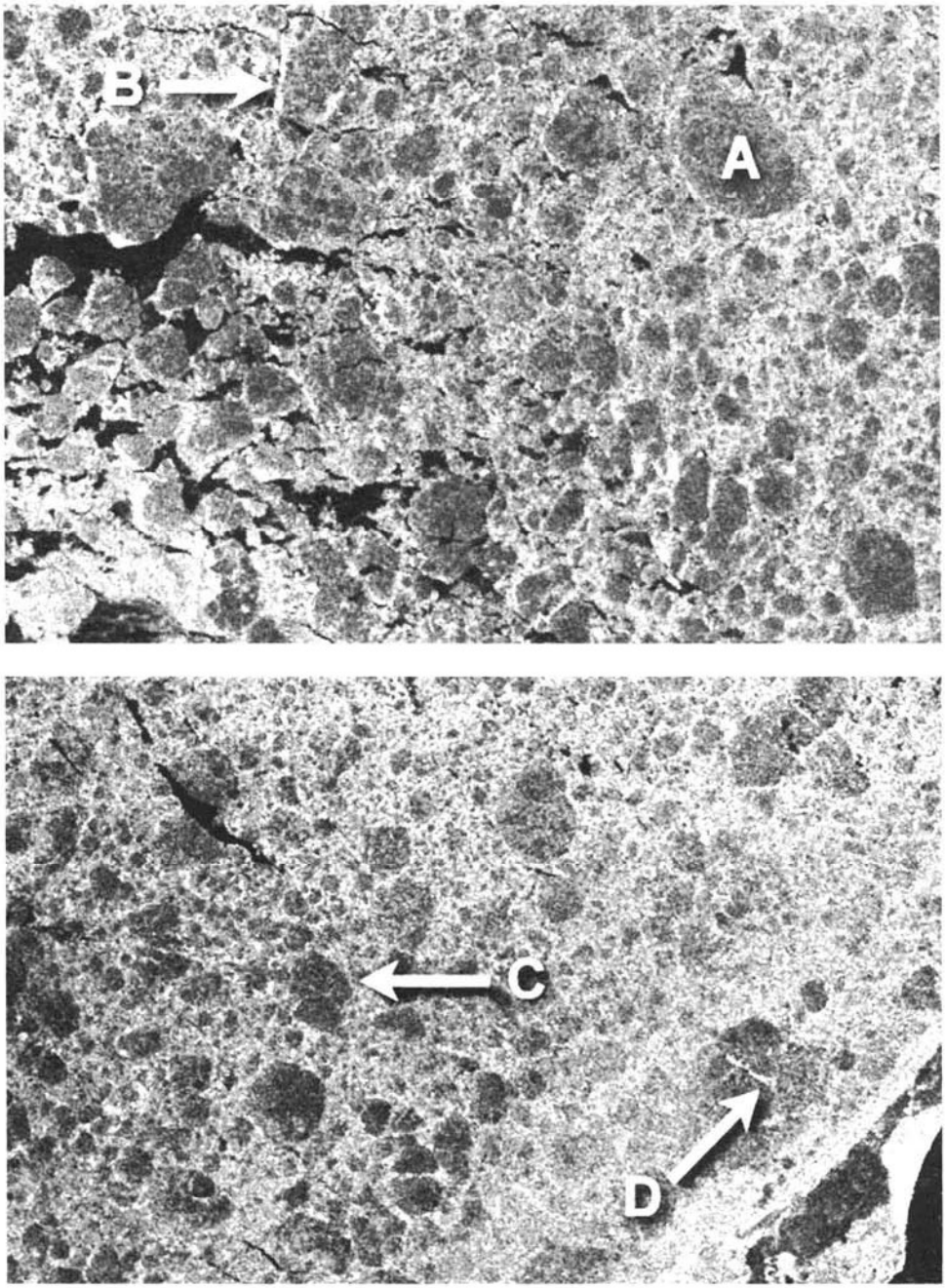

Figure 8.49 Radarsat-1 images of the Gulf of St. Lawrence, Canada. Shown at A is a first-year ice floe; at B is "brash ice"; at C is a pressure ridge; and at D is a crack or "lead" within first-year ice. (Radarsat data copyright © Canadian Space Agency 1996. Courtesy Canada Centre for Remote Sensing and Canadian Ice Service.)

As mentioned earlier, Radarsat-2 is scheduled for launch in 2004. This satellite will provide data continuity to Radarsat-1 users and data for new commercial applications tailored to market needs. Its SAR is a C-band system with HH, VV, HV, and VH polarization options. It has beam selection modes similar to Radarsat-1 but with an increased number of modes available. The various modes support swath widths from 10 to 500 km, look angles from 10° to 60°, resolutions varying from 3 to 100 m, and number of looks varying from 1 to 10.

8.17 SHUTTLE RADAR TOPOGRAPHY MISSION

The *Shuttle Radar Topography Mission (SRTM)* was a joint project of the National Imagery and Mapping Agency (NIMA) and NASA to map the world in three dimensions. During a single Space Shuttle mission on February 11 to 22, 2000, SRTM collected single-pass radar interferometry data covering 119.51 million km^2 of the earth's surface, including over 99.9 percent of the land area between 60° N and 56° S latitude. This represents approximately 80 percent of the total land surface worldwide and is home to nearly 95 percent of the world's population.

The C-band and X-band antennas from the 1994 SIR-C/X-SAR shuttle missions (Section 8.12) were used for data collection. To provide an interferometric baseline suitable for data acquisition from space, a 60-m-long rigid mast was extended when the shuttle was in orbit, with a second pair of C-band and X-band antennas located at the end of the mast. The primary antennas in the shuttle's payload bay were used to send and receive data, while the outboard antennas on the mast operated only in receiving mode. The extendible mast can be seen during testing prior to launch in Figure 8.50. In

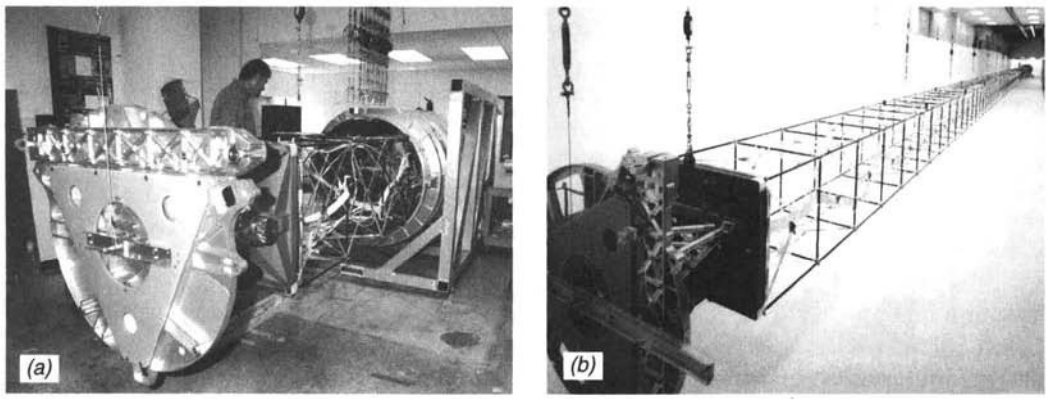

Figure 8.50 The SRTM extendable mast during prelaunch testing: (*a*) view of the mast emerging from the canister in which it is stowed during launch and landing; (*b*) the mast fully extended. (Courtesy NASA/JPL/NIMA.)

Figure 8.50*a* most of the mast is stowed within the canister visible in the background. In Figure 8.50*b* the mast is extended to its full length. The two outboard antennas were not installed on the mast at the time of these tests; during the mission they were mounted on the triangular plate visible at the end of the mast in Figure 8.50. An artist's rendition of the shuttle in orbit during SRTM is provided in Figure 8.51. This illustration shows the position and orientation of the various SRTM components, including the main antenna inside the shuttle's payload bay; the canister for storage of the mast, the mast itself, and the outboard antennas at the end of the mast.

The system collected 12 terabytes of raw data during the 11-day mission, a volume of data that would fill over 15,000 CD-ROMs. Processing this volume of data has taken several years and is not yet complete as of this writing (2002). Plans call for the elevation data to be released as each continent is completed; data for the continental United States were released in 2002 and are being distributed by the U.S. Geological Survey. The SRTM processor produces digital elevation models with a pixel spacing of 1 arcsecond of latitude and longitude (about 30 m). The data for areas outside the United States will be aggregated prior to public distribution and will have a pixel spacing of 3 arcseconds (about 90 m). The absolute horizontal and vertical accuracy of the data are better than 20 and 16 m, respectively. In addition to the elevation data, the SRTM processor produces orthorectified radar image products and maps showing the expected level of error in the elevation model.

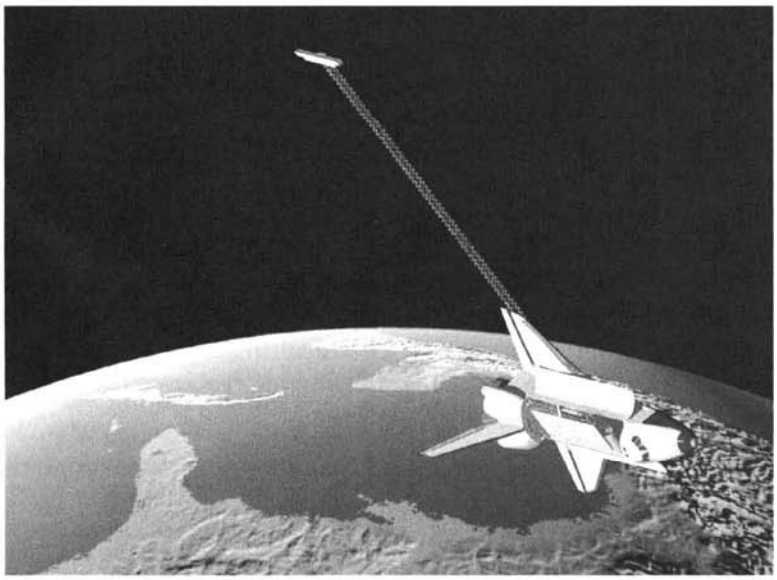

Figure 8.51 Artist's rendition of the shuttle in orbit during SRTM, showing the positions of the main antenna inside the payload bay, the canister, the mast, and the outboard antennas. (Courtesy NASA/JPL/NIMA.)

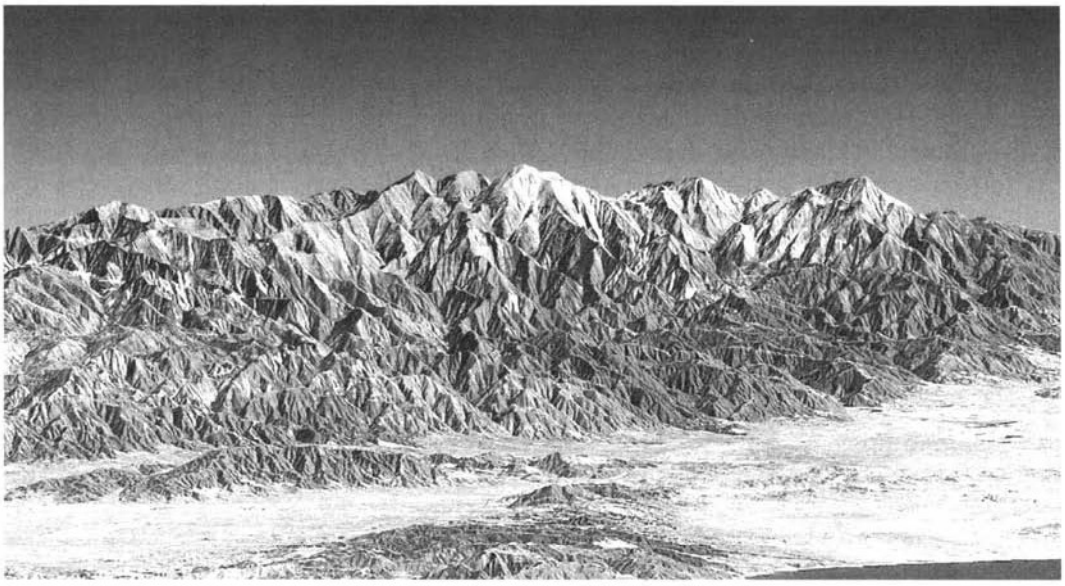

Figure 8.52 Perspective view of a DEM of the Los Angeles area, derived from SRTM interferometric radar data. A Landsat-7 ETM+ image has been draped over the DEM to show land cover patterns. (Courtesy NASA.)

Figure 8.52 shows a perspective view of a DEM for the Los Angeles metropolitan area. The DEM was derived from interferometric analysis of SRTM imagery, and a Landsat-7 ETM+ image was draped over the DEM. This view is dominated by the San Gabriel Mountains, with Santa Monica and the Pacific Ocean in the lower right and the San Fernando Valley to the left.

Technical problems during the shuttle mission caused 50,000 km^2 of the targeted land area to be omitted by SRTM. These omitted areas represent less than 0.01 percent of the land area intended for coverage. All the omitted areas were located within the United States, where topographic data are already available from other sources. As the first large-scale effort to utilize single-pass radar interferometry for topographic mapping from space, the project has proved to be highly successful. The resulting topographic data and radar imagery represent a unique and highly valuable resource for future geospatial applications.

8.18 SPACEBORNE RADAR SYSTEM SUMMARY

Given the number and diversity of recent past, currently operational, and planned future radar satellites, it is difficult to readily compare the operating

TABLE 8.6 Characteristics of Major Past Operational Spaceborne Synthetic Aperture Radar Systems

Characteristic	Almaz-1 (Soviet Union)	ERS-1 (ESA)	JERS-1 (Japan)
Launch date	March 31, 1991	July 17, 1991	February 11, 1992
End of operations	October 17, 1992	March 10, 2000	October 12, 1998
Altitude, km	300 or 360	785	568
Wavelength band	S band	C band	L band
Polarization modes	Single	Single	Single
Polarization	HH	VV	HH
Look angle	20–70°	23°	35°
Swath width, km	350	100	75
Resolution, m	10–30	30	18

characteristics of the various systems. Tables 8.6, 8.7, and 8.8 are presented to assist in this process. Note that there has been a general trend toward increasing design sophistication, including multiple polarizations, multiple look angles, and multiple combinations of resolution and swath width. However, none of these systems operates at more than one wavelength band—a fact that testifies to the technical challenges involved in designing spaceborne multiwavelength radar systems. In fact, all currently available spaceborne radar systems only operate at the C band. This places significant limits on the range of potential applications of spaceborne radar systems, a circumstance that will not be changed until the scheduled launch of the L-band ALOS PALSAR system in 2004.

TABLE 8.7 Characteristics of Major Current Operational Spaceborne Synthetic Aperture Radar Systems

Characteristic	ERS-2 (ESA)	Radarsat-1 (Canada)	Envisat (ESA)
Launch date	April 21, 1995	November 28, 1995	March 1, 2002
Altitude, km	785	798	785
Wavelength band	C band	C band	C band
Polarization modes	Single	Single	Single, dual
Polarization(s)	VV	HH	HH, VV, HV, VH
Look angle	23°	10–60°	14–45°
Swath width, km	100	45–500	58–405
Resolution, m	30	8–100	30–1000

TABLE 8.8 Characteristics of Planned Future Spaceborne Synthetic Aperture Radar Systems

Characteristic	Radarsat-2 (Canada)	ALOS PALSAR (Japan)
Scheduled launch	2004	2004
Altitude, km	798	692
Wavelength band	C band	L band
Polarization modes	Single, dual, quad	Single, dual
Polarization(s)	HH, VV, HV, VH	HH, VV, HV, VH
Look angle	10–60°	10–51°
Swath width, km	10–500	Up to 350
Resolution, m	3–100	10–100

8.19 PLANETARY EXPLORATION

Synthetic aperture radar is especially well suited for obtaining images of planetary bodies that may be too cloud covered for sensing by optical means. Below we describe missions to Venus and to Saturn's moon Titan.

Radar Remote Sensing of Venus

Launched from the space shuttle *Atlantis* on May 4, 1989, the *Magellan* spacecraft has provided remarkable radar images of the planet Venus. A typical elliptical polar orbit of Magellan around the planet took approximately 3 hr and 15 min and dipped from an altitude of 2100 km above the poles to an altitude of 175 km above the equator. From this orbit, the S-band SAR aboard the spacecraft collected successive image swaths 16,000 km long and 25 km wide, with a multilook spatial resolution of 75 m. The radar was able to penetrate Venus' inhospitable atmosphere, which includes thick clouds of sulfuric acid. The data from the mission are not only advancing the scientific understanding of Venus but are also helping scientists understand more clearly the geologic forces that shaped Earth. Often referred to as Earth's sister planet, Venus is nearly identical to Earth in size and density. Magellan unveiled a new view of Venus' striking volcanism, tectonics, and meteoroid impact processes.

Figure 8.53 is a Magellan image mosaic showing the largest (280-km-diameter) impact crater known to exist on Venus. Named Mead, after American anthropologist Margaret Mead, this multiring crater has a light-toned inner floor that is interpreted as resulting from considerable infilling of the original crater cavity by impact melt and/or by volcanic lavas.

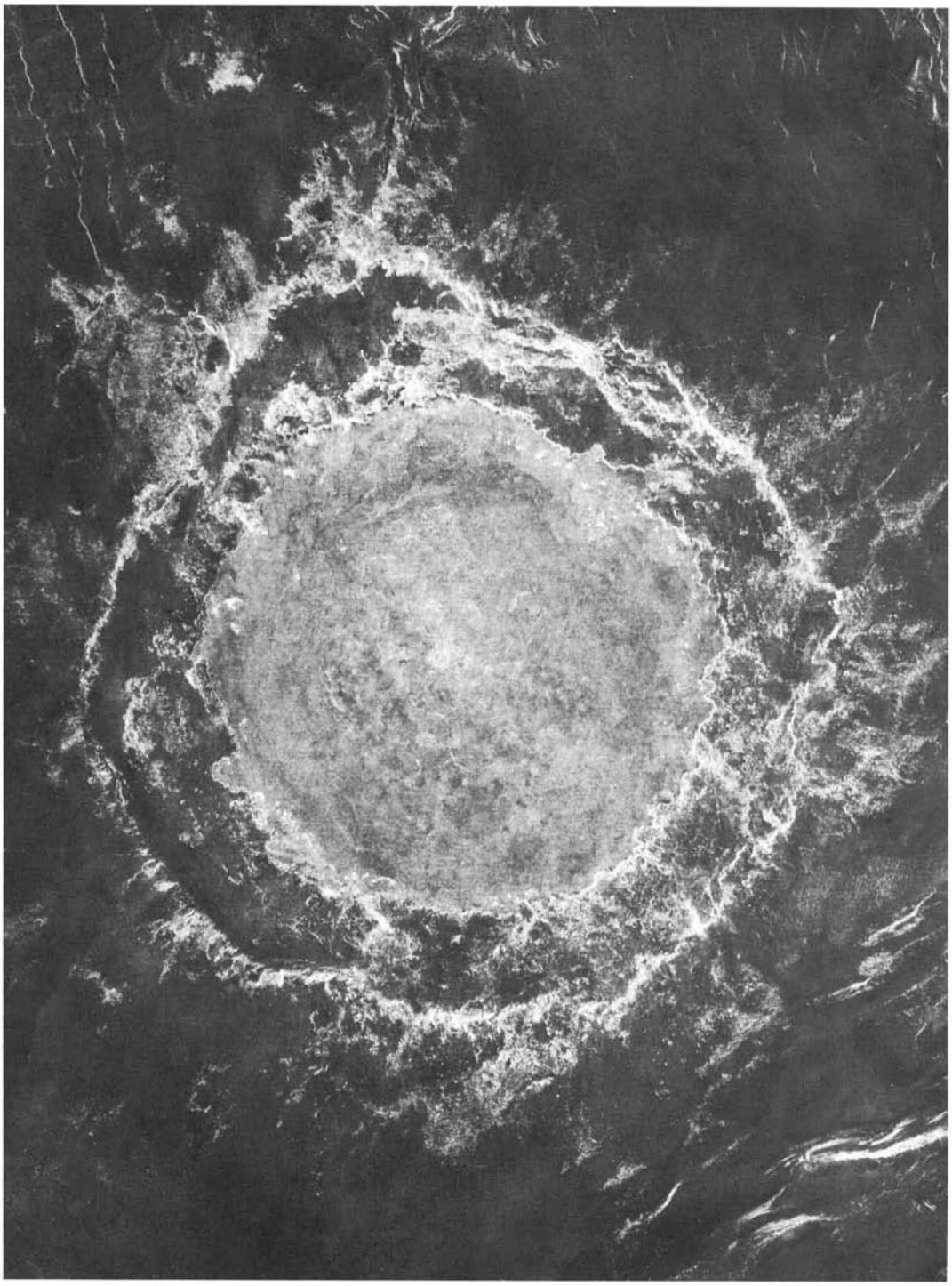

Figure 8.53 Magellan radar image mosaic showing Mead impact crater, Venus. (Courtesy NASA/JPL/Caltech.)

Figure 8.54 is a stereopair of radar images of the Geopert-Meyer crater on Venus, named for the twentieth-century Polish physicist and Nobel laureate. This crater was imaged from the same side at look angles of 28° and 15°. This crater is 35 km in diameter and can be seen near the center of the stereopair. The crater lies above an escarpment at the edge of a ridge belt. Analysis of stereopairs allows planetary scientists to resolve details of topographic relationships on Venusian craters, volcanoes, mountain belts, and fault zones.

Figure 8.55 is a perspective view image of Venus' surface created by merging Magellan radar data with radar altimetry data collected during the mission. Shown is Sapas Mons, from a viewpoint located 243 km to the south. Sapas Mons appears at the center of the image, with two peaks that ascend to

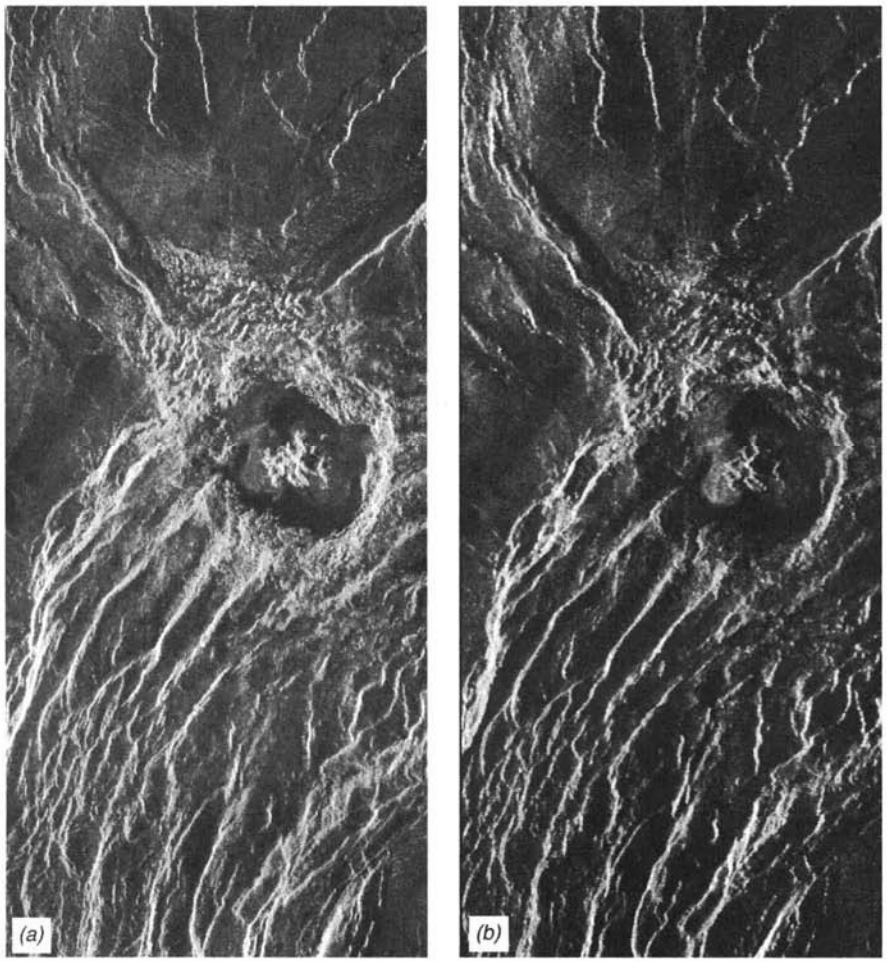

Figure 8.54 Magellan same-side radar stereopair of the crater Geopert-Meyer, Venus: (*a*) 28° incident angle; (*b*) 15° incident angle. (Courtesy NASA/JPL/Caltech.)

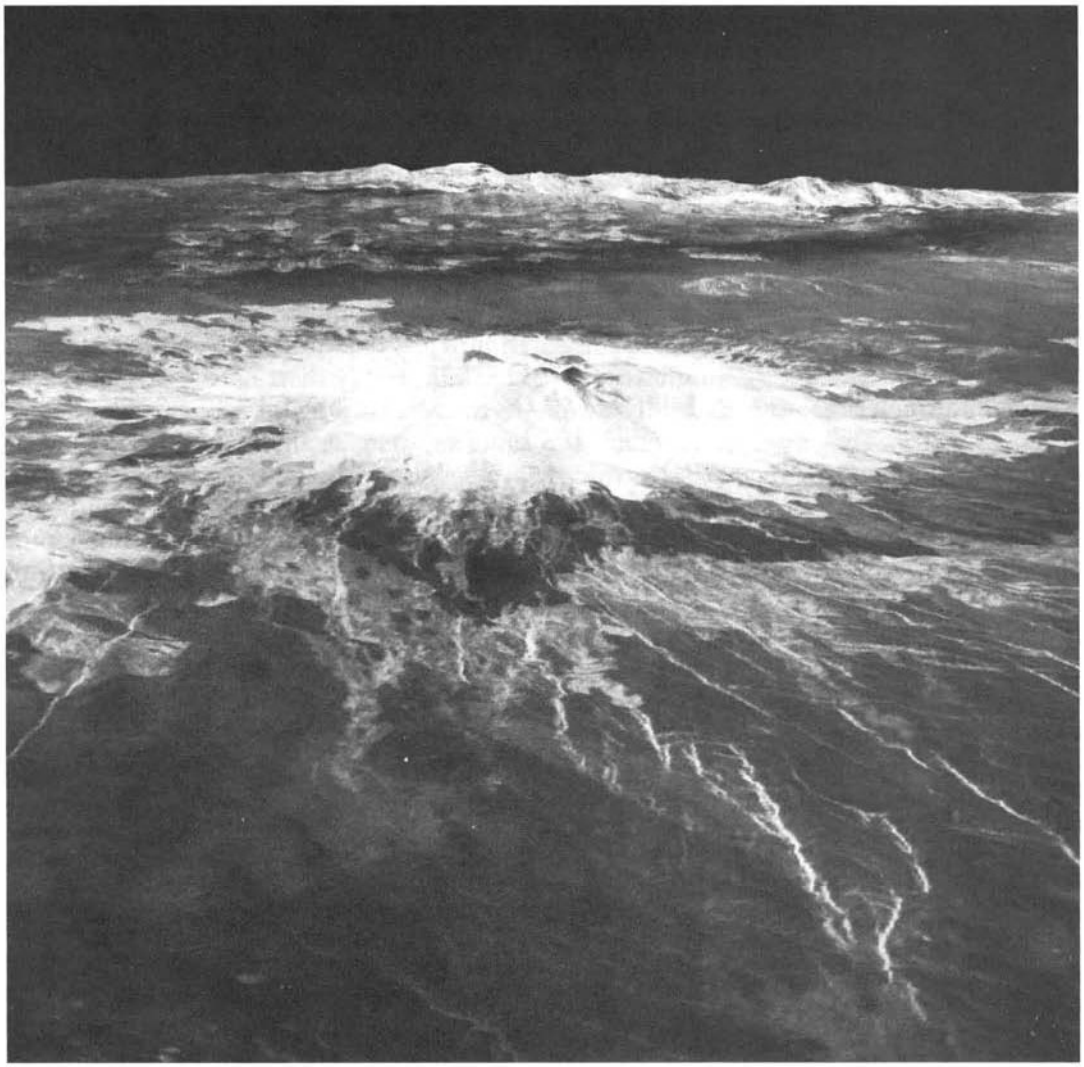

Figure 8.55 Magellan perspective view radar image of Sapas Mons, Venus. The vertical scale in this perspective has been exaggerated 10 times. (Courtesy NASA/JPL/Caltech.)

a height of 3 km above the mean surface. Lava flows extend for hundreds of kilometers from the large volcano onto the smooth plains.

Radar Remote Sensing of Saturn's Moon Titan

Launched from Kennedy Space Center on October 15, 1997, NASA's *Cassini* spacecraft is expected to reach Saturn in June 2004. One of several remote

sensing systems that will be used to explore Saturn's moon, Titan, is a synthetic aperture radar system that operates in the Ku band (2.2 cm) and has a resolution of 0.35 to 1.7 km. This system has the scientific objectives of studying the geologic features and topography of the solid surface of Titan and to acquire data on non-Titan objects (e.g., Saturn's rings) as conditions permit.

8.20 PASSIVE MICROWAVE SENSING

Operating in the same spectral domain as radar, passive microwave systems yield yet another "look" at the environment—one quite different from that of radar. Being passive, these systems do not supply their own illumination but rather sense the naturally available microwave energy within their field of view. They operate in much the same manner as thermal radiometers and scanners. In fact, passive microwave sensing principles and sensing instrumentation parallel those of thermal sensing in many respects. As with thermal sensing, blackbody radiation theory is central to the conceptual understanding of passive microwave sensing. Again as in thermal sensing, passive microwave sensors exist in the form of both radiometers and scanners. However, passive microwave sensors incorporate antennas rather than photon detection elements.

Most passive microwave systems operate in the same spectral region as the shorter wavelength radar (out to 30 cm). As shown in Figure 8.56, passive microwave sensors operate in the low energy tail of the 300 K blackbody radiation curve typifying terrestrial features. In this spectral region, all objects in

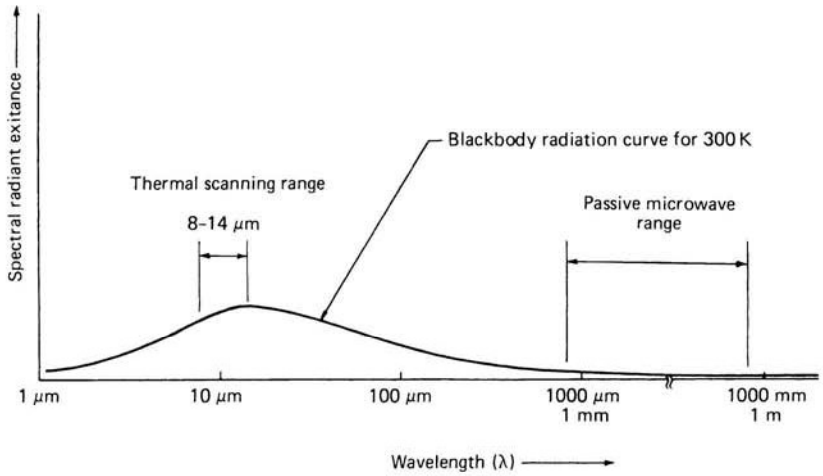

Figure 8.56 Comparison of spectral regions used for thermal versus passive microwave sensing.